CHARACTERIZING MECHANISMS OF POTENTIAL INHIBITORS OF THE HSP90 CHAPERONE COMPLEX

By

SEAN ALAN GILE

Bachelor of Science in Biochemistry and Molecular Biology
Oklahoma State University
Stillwater, Oklahoma
2015

Master of Science in Biochemistry and Molecular Biology
Oklahoma State University
Stillwater, Oklahoma
2022

Submitted to the Faculty of the
Graduate College of the
Oklahoma State University
in partial fulfillment of
the requirements for
the Degree of
DOCTOR OF PHILOSOPHY
May, 2023

CHARACTERIZING MECHANISMS OF POTENTIAL INHIBITORS OF THE HSP90 CHAPERONE COMPLEX

Dissertation Approved:

Dr. Robert Matts

Dissertation Adviser

Dr. Steven Hartson

Dr. Ramanjulu Sunkar

Dr. Stephen Clarke

ACKNOWLEDGEMENTS

First, I would like to dedicate this work to my late mother, Annette Gile, who was my greatest supporter in all things, and motivator for when times were tough. I will always regret that you did not get to see me complete graduate school. Second, I must thank all of my family for their love, and support: Dad, Ben, Brittany, Tim, Danielle, and Lauren. Without you all I would not have been able to finish this dissertation. Next, I would like to thank my mentors, and fellow graduate students that have helped over the many years: Dr. Hartson, Dr. Matts, Matt Greenlee, Maurie Balch, and Lawrie Veale. Lastly, I need to thank my closest friends for their constant support, and words of encouragement: Tyler Sampsel, and Ryan Latham.

Name: SEAN ALAN GILE

Date of Degree: MAY, 2023

Title of Study: CHARACTERIZING MECHANISMS OF POTENTIAL INHIBITORS OF THE HSP90 CHAPERONE COMPLEX

Major Field: BIOCHEMISTRY AND MOLECULAR BIOLOGY

Abstract: In this work, we characterized the effects of ten compounds reported to be inhibitors of the Hsp90 chaperone complex in Jurkat leukemia cells, and compared them to the N-terminal Hsp90 inhibitor AUY922. Our primary focus was to elucidate the proteomic profile of C-terminal Hsp90 inhibition. Changes in protein expression of treated cells were quantified by labeling peptides with Tandem Mass Tags (TMT) isobaric labels, and SPS-MS3 methodologies leading to approximately 6000 proteins identified in all biological replicates (n=6). We characterized the compounds for hallmark Hsp90 inhibition motifs including the induction of the heat shock response, and depletion of Hsp90-dependent protein kinases. In both our Western blotting and proteomic data: ailanthone, celastrol, clorobiocin, gambogic acid, coumermycin A1, derrubone, garcinol, daurisoline, β-lapachone, and α-mangostin failed to depleted Hsp90-dependent clients. Pairwise comparisons of proteomic perturbations in response to drug treatment showed negligible Pearson correlation between AUY922 and all the compounds in our panel, except celastrol. Bootstrapped hierarchical clustering was completed on our compound panel alone, and along with previously generated data by our lab group, and from the literature. The compounds from our panel generated a distinct cluster away from the branch containing N-terminal Hsp90 inhibitors and proteostasis perturbing compounds. From this we concluded that none of the compounds characterized are inhibitors of the Hsp90 chaperone complex. Additionally, we suggest scrapping the C-terminal Hsp90 inhibition model. Bioinformatics analysis consisting of GO, and protein-protein interaction networks enriched terms indicting that the majority of the compounds induce apoptosis through disruption of the endoplasmic reticulum and/or the mitochondria. After completing an additional literature review guided by our bioinformatics enrichments we found studies supporting our findings. As such, we suggest that future studies on the compounds not be focused on Hsp90 inhibition.

TABLE OF CONTENTS

Chapter Page

LIST OF TABLES

Table Page

LIST OF FIGURES

Figure Page

Figure Page

Figure Page

CHAPTER I

REVIEW OF LITERATURE

Heat Shock Protein 90 kDa

Heat shock protein 90 kDa (Hsp90) is a chaperone protein which, along with a cohort of co-chaperones, ensures the proper folding of client proteins. Hsp90 is a highly conserved protein found across all kingdoms [1]. Hsp90 is the most abundant heat shock protein accounting for 1-2 % of the proteome of normal cells, and up to 3-5 % in cells under stress [2, 3]. Hsp90 has a plethora of client proteins involved in cell signaling which attribute to all six hallmarks of cancer [4, 5]. Additionally, cancer cells become addicted to Hsp90 for the role it plays in the mitigation of acidosis, hypoxia, and mutation accumulation of the tumor environment [5]. In humans there are four isoforms of Hsp90: GRP94 (glucose-related protein 94 kDa) in the endoplasmic reticulum, TRAP1 (tumor necrosis factor-associated protein 1) in the mitochondria, Hsp90α (stress inducible) and Hsp90β (constitutively expressed) in the cytoplasm.

Hsp90 Structure

Hsp90 functions as a homodimer. Each monomer consists of three domains: C-terminal domain, and a middle (Mid), and N-terminal domain which are connect by a small

flexible linker region. The C-terminal domain is the site of dimerization, and contains a MEEVD sequence critical for the interaction with co-chaperones containing tetratricopeptide repeat (TPR) domains [6-8]. The Mid domain is required for the interaction of client proteins and co-chaperones. The N-terminal domain of Hsp90 contains a unique ATP hydrolysis site (GHKL super family) that is structurally similar to gyrases, histidine kinases, and topoisomerases [9]. The ATPase activity of the N-terminal domain allows for the cycling between open and closed conformations to ensure the proper folding of clients. Hsp90 structure has been elucidated through multiple X-ray crystallography studies bound to ADP [9], inhibitors [10], and clients [11].

Hsp90 Function

Hsp90 chaperone function is a multiple step process controlled through conformational changes induced by substrate and co-chaperone interactions [12]. The chaperone cycle begins with a homodimer of Hsp90 in the open conformation without ATP bound. Next, ATP binds in the N-terminal domain causing the ATP lid to close, while leaving Hsp90 in the open conformation. Then, conformational changes bring the two N-terminal domains together allowing for their dimerization. Subsequently, the Mid domains are also brought closer together, clamping the client between the monomers. The closed conformation is when the misfolded clients or nascent polypeptides are refolded to their native state. Following the hydrolysis of ATP to ADP the chaperone complex returns to the open state allowing for the release of now properly folded client.

As alluded to previously, chaperone function is not completed by Hsp90 alone. To date there are more than 20 known Hsp90 co-chaperones which function in recruitment of

clients to the chaperone complex and alter ATPase activity. A subset of co-chaperones and their function are listed in Table 1.1 below.

Co-chaperone	Function
Aha1 (Activator of Hsp90 ATPase activity)	Stimulates the conformational changes of Hsp90 chaperone cycle. Associates with non-native proteins preventing aggregation and promoting ubiquitination to maintain cellular proteostasis [13].
Cdc37 (Cell division cycle 37 protein)	Kinase-specific co-chaperone responsible for stabilizing and activating over half of the human kinome; inhibits Hsp90 ATPase activity [11].
CHIP (C-terminus of Hsc70-interacting protein)	E3 ubiquitin-ligase which is selective for non-native client protein [14].
Cyp40 (Cyclophilin 40)	An immunophilin, a peptidyl-propyl isomerase that catalyzes conversion between cis and trans isomers of peptide bonds containing proline. Associates with Hsp90 to ensure the proper folding of steroid hormone receptors [15].
Fkbp51 (FK506-binding protein 51)	Immunophilin, associates with Hsp90 and to ensure the proper folding of steroid hormone receptors [15].
Fkbp52 (FK506-binding protein 52)	Immunophilin, associates with Hsp90 and to ensure the proper folding of steroid hormone receptors [15].
Hsp40 (Heat shock protein 40 kDa)	Associates with co-chaperone Hsp70 to stabilize and deliver non-native client proteins to Hsp90 chaperone complex [16].
Hsp70 (Heat shock protein 70 kDa)	Associates with co-chaperone Hsp40 to stabilize and deliver non-native client proteins to Hsp90 chaperone complex [17].
Hip (Hsp70-interacting protein)	Inhibits ATPase activity of Hsp70, delaying release of non-native client from the Hsp40/Hsp70/non-native client complex [18].
Hop (Hsp70-Hsp90 organizing protein)	Inhibits ATPase activity of Hsp90, coordinates non-native client handover from Hsp40/Hsp70/non-native client complex to Hsp90 [19].
p23	Stabilizes the closed conformation of Hsp90 chaperone cycle, inhibits ATPase activity of Hsp90, and interacts with steroid hormone receptors (both free and Hsp90 bound) [20-23].
Tom70 (translocase of the mitochondria outer membrane protein 70 kDa)	Interacts with Hsp90 and co-chaperones promoting transport of Hsp90-clients to the mitochondria. Promotes endoplasmic reticulum to mitochondria Ca^{2+} transfer [24].

Table 1.1 Co-chaperones of Hsp90

Additionally, Hsp90α is secreted into the extracellular space following environmental stressors including: cytokine signaling, heat shock, hypoxia, irradiation, and reactive oxygen species [5]. Extracellular Hsp90α has been shown to enhance cell motility. In studies of wound healing, out-performing many growth factors [25]. In cancer, extracellular Hsp90 has been shown to promote metastasis [26].

Hsp90 Clients

To date, there are more than 200 Hsp90 clients. The Picard laboratory maintains a up-to-date list of Hsp90 interactors, including co-chaperones and clients (https://www.picard.ch). A Hsp90 client protein can be defined as a protein that requires Hsp90 chaperoning for one or more of the following: activity, conformation, and/or stability. The client proteins can be grouped into three categories: kinases (cyclin dependent, serine/threonine, and tyrosine), transcription factors (includes steroid hormone receptors), and others. Many of these clients are involved in signal transduction pathways controlling cell cycle and are often over expressed or mutated in cancer cells.

Proteostasis

Protein homeostasis (proteostasis) is a set of highly complex interconnected pathways that regulate the cellular proteome (Reviewed in G.G Jayaraj, *et al*., 2019) [27]. These pathways encapsulate the entire life span of a protein beginning at synthesis, to nascent folding, subsequent maintenance folding, and ending with degradation. The ability to for these pathways to manage the composition, state, and turnover of proteins is critical avoid toxic aggregates. The coordination of these pathways are completed by a large number of chaperones and co-chaperones, with more than 300 being encoded in the human genome

[28]. There are eight classifications of chaperones, primarily grouped by molecular weight: Hsp40s, Hsp60s, Hsp70s, Hsp90s, Hsp100s, small Hsps, TPRs, and others [28].

Heat shock response

The heat shock response is a proteostasis pathway activated by cellular stress to alleviate misfolded, unfolded, and aggregated proteins [29, 30]. The heat shock response is induced by the transcription factor, Heat shock factor 1 (Hsf1). Hsf1, in its inactive state, is sequestered as a monomer in the cytoplasm during cellular homeostasis. There are conflicting models on what binding partner is sequestering Hsf1 under normal conditions [31, 32]. What both models agree on is cellular stress leads to release of Hsf1 from its sequestering partner, allowing for trimerization (activation), and subsequent translocation to the nucleus [33, 34]. In the nucleus, the now activated Hsf1 is capable of binding to heat shock reporter elements and inducing the transcription of heat shock proteins [34]. The induction of the heat shock proteins allows for the return to proteomic steady-state by folding proteins to their native conformation or directing the unfolded proteins to the proteasome for degradation.

Unfolded protein response

The unfolded protein response is a proteostasis pathway specific to the endoplasmic reticulum (ER) (Reviewed in Andrew P.K. Wodrich, *et al*., 2022) [35]. The ER is the organelle where membrane, and secreted proteins are synthesized and folded. The unfolded protein response is regulated by three transmembrane proteins: activating transcription factor (ATF6), PKR-like endoplasmic reticulum kinase (PERK/EIF2AK3), and inositol-requiring protein 1 (IRE1/ERN1). These three proteins work in concert to alleviate stress in the ER.

They are all also sequestered by chaperone protein BiP/Grp78 (Hsp70 class chaperone) [36, 37]. BiP disassociates from all three in response to increasing levels of stress-induced unfolded proteins. IRE1 is activated by dimerization and autophosphorylation in response to ER stress [38]. The IRE1 pathway induces genes involved in protein folding, trafficking, and degradation [39]. Degradation of proteins is completed through the endoplasmic reticulum associated degradation (ERAD) pathway, in which proteins are trafficked from the endoplasmic reticulum to the cytosol to be processed by the proteasome [40]. Additionally, IRE1 cleaves mRNAs and miRNAs targeted for the endoplasmic reticulum, eliminating new translation and protein-folding stress [41]. PERK is also activated through dimerization and autophosphorylation [42]. The PERK pathway inhibits global translation of new proteins through the phosphorylation of eIF2α, while allowing the select induction of genes involved in amino acid metabolism, apoptosis, autophagy, and oxidative stress [42]. ATF6 pathway has a significant amount of overlap with the IRE1 pathway [43]. ATF6 induces genes involved in protein quality control, and biogenesis of endoplasmic reticulum in an attempt to improve secretory capacity of the cell [44].

Ubiquitin proteasome system

The ubiquitin proteasome system maintains proteostasis through the degradation of unfolded proteins by the 26S proteasome [45, 46]. This pathway is responsible for approximately 80 % of protein turnover. Proteins set to be degraded are first marked with the ubiquitin modification. Ubiquitin is added to a lysine of the target protein in a highly regulated process by ubiquitin-activating enzymes (E1), ubiquitin-conjugating enzymes (E2), and ubiquitin ligases (E3). E1 enzymes are responsible for activating ubiquitin, and then handing it off to E2 enzymes. An E2 enzyme with activated ubiquitin is then coordinated to

the protein set to degraded by an E3 enzyme. Ubiquitination can be added as a single moiety (mono-ubiquitination) or as a set of multiple moieties in a string (poly-ubiquitination). Additionally, target proteins can have a single or multiple lysines ubiquitinated. Different ubiquitination patterns lead to different protein fates [47]. A protein must be poly-ubiquitinated in order to be coordinated to the 26S proteasome.

Inhibition of the Hsp90 chaperone complex

N-terminal inhibitors of Hsp90

The ansamycin antibiotic geldanamycin was the first natural product inhibitor of Hsp90 discovered [48]. Geldanamycin was shown to preferentially prevent the proliferation of cancer cell lines compared to normal cell lines [49]. Soon after, the macrolactone antibiotic radicicol was also shown to inhibit Hsp90, but with greater potency than Geldanamycin [50, 51]. Despite the different structures of these two compounds, both inhibit Hsp90 function by binding to the ATP-binding site located in the N-terminal domain [51]. Co-crystal structures of Hsp90 and both compounds were solved [10, 52]. These first generation inhibitors had problems with drug stability, and hepatotoxicity [53].

Second generation N-terminal Hsp90 inhibitors were developed using structure-based drug design leading to a handful of derivative compounds based on geldanamycin and radicicol. These compounds had increased potency and decreased negative side effects compared to the natural compounds. Geldanamycin derivatives primarily focused with altering the methoxy group located at position 17 (e.g. 17-AG, 17-AAG, and 17-DMAG) [54, 55]. The second generation radicicol derivatives are much more structurally diverse compared to their natural product (e.g. AUY922 and STA-9090) [56, 57].

Additionally, structure-based drug design allowed for the development of two more categories of N-terminal Hsp90 inhibitors. The first, synthetic purine analogs, target the unique conformation ATP takes within Hsp90's GHKL-ATPase site (e.g. HSP990 and PU-H71) [58, 59]. The second, benzamide containing compounds, are a set of very structurally diverse compounds which contain a benzamide moiety (e.g. XL888) [60].

Unfortunately, despite all the advancements made in N-terminal Hsp90 inhibition as a treatment for cancer, to date none of the N-terminal Hsp90 inhibitors have made it through clinical trials (https://clinical trials.gov, June 2022). The lack of success in clinical trials is primarily attributed to the fact that treatment with N-terminal Hsp90 inhibitors leads to the induction of the heat shock response. As described previously, this pro-survival stress pathway leads to the induction of multiple heat shock proteins and is detrimental to clinical success.

C-terminal inhibitors of Hsp90

The first C-terminal Hsp90 inhibitors were discovered unexpectedly by the Neckers' lab [61]. At the time it had been shown that geldanamycin and radicicol inhibit Hsp90 by binding to the atypical N-terminal ATP-binding site, and the ATP-binding site is highly conserved between bacterial DNA gyrase and Hsp90. This led the Neckers' lab to test coumarin containing antibiotics novobiocin (known to target the ATP-site of DNA gyrase), clorobiocin, and coumermycin A1 as novel N-terminal Hsp90 inhibitors. Novobiocin immobilized to Sepharose was used to affinity purify full-length, and a truncated form of Hsp90 consisting of only the mid- and C-terminal domains. However, it did not purify a

truncated Hsp90 consisting of only the N-terminal domain. Novobiocin depleted Hsp90 dependent clients (Her2, p53, Raf-2, and v-src) in a dose-dependent manner [61].

To date, there have been no published crystal structures of drug bound to the C-terminus of Hsp90 and there is conflicting conclusions on the binding site. A novobiocin derivative was used to elucidate the C-terminal binding site by photo-affinity labelling followed by LC-MS/MS [62]. In addition, three lab groups have attempted to determine the C-terminal binding site through computer prediction modeling [63-65].

Inhibitors of the Hsp90-co-chaperone interactions

As stated previously, Hsp90 has more than 20 reported co-chaperones which assist in its chaperoning function. Therefore, in addition to inhibiting Hsp90 by direct targeting, chaperone function can be inhibited by preventing the association of key co-chaperones to the complex (Reviewed in David Bickel and Holger Gohlke, 2019)[?]. Depending on the co-chaperone targeted, a smaller, more specific subset of Hsp90 clients can be altered [66]. Key co-chaperones that have been investigated for targeted inhibition include Cdc37 [67-69], and p23[70-72] (Table 1.1). Cdc37 is required for the maturation of multiple classes of protein kinases, and p23 is required for the stabilization of steroid hormone receptors (Table 1.1).

Evidence as inhibitors of the Hsp90 chaperone complex

Clorobiocin

Clorobiocin is an aminocoumarin antibiotic isolated from multiple strains of *Streptomyces*. There were three observations made when first concluding that clorobiocin is a Hsp90 inhibitor [61]. First, clorobiocin is structurally similar to novobiocin, and

coumermycin A1. Second, free clorobiocin competes for Hsp90 in cell lysate, preventing the binding of Hsp90 to novobiocin-Sepharose beads in a dose-dependent manner. Third, clorobiocin depletes Hsp90 dependent clients ErbB2 and Raf-1in a dose-dependent manner, without inducing the Hsc70. In a later study, clorobiocin was shown to provide proteolytic protection of the Hsp90 C-terminal domain against V8 protease [62].

Coumermycin A1

Coumermycin A1 is an aminocoumarin antibiotic isolated from actinomycetes. There were three observations made when first concluding that coumermycin A1 is a Hsp90 inhibitor [61]. First, coumermycin A1 is structurally similar to novobiocin and clorobiocin. Second, free coumermycin A1 in cell lysate was shown to compete for Hsp90 binding and prevent its association to novobiocin-Sepharose beads in a dose-dependent manner. Third, coumermycin A1 was shown to deplete Hsp90 dependent clients ErbB2 and Raf-1 in a dose-dependent manner.

Derrubone

Derrubone is an isoflavone isolated from *Derris robusta.* There were four observations made when first concluding that derrubone is a Hsp90 inhibitor [73]. First, derrubone was shown to prevent Hsp90 refolding of firefly luciferase in a dose-dependent manner. Second, derrubone inhibited the maturation of Hsp90-dependent kinase HRI. Third, derrubone degraded Hsp90 dependent client Her2 in a dose-dependent manner in ELISA assay. Fourth, derrubone treated MCF-7 cells depleted Hsp90-dependent clients Raf, Her2, ER, and AKT in dose-dependent manner assayed by Western blot.

Gambogic acid

Gambogic acid is a xanthonoid isolated from *Garcinia hanburyl*. There were four observations made when first concluding that gambogic acid is a Hsp90 inhibitor [74]. First, gambogic acid depleted Hsp90-dependent clients Her2, Raf, and Akt in a dose-dependent manner assayed by Western blot. Second, gambogic acid inhibited the co-immunoadsorption of HRI with Hsp90, Hsp70, and Cdc37. Third, gambogic acid inhibited HRI maturation. Fourth, binding of gambogic acid and Hsp90 were characterized by surface plasmon resonance.

Garcinol

Garcinol is a polyisoprenylated benzophenone isolated from *Garcinia indica*. Garcinol was first identified as putative inhibitor of Hsp90 in a high throughput screening of natural products. In that study three observations were made concluding garcinol is a Hsp90 inhibitor [75]. First, garcinol inhibited luciferase refolding. Second, garcinol inhibited Hsp90 dependent HRI maturation. Third, garcinol depleted Hsp90 dependent clients p-Akt, Cdk6, and Her2 in a dose-dependent manner assayed by Western blot.

β-lapachone

β-lapachone is an ortho-naphthoquinone isolated from *Handroanthus impetiginosus*. β-lapachone was identified as putative inhibitor of Hsp90 in a high throughput screening of natural products inhibiting luciferase refolding [75]. A later study showed that β-lapachone induces Hsp90-cleavage by oxidative stress, thus destabilizing and depleting Hsp90-dependent clients Akt, Cdk4, Her2, Raf-1, and VEGFR-2 [76]. This Hsp90 cleavage is not conserved with N-terminal inhibition by 17-AAG.

α-mangostin

α-Mangostin is an xanthone isolated from *Garcinia mangostana.* α-mangostin was identified as putative inhibitor of Hsp90 in a high throughput screening of natural products inhibiting luciferase refolding [75]. α-Mangostin has been shown to promote cell cycle arrest and induction of apoptosis in multiple cancer cell lines [77, 78].

Ailanthone

Ailanthone is a pentacyclic diterpene lactone isolated from *Ailanthus altissima.* Ailanthone is a well-reviewed anti-cancer compound that has been characterized to have effects on multiple cancer pathways in multiple cancer types [79]. Ailanthone has been reported as an inhibitor of Hsp90 co-chaperone p23 on the basis of five observations [70]. First, inhibition of luciferase refolding. Second, depletion of the Hsp90 client androgen receptor in a dose-dependent manner. Third, inhibition of heat shock proteins 40, 70, and 90 associations to androgen receptor by immunoprecipitation. Fourth, inhibition of p23 binding to Hsp90 by immunoprecipitation. Fifth, SPR profiling of ailanthone-p23.

Celastrol

Celastrol is a quinone methide triterpene isolated from the famous Chinese Thunder God Vine (*Tripterygium wilfordii*) whose root pulp contains multiple natural compounds used to treat a variety of diseases. Celastrol has been characterized to induce the heat shock response [80]. Celastrol cytotoxicity stems from non-specific thiol reactive chemistry [81]. Celastrol is quite the controversial inhibitor of Hsp90 chaperone complex with conflicting reports of the ability to target Hsp90 co-chaperones Cdc37, and p23.

Celastrol was reported as an inhibitor of Hsp90 co-chaperone Cdc37 based on four observations [82]. First, celastrol inhibited the immunoprecipitation of Cdc37, but not HOP

to Hsp90 to a greater extent than geldanamycin. Second, celastrol did not inhibit the p23-Hsp90 complex by immunoprecipitation. Third, celastrol depleted Hsp90-dependent clients Akt, and Cdk4 in a dose-dependent manner. Fourth, celastrol was molecularly docked to Hsp90, and Cdc37-Hsp90 complex.

Celastrol was reported as an inhibiter of Hsp90 co-chaperone p23 based on four observations [71]. First, celastrol induced Hsp90-dependent client depletion of Akt, ChK1, PR, and Raf in a dose-dependent manner. When compared to the geldanamycin positive control, celastrol depleted PR at a lower dose and more quickly when assayed over a time course. Second, Hsp90 ATPase activity was not inhibited by the presence of celastrol compared to geldanamycin at the same concentrations. Third, celastrol inhibited the immunoprecipitation of p23 by Hsp90. Fourth, celastrol induced p23 to form amyloid-like fibrils.

Daurisoline

Daurisoline is a bis-benzylisoquinoline alkaloid isolated from *Rhizoma Menispermi*. Daurisoline has been reported as a direct inhibitor of Hsp90 based on four observations [83]. First, daurisoline depletes Hsp90-dependent clients β-catenin, cyclin D1, and c-myc as assayed by Western blot and quantitative proteomics. Second, daurisoline-Hsp90 binding was characterized by isothermal titration calorimetry. Third, daurisoline inhibited the immunoprecipitation of β-catenin by Hsp90. Fourth, daurisoline provided protease protection by drug affinity responsive target stability (DARTS) assay.

Mass spectrometry

Mass spectrometry (MS) has become an essential analytical technique for scientists wanting to compare changes in protein levels induced by compound treatment. Mass spectrometers work by measuring the mass-to-charge ratio (m/z) of molecules in the sample, peptides in our case. Mass spectrometers all consist of three components: an ion source, a mass analyzer, and an ion detector.

The ion source is responsible for converting peptides from a liquid into a gas-phase ion that is capable of being manipulated by electric and magnetic fields within the mass spectrometer. There are multiple types of ion sources, broadly categorized into hard or soft ionization. In this study, we used electrospray ionization, a soft ionization technique, which uses high voltage (~3000 V) applied to a stainless-steel tip to aerosolize peptides separated by high-pressure liquid chromatography (HPLC).

The mass analyzer is responsible for separating ions according to their m/z. There are many types of mass analyzers which use dynamic or static, and electric or magnetic fields to manipulate the ions generated by the ion source. These variables impart strengths and weaknesses for each mass analyzer. Many modern mass spectrometers consist of two or more mass analyzers. The Orbitrap Fusion Tribrid mass spectrometer (Thermo) used in this study contains a quadruple mass filter, Orbitrap mass analyzer, and a linear ion trap mass analyzer.

The coupling of multiple mass analyzers allows for completing tandem mass spectrometry (MS/MS or MS^2). In this technique, the first mass analyzer (MS1) separates the ions by their m/z, deemed parent ions. Parent ions are filtered from the MS^1 and further fragmented into smaller ions, deemed daughter ions. These daughter ions are then separated

by m/z and detected by the second mass analyzer (MS2). LC-MS/MS is the most dominate technique for characterizing proteomic changes.

The ion detector is responsible for recording and generating report(s), called mass spectrum (spectra), which graph the m/z of ions versus their relative abundance. Many mass analyzers are coupled with ion detectors.

Quantitative proteomics

Proteomics is the large-scale study of proteins at the level of the proteome. Quantitative proteomics characterizes the relative or absolute changes in protein expression between two or more biological samples. Mass spectrometry-based quantitative proteomics has become a pivotal technique in small molecule drug discovery with the ability to identify, and validate a compound's effect on target protein/pathway(s) [84].

Quantitative proteomics is completed using either label-free or label-based quantitation methods. Label-based methods allow for the pooling of multiple biological samples early in the proteomics workflow. Label-based quantitation methods use stable heavy isotopes of H, C, N, and O to label proteins or peptides [85]. There are a large number of labelling technologies available, in this study we used Tandem Mass Tags (TMT, Thermo).

The TMT are isobaric labels for peptides, meaning they have the same mass and chemical structure, that allows for the pooling of 2-18 samples [86]. All isobaric labels are made of three distinct groups: a peptide reactive group, a mass normalizer, and a mass reporter. For the TMT kit we used, the peptide reactive group was composed of an amine-reactive N-hydroxysuccinimide ester group. This group reacts with the N-terminus of

peptides and lysine residues. The mass reporter group is comprised of various combinations of light or heavy ^{13}C and ^{15}N isotopes unique to each labeling "channel" of the kit. The reporter group is broken by either ETD or HCD fragmentation in the mass spectrometer, and allows for the quantification of the each of the samples. The mass normalizer group is a spacer group between the reporter and peptide reactive groups. The mass normalizer is also comprised of light and heavy isotopes, balancing with the mass reporter group so that each labeling channel is the same mass.

As stated above, isobaric labels allow for the pooling of multiple samples up to the number of channels provided by the kit. The pooling of samples provides multiple advantages: First, increasing the throughput of each mass spectrometry experiment. Where before each sample would have to be an independent experiment, the amount samples quantified in a single experiment is now limited to the number of channels in the kit. Second, is by reducing technical variability between experiments as the same peptides in multiple experiments will all orthogonally fractionate, and elute off the HPLC together. Furthermore, the co-elution of peptides from pooling to reporter fragmentation yields fewer missing values between biological samples, thus increasing statistical validation of proteomic changes.

Unfortunately, isobaric labeling has two major disadvantages: (1) the cost of reagents, and (2) ratio compression. To address the cost of labeling reagents Zecha *et al.* completed a study optimizing TMT labeling conditions [87]. In this study they compared the labeling efficiencies at multiple TMT reagent to peptide ratios. What they found was the vendor suggested ratio of 8:1 (reagent to peptides) is over reported, showing equal labelling efficiencies at 4:1, 2:1, and 1:1 across multiple labs. Additionally, they showed that by maintaining the molar concentration ratios (reducing the reaction volume), labeling could be

efficiently completed on lower amounts of peptides. Thus, further reducing the amount of TMT reagent required for each sample. Based on these results we completed our study following the procedures published by Zecha *et al.* at a TMT reagent to peptide ratio of 3:1.

The struggles of ratio compression in isobaric labeling techniques is well documented in the literature and universal to all mass spectrometers [88-90]. Ratio compression leads to reduced accuracy and precision. This issue arises from the fact many peptides are co-isolated in addition to the target peptide of interest. Since the mass reporter groups (tags) are the same for each sample, these contaminating peptides provide reporter fragments that increase the background noise. In order to alleviate ratio compression we followed the synchronous precursor selection (SPS) MS3 (MS/MS/MS) protocol laid out by McAlister *et al*. [91]. Briefly, this technique uses the MS1 cycle to detect the parent peptide of interest. Then, the MS2 cycle fragments and sequences the parent. The top ten most abundant m/z fragments data is stored. The parent peptide is then re-isolated and fragmented. Following fragmentation, all other peptides besides the top ten are ejected using energetic excitation. With the contaminating peptides removed the ten peptides of interest can be sent to the HCD cell for reporter fragmentation.

CHAPTER II

CHARACTERIZATION OF COMPOUNDS FOR HSP90 INHIBITION MOTIFS

Introduction

As previously described in the literature review, N-terminal Hsp90 inhibitors have a highly conserved, well characterized impact on protein expression with: (1) the depletion of Hsp90 dependent kinases, and (2) the induction of the heat shock response. In contrast, C-terminal Hsp90 inhibitors deplete Hsp90 clients without the induction of the heat shock response. Traditionally, one of the most common methods to characterize these modalities is to assay treated cell culture lysates by Western blotting for depletion of known Hsp90 dependent kinases, and either induction of Hsp90 or Hsp70. Recently, advances in mass spectrometry and proteomic approaches have allowed for more robust characterization of N-terminal Hsp90 inhibition/inhibitors. To date, no proteomic profiling has been completed on C-terminal Hsp90 inhibitors.

In this study, we sought to elucidate the proteomic fingerprint of C-terminal Hsp90 inhibition. We constructed a compound panel consisting of a N-terminal Hsp90 inhibitor, two putative Hsp90-cochaperone inhibitors, eight putative C-terminal (or not designated)

Hsp90 inhibitors, and a non-Hsp90 related chemotherapeutic and tested the N- and C-terminal Hsp90 inhibition models for these compounds.

Materials and Methods

Compounds

The following compounds were dissolved in DMSO to make 50 mM stocks, aliquoted, and stored at -80 °C: AUY922 (Selleck chemicals S1069), ailanthone (Cayman Chemical Company 29194), α-mangostin (National Cancer Institute 30552), β-lapachone (Selleck chemicals S7261), celastrol (Selleck chemicals S1290), coumermycin A1 (National Cancer Institute 107412), clorobiocin (National Cancer Institute 227186), daurisoline (Cayman Chemical Company 29628), derrubone (Dr. Blagg, The University of Notre Dame), gambogic acid (Selleck chemicals S2488), garcinol (Cayman Chemical Company10566), and paclitaxel (Selleck chemicals S1150).

Antibodies

The following primary antibodies were diluted in Tris-buffered saline-Tween20 solution (20 mM Tris, 150 mM NaCl, and 0.1 % (v/v) Tween-20) with 1 % (w/v) skim milk (bioPlus): anti-human poly-ADP ribose polymerase (PARP) (Cell Signaling Technology 9542S, 1:1,000), anti-human heat shock protein 70 (Hsp70) C92F3A-5 (Santa Cruz SC-66048, 1:1,000), anti-human lymphoid cell kinase (LCK) (polyclonal ascites fluid as described [92], 1:1,500), anti-human cyclin-dependent kinase 6 (Cdk6) (Abcam ab133327, 1:50,000), anti-human cyclin-dependent kinase 1 (Cdk1) (Abcam

ab124821, 1:25,000), and anti-human β-actin (Sigma A5441, 1:10,000). Secondary antibodies: peroxidase conjugated goat anti-rabbit IgG (Jackson ImmunoResearch 111-035-045, 1:50,000) and peroxidase conjugated goat anti-mouse IgG (Jackson ImmunoResearch 111-035-003, 1:50,000).

Cell culture

Jurkat E6-1 (ATCC) cells were cultured in a humidified 37 °C incubator in the presence of 5 % CO_2. Cells were cultured in RPMI-1640 medium (Corning) supplemented with 10 % (v/v) fetal bovine serum (Atlanta biologicals) and 50 U/mL penicillin and 50 µg/mL streptomycin (Gibco). Cells were allowed to grow to densities between 100,000 and 1,000,000 cells/mL in 25 mL complete growth medium in a T-75 cell culture flasks (Falcon), and were propagated for a maximum of 25 passages.

Cell compound dosing and lysate preparation

Cells were monitored for 48 hours before seeding to ensure proper doubling times. A concentrated (~1,000,000 cells/mL) T-75 culture flask was diluted to 200,000 cells/mL with complete growth medium and used to seed T-25 culture flasks (Fischer) (8 mL cell suspension). Then, 24 hours after seeding, cells were treated with either DMSO or compound. After an additional 24 hours, cells were collected by centrifugation, and washed once with room temperature phosphate buffered saline (137 mM NaCl, 2.7 mM KCl, 10 mM Na_2HPO_4, 2 mM K_2HPO_4 at pH 7.6). Supernatants were vacuum aspirated and cell pellets were lysed in 300 µL 8 M urea, 100 mM TEAB pH 8.5, 10 mM DTT, and 2 mM $MgCl_2$ for 15 minutes with aggressive vortexing at room temperature. DNA was sheared using a sonicator (Bioruptor, Diagenode) on high setting, using cycles of 15

seconds on/off for 12.5 minutes at 4 °C. Lysates were then treated with 25 U/mL Benzonase (Millipore 70746-4) for 15 minutes at room temperature, and then stored at -80 °C.

Determining lysate concentration

Lysate concentrations were assayed by tryptophan fluorescence [93]. Briefly, L-tryptophan (VWR 97064-004) standards were dissolved in urea lysis buffer. Standards and lysates were loaded on a black 96 well microplate (Greiner Bio-One 655209) in experimental triplicates, and read on a Synergy H1 (Agilent-BioTek) microplate reader with excitation 295 nm, emission 350 nm. Lysate concentration was determined by the average of the technical replicates (n=3).

$$[Lysate]\left(\frac{\mu g}{\mu L}\right) = ([\text{Tryptophan}](\frac{\mu g}{\mu L})*100)/1.17$$

Protein digestion

Disulfide bonds of lysates were reduced with 5 mM TCEP at room temperature for 30 minutes, and then were alkylated in the dark at room temperature with 10 mM iodoacetamide for 20 minutes. Lysates were diluted to 2 M urea, 100 mM Tris pH 8.0. Proteins were digested with 4 µg trypsin/LysC at 37 °C overnight after which another 2 µg trypsin/LysC were added for 6 hours at 37 °C. Digests were acidified to contain 1 % trifluoroacetic acid (TFA). Peptides were desalted using C18 columns as recommended by the manufacturer (Pierce Cat 89852) using 0.1 % TFA washing solution and 0.1 % TFA, 50 % acetonitrile for peptide elution. Elutes were frozen at -80 °C overnight and then dried by vacuum centrifugation.

Western bloting

Lysates (10 µg in SDS-PAGE sample buffer) were electrophoresed at 15 mA through the stacking gel and 30 mA through separating gel. Gels were transferred to PVDF membrane (BioRad #1620177) using a semi-dry transfer apparatus (BioRad). Membranes were blocked with 5 % skim milk in Tris-buffered saline for 1 hour. Membranes were then incubated overnight with primary antibodies at 4 °C. Membranes were washed and then incubated with secondary antibodies for 2 hours at room temperature. Membranes were again washed in Tris-buffered saline-Tween20 and Tris-buffered saline, and visualized with SuperSignal West Femto chemiluminescent substrate (Thermo) using a BioRad ChemiDoc. The ChemiDoc was set to take multichannel exposures, channel 1: Chemiluminescent 647SP, no light, set to auto rapid exposure 1x1 (highest resolution). Channel 2: Colorimetric blot 590/110, White epi, set to auto rapid exposure.

Densitometry

Western blot band densities were measured using Image Lab (BioRad). For each experiment, variable lysate loading was accounted for by normalizing actin intensities using the Image Lab software. Briefly, an actin normalization factor was calculated by dividing the actin band intensity from the DMSO treated lane by each of the drug treated lanes for the dose series. This generated a lane specific normalization factor that was applied to the band intensities of the other proteins in the lane (PARP, Hsp70, Lck, Cdk6, and Cdk1).

$$Actin\ normalization\ factor = \frac{Intensity\ DMSO\ treated\ actin\ band}{Intensity\ drug\ treated\ actin\ band}$$

PARP-cleavage was calculated by taking one minus the ratio of full length PARP signal over the sum of total PARP signal and multiplying by 100 %.

$$PARP - cleavage = \left(1 - \left(\frac{Full\ legnth\ PARP}{Full\ length\ PARP + Cleaved\ PARP}\right)\right) * 100\ \%$$

Band densities were plotted using GraphPad Prism 9, where in each point indicated mean for three biological replicates, and error bars represent one standard deviation. Trendlines were fit to data using a sigmoidal function in GraphPad Prism 9.

TMT labelling and orthogonal fractionation

To determine concentration an aliquot of trypsinolytic peptides were assayed by peptide fluorescence (Pierce Cat 23290) following manufactures protocols. A second aliquot of peptides were reconstituted in 50 mM TEAB pH 8.5 to a concentration of 1.8 µg/µL. TMT6-plex reagents were dissolved in anhydrous acetonitrile to a concentration of 20 µg/µL. Peptide labelling was completed using 100 µg TMT reagent and 36 µg peptides. The TMT6-plex reagent kit was divided in half between corresponding DMSO (control) lysates and compound-treated lysates. The first three channels were reserved for DMSO-treated biological replicates 1-3 and the fourth through sixth channels for compound-treated biological replicates 1-3. Peptides and TMT reagent were vortexed, quickly centrifuged, and then incubated for 1 hour at room temperature. The labelling reaction was then quenched with 5 % hydroxylamine and incubated at room temperature for 15 minutes. Following quenching, 12 µL of labelled peptides from each channel were

pooled (16.7 µg per channel for ~100 µg peptide total) and brought to 300 µL with 0.1 % TFA. Orthogonal fractionation was completed using high-pH reversed-phase peptide fractionation spin columns (Pierce 84868). For this, the column was conditioned by washing with acetonitrile and 0.1 % TFA. TMT labelled peptides were bound to the column and washed three times with 5 % (v/v) acetonitrile in 0.1 % triethylamine. Subsequently, nine fractions were collected with 7.5, 10, 12.5, 15, 17.5, 20, 22.5, 25, 27.5, or 60 % (v/v) acetonitrile in 0.1 % triethylamine. Fractions were frozen at -80 °C overnight and then dried by vacuum centrifugation.

Liquid chromatography and mass spectrometry

TMT-labelled fractions were analyzed on an Easy-nCL 1200 (Thermo) HPLC coupled to an Orbitrap Fusion Hybrid mass spectrometer (Thermo). Briefly, peptide fractions were dissolved in solution A (0.1% aqueous formic acid), and then separated on a 75-um x 50-cm PepMap C18 column (Thermo catalog 164942) plumbed in a vented trap configuration. The column was developed using a 3-hour non-linear gradient of 5-34 % solution B (80:20:0.1 acetonitrile/water/formic acid) in solution A at a flow rate 250 nL/min. Eluting peptides were ionized in a Nanospray Flex ion source (Thermo) by application of 1900V to a stainless-steel needle at the column terminus.

The mass spectrometer was operated in positive ionization mode. Gas phase peptides were analyzed using a top-speed data-dependent scan cycle, in which parent ions were measured in the FT Orbitrap sector. For MS/MS, ions were transferred to the IT sector for CID fragmentation and ion trap analysis. TMT reporter fragments were generated using an SPS-MS3 [91] scan method, wherein the parent ions were fragmented

by CID in the IT, and the 10 most intense MS2 fragments were transferred to the HCD cell for high-energy fragmentation, followed by FT Orbitrap analysis of the TMT reporter ions.

Database searching

Instrument RAW files were searched using MaxQuant (version 2.0.3.0, [94]) against a human reference proteome from Uniprot (78,139 human proteins accessed September 24, 2021). MaxQuant searches were completed using largely default settings with supplemental changes as follows: the reporter ion MS3 module was selected, specifying 6-plex TMT labeling and correcting for TMT lot-specific factors. A reporter mass tolerance of 0.003 was specified, and TMT signals were measured as ratios to the reference channels (channels 1, 2, and 3 i.e. the DMSO lysates). Carbamidomethylation of cysteine was selected as a fixed modification. Oxidation of methionine, acetylation of the protein N-terminus, glutamine cyclization to pyro-glutamate, and deamidation of asparagine and glutamine were selected as variable modifications for both identification and quantification. Trypsin/P was selected for digestion with two missed cleavages allowed.

Data normalization and significance testing

MaxQuant output was analyzed using Perseus (version 1.6.5.0, [95]). Reporter corrected ratios were filtered to remove contaminants and decoy proteins. Ratios were log2 transformed, and then normalized to the median ratio observed in each individual experiment. Significant differences in protein expression were determined by a two-sided two-sample Student's t-test. *P*-value significant thresholds were determined by the

Benjamini-Hochberg procedure using a false discovery rate of 0.05. Treated and Control groups were then averaged to obtain a median ratio, and then subtracted for the median log2(Treated/Control) value. Changes in expression between log2 +/- 0.322 (25 % fold-change) were not regarded as significant irrespective of *p*-value.

Probes of Hsp90 inhibition

To complete comparisons of our compound panel on the basis of Hsp90 inhibition, we developed panels of proteins to serve as probes of Hsp90 inhibition. These probes consisted of a list of proteins known to have their expression altered by Hsp90 inhibition. The probe sets of Hsp90α, Hsp90β, and Hsp90α∩β (Hsp90α-β intersect, i.e. proteins that interact with both isoforms) interaction probes were manually curated from BioGRID [96], The Database of Interacting Proteins (DIP) [97], Human Protein Reference Database (HPRD) [98], IntAct [99], Literature-curated protein interaction datasets (LC) [100], Molecular INTeraction database (MINT) [101], and Hsp90 interactors list (https://www.picard.ch) by Maurie Balch. The Kinases probe set was obtained from [102]. The Hsf1-regulated probe set was obtained from [103]. Using these probe lists, we generated specifically targeted heatmaps and used them to compare our positive control AUY922 to panel compounds. Probes list provided in digital Appendix.

Bootstrapped hierarchical clustering

Hierarchical clustering and statistical testing of generated clusters was completed using the R package Pvclust [104]. The clustering used the log2(treated/control) data for each compound in our panel, Kline's compound panel, Voruganti's compound panel [105], and those obtained from the literature [106, 107] as indicated. In addition to the

distance methods provided by the package, we added a Pearson and Spearman function. Dendrograms used Pearson correlation for distance measurement, ward.D2 for agglomeration, and 1000 replicates for bootstrap resampling. Values on the edges are *p*-values (%). Red values are the approximately unbiased (AU) and green values are the bootstrapped probability (BP). According to the package creators, AU *p*-value is a better approximation compared to the BP value, as it is computed by the multiscale bootstrap resampling [104].

Results

To determine the appropriate dose range for each compound in our panel, Jurkat cells were treated along an eight-point dose series with DMSO (vehicle control) or with varying concentrations of compound for 24 hours, and assayed by Western blotting for cleavage of the apoptosis marker PARP. We saw inductions of PARP-cleavage greater than 80 % for 11 compounds in our panel at the highest dose used (Figures 2.2-2.12). In contrast, the well characterized N-terminal Hsp90 inhibitor AUY922 was observed to have an apparent plateau at ~60 % PARP-cleavage at the three highest doses (Figure 2.1). Based on these results we concluded that we had determined an appropriate, apoptosis constrained, dose range to characterize our drug panel.

To characterize induction of the heat shock response in our treated lysates, we used Western blotting to assay Hsp70 expression. Following literature precedents AUY922 and celastrol both induced Hsp70. AUY922 is an N-terminal Hsp90 inhibitor and the positive control of our compound panel, thus the induction of Hsp70 was to be

expected. This confirms the Hsp70 antibody can report the induction of heat shock response, and the AUY922 treatments were efficacious (Figure 2.1 Panel C). Celastrol induced Hsp70 reaching levels to 86 % of the AUY922-induced Hsp70 induction (Figure 2.4 Panel C). Also following literary precedence, reported C-terminal Hsp90 inhibitors gambogic acid, coumermycin A1, derrubone, garcinol, daurisoline, β-lapachone, and α-mangostin did not induce Hsp70 (Figure 2.6-2.12 Panel C). The chemotherapeutic paclitaxel did not induce Hsp70 (Figure 2.2 Panel C). The reported Hsp90-cochaperone inhibitor ailanthone did not induce Hsp70 (Figure 2.3 Panel C). More unexpectedly, 128 μM clorobiocin induced Hsp70 to 43 % of the levels induced by AUY922 positive control (Figure 2.5 Panel C). By definition of the C-terminal Hsp90 inhibition model, this suggested clorobiocin was not a C-terminal Hsp90 inhibitor.

The C-terminal Hsp90 inhibitor model demands that a C-terminal Hsp90 inhibitor should deplete Hsp90-dependent kinases. Therefore, we assayed our compound panel by Western blot for the depletion of Hsp90-dependent kinases Lck, Cdk6, and Cdk1. The N-terminal Hsp90 inhibitor AUY922 induced sigmoidal depletion of Lck, Cdk6, and Cdk1 (Figure 2.1 Panels D, E, and F). Unexpectedly, none of the other compounds in our panel caused comparable depletion of the kinases assayed. Clorobiocin was the only treatment that led to some kinase depletion, and this was observed for only two of the three kinases (Figures 2.5-2.12 Panels D, E, and F, Table 2.1). This unexpected kinase depletion phenotype prompted us to expand the set of reporter proteins by using a shotgun proteomics approach.

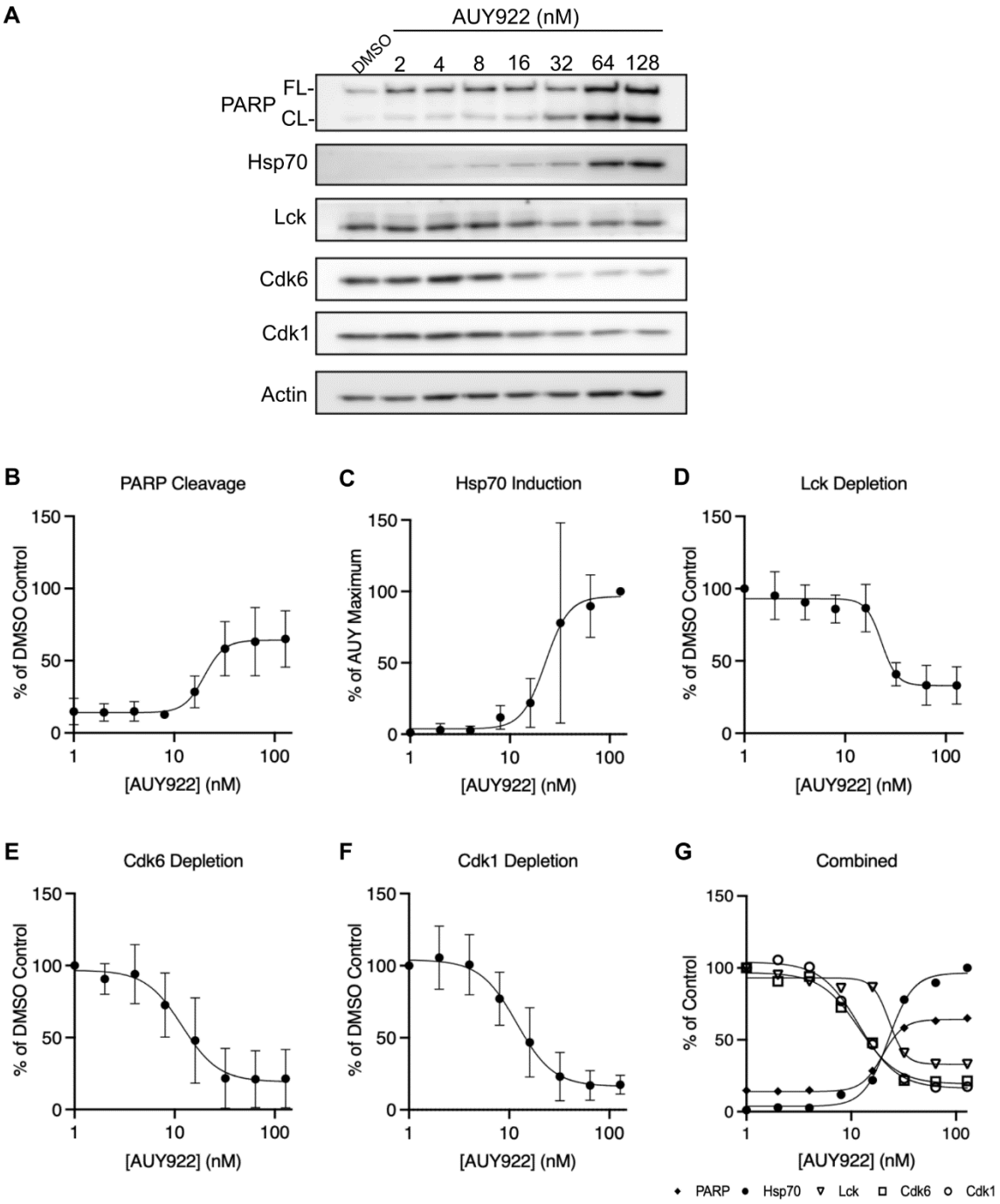

Figure 2.1. Effects of AUY922 on Jurkat cells. Jurkat cells were treated with DMSO or AUY922 as indicated for 24 hours and then lysed using 8 M urea as described in Methods. Panel A: A representative Western blot of indicated targets. Full length PARP indicated by FL- and cleaved PARP indicated by CL-. Panel B-F: Densitometry was completed for each Western blot target and normalized to actin. Points are the mean and error bars are one standard deviation of (n=3). Trendline was fit using GraphPad Prism 9 interpolate a standard curve: Sigmoidal, 4PL, X is concentration. Panel G: The mean points and trendlines for Panels B-F combined (◆ PARP-cleavage, ● Hsp70 induction, ▽ Lck depletion, ☐ Cdk6 depletion, ○ Cdk1 depletion).

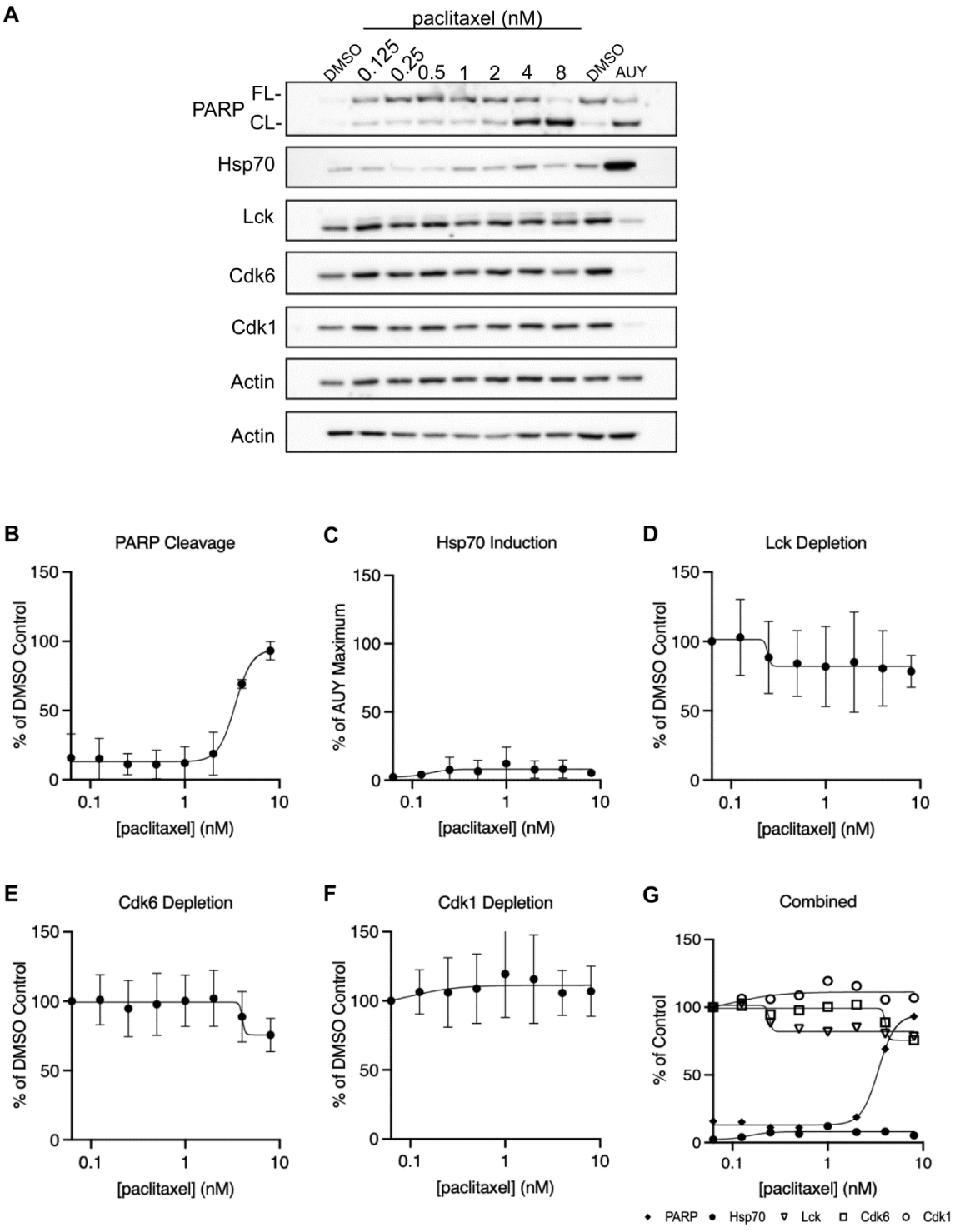

Figure 2.2. Effects of paclitaxel on Jurkat cells. Jurkat cells were treated with DMSO or paclitaxel as indicated for 24 hours. Cell lysates were prepared, and Western blot analysis was completed as previously described in **Figure 2.1** and Methods with DMSO and 128 nM AUY used as negative and positive controls. Panel A: A representative Western blot. Upper actin blot corresponds to PARP, Lck, Cdk6, and Cdk1. Lower actin blot corresponds to Hsp70. Panels B-F: Densitometries for indicated targets. Panel G: Panels B-F combined (◆ PARP-cleavage, ● Hsp70 induction, ▽ Lck depletion, □ Cdk6 depletion, ○ Cdk1 depletion).

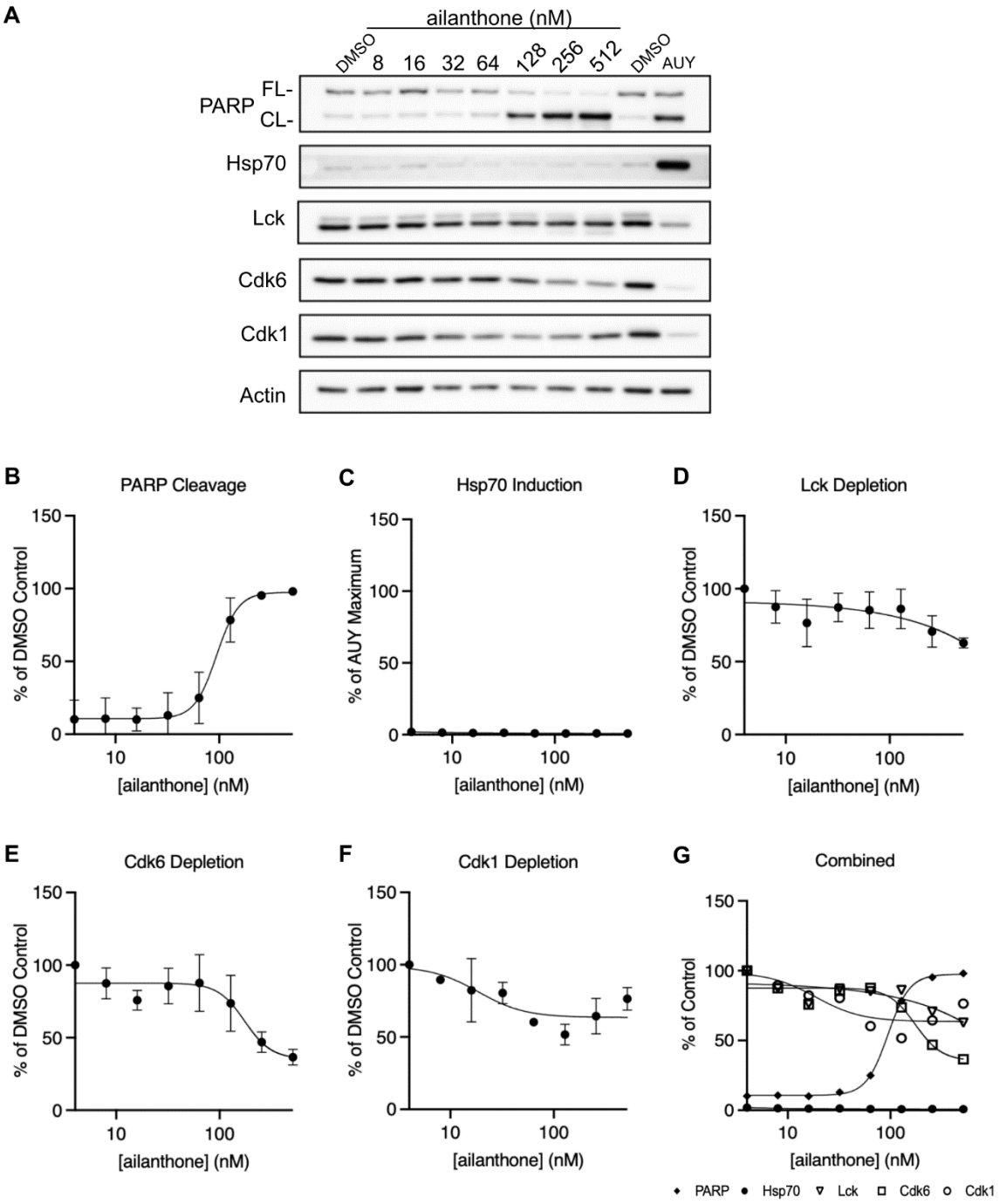

Figure 2.3. Effects of ailanthone on Jurkat cells. Jurkat cells were treated with DMSO or ailanthone as indicated for 24 hours as described previously in **Figure 2.2** and Methods, with DMSO and 128 nM AUY serving as negative and positive controls. Panel A: A representative Western blot. Panels B-F: Densitometries for indicated targets. Panel G: Panels B-F combined (◆ PARP-cleavage, ● Hsp70 induction, ▽ Lck depletion, □ Cdk6 depletion, ○ Cdk1 depletion).

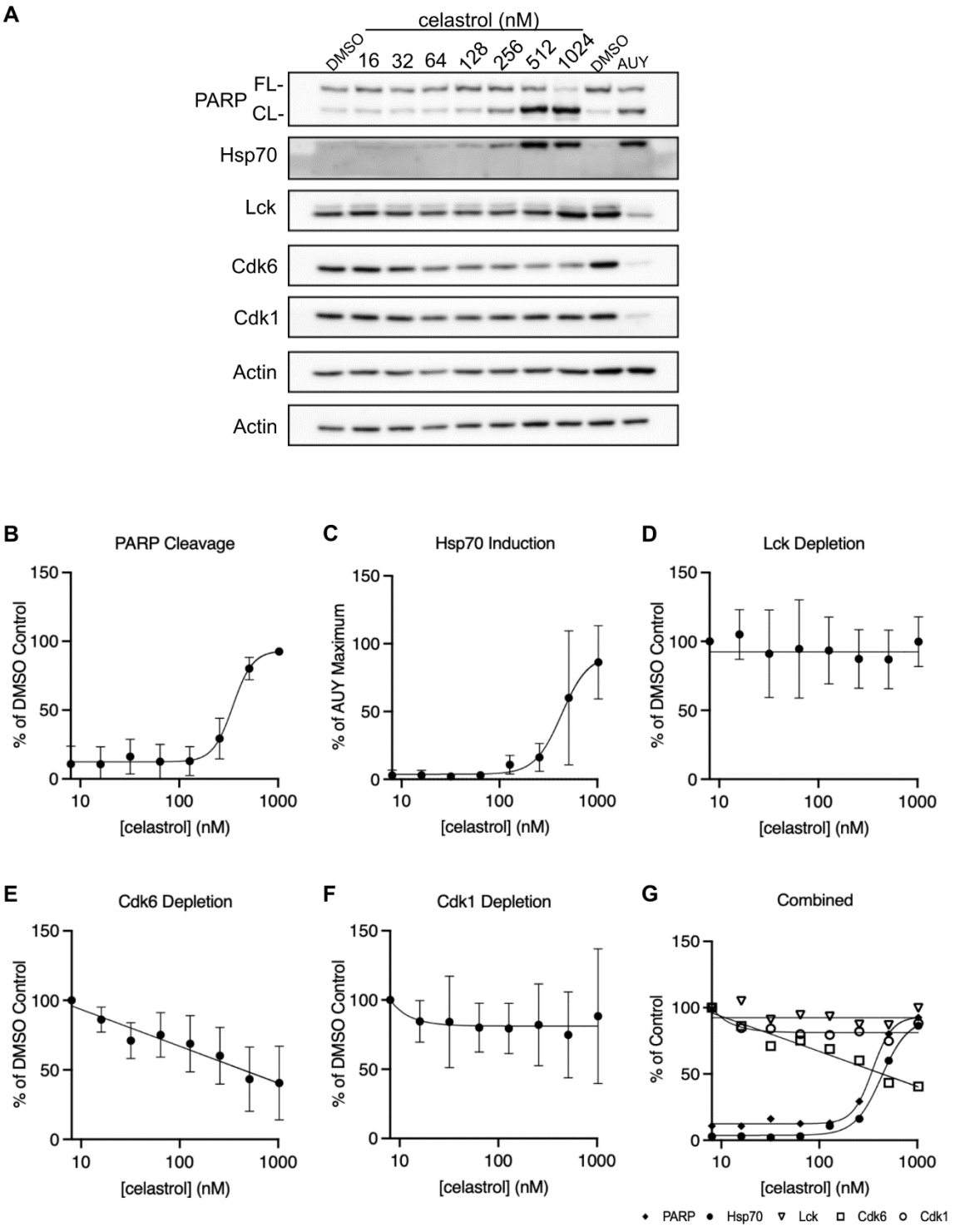

Figure 2.4. Effects of celastrol on Jurkat cells. Jurkat cells were treated with DMSO or celastrol as indicated for 24 hours as described previously in **Figure 2.2** and Methods, with DMSO and 128 nM AUY serving as negative and positive controls. Panel A: A representative Western blot. Upper actin blot corresponds to PARP, Hsp70, Cdk6, and Cdk1. Lower actin blot corresponds to Lck. Panels B-F: Densitometries for indicated targets. Panel G: Panels B-F combined (◆ PARP-cleavage, ● Hsp70 induction, ▽ Lck depletion, □ Cdk6 depletion, O Cdk1 depletion).

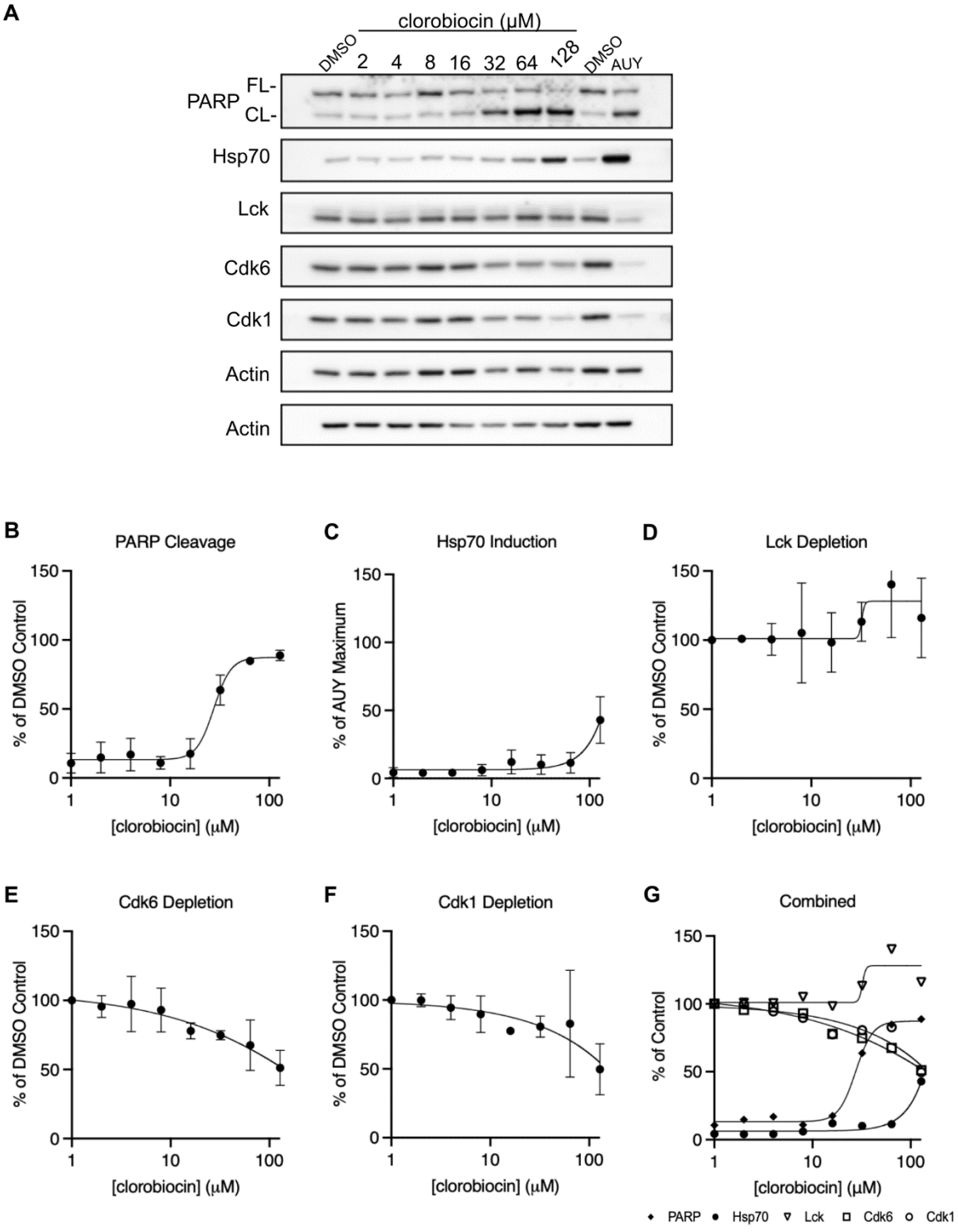

Figure 2.5. Effects of clorobiocin on Jurkat cells. Jurkat cells were treated with DMSO or clorobiocin as indicated for 24 hours as described previously in **Figure 2.2** and Methods, with DMSO and 128 nM AUY serving as negative and positive controls. Upper actin blot corresponds to PARP, Lck, Cdk6, and Cdk1. Lower actin blot corresponds to Hsp70. Panel A: A representative Western blot. Panels B-F: Densitometries for indicated targets. Panel G: Panels B-F combined (◆ PARP-cleavage, ● Hsp70 induction, ▽ Lck depletion, □ Cdk6 depletion, ○ Cdk1 depletion).

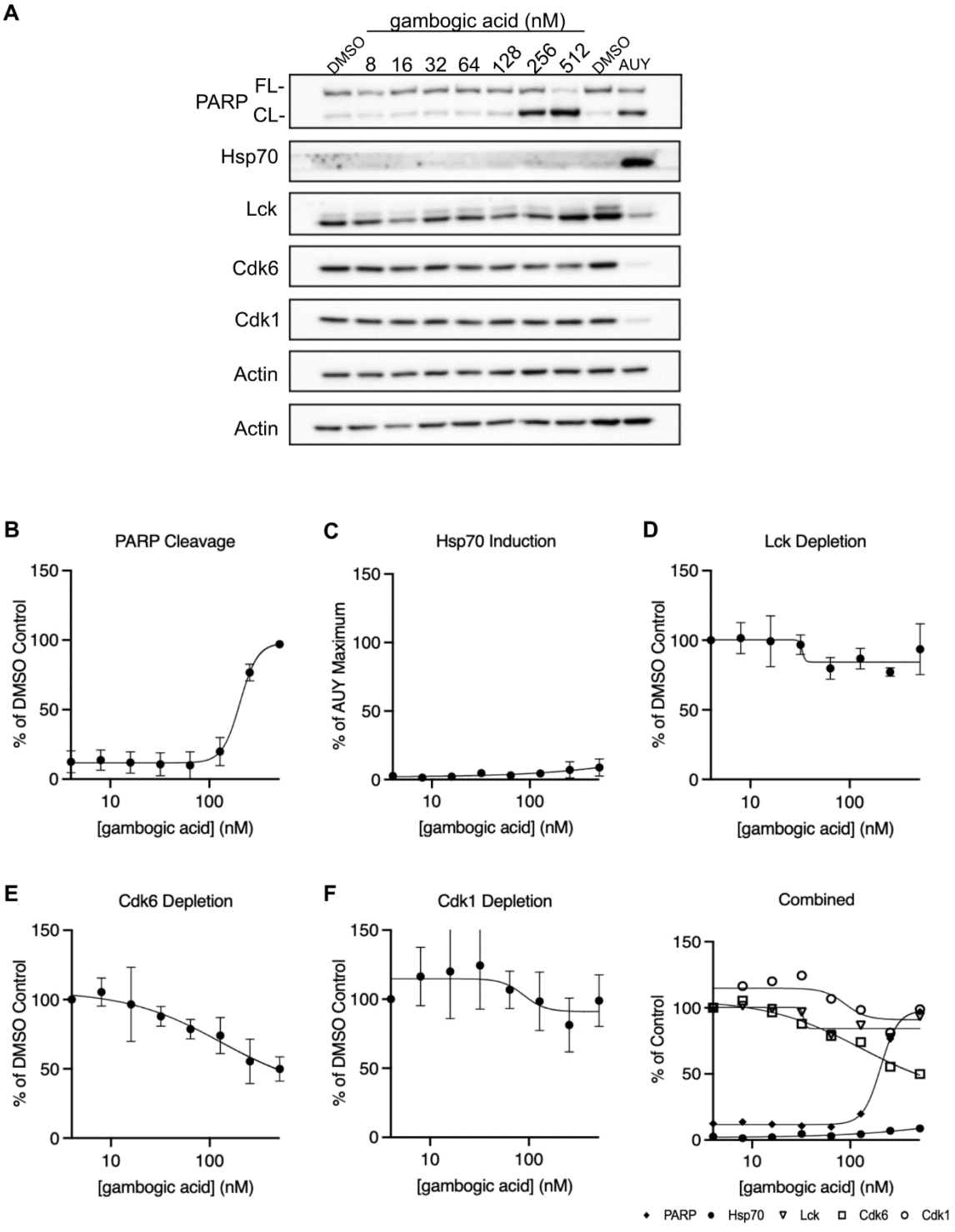

Figure 2.6. Effects of gambogic acid on Jurkat cells. Jurkat cells were treated with DMSO or gambogic acid as indicated for 24 hours as described previously in **Figure 2.2** and Methods, with DMSO and 128 nM AUY serving as negative and positive controls. Panel A: A representative Western blot. Upper actin blot corresponds to PARP, Cdk6, and Cdk1. Lower actin blot corresponds to Hsp70 and Lck. Panels B-F: Densitometries for indicated targets. Panel G: Panels B-F combined (◆ PARP-cleavage, ● Hsp70 induction, ▽ Lck depletion, □ Cdk6 depletion, ○ Cdk1 depletion).

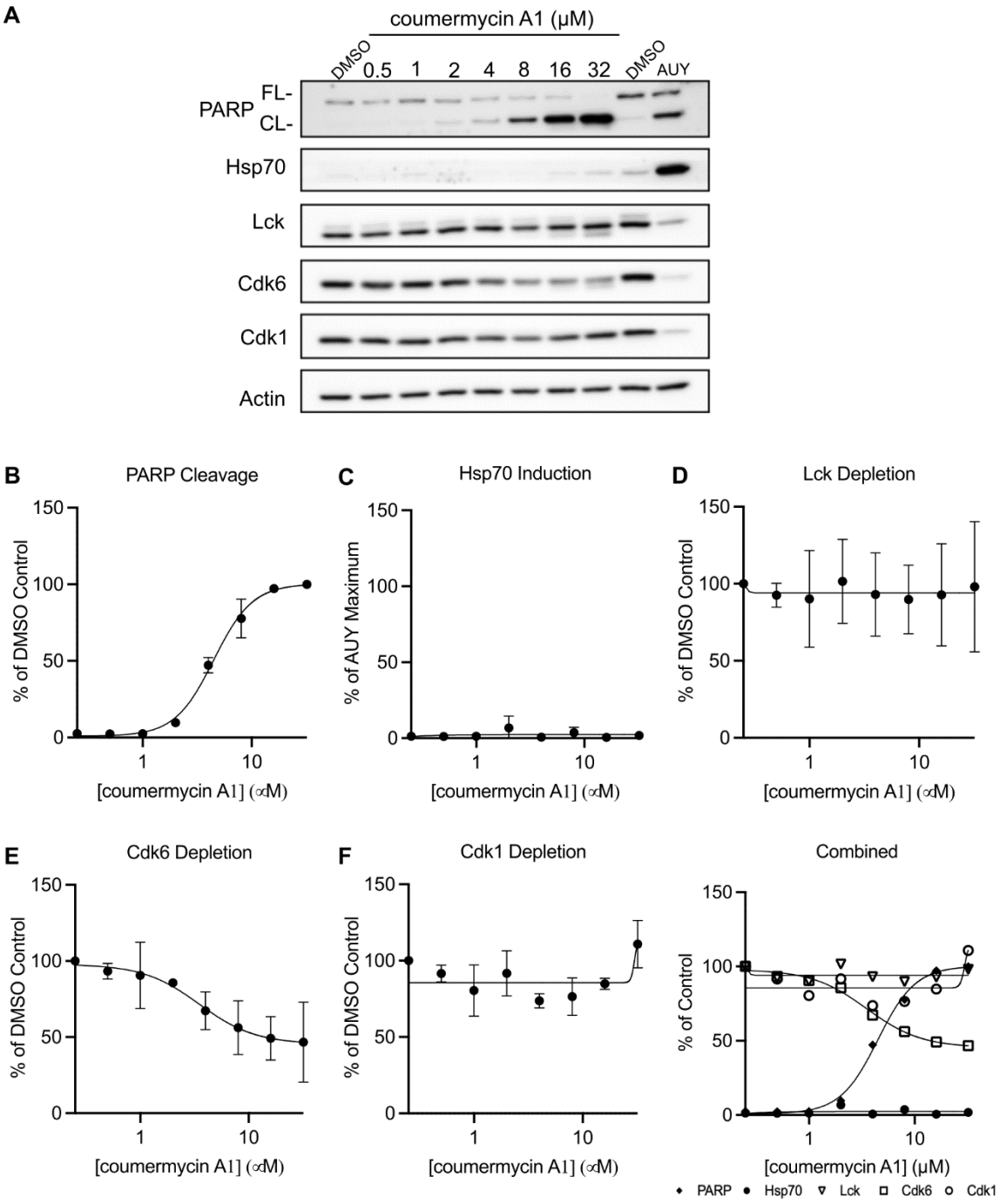

Figure 2.7. Effects of coumermycin A1 on Jurkat cells. Jurkat cells were treated with DMSO or coumermycin A1 as indicated for 24 hours as described previously in **Figure 2.2** and Methods, with DMSO and 128 nM AUY serving as negative and positive controls. Panel A: A representative Western blot. Panels B-F: Densitometries for indicated targets. Panel G: Panels B-F combined (◆ PARP-cleavage, ● Hsp70 induction, ▽ Lck depletion, □ Cdk6 depletion, ○ Cdk1 depletion).

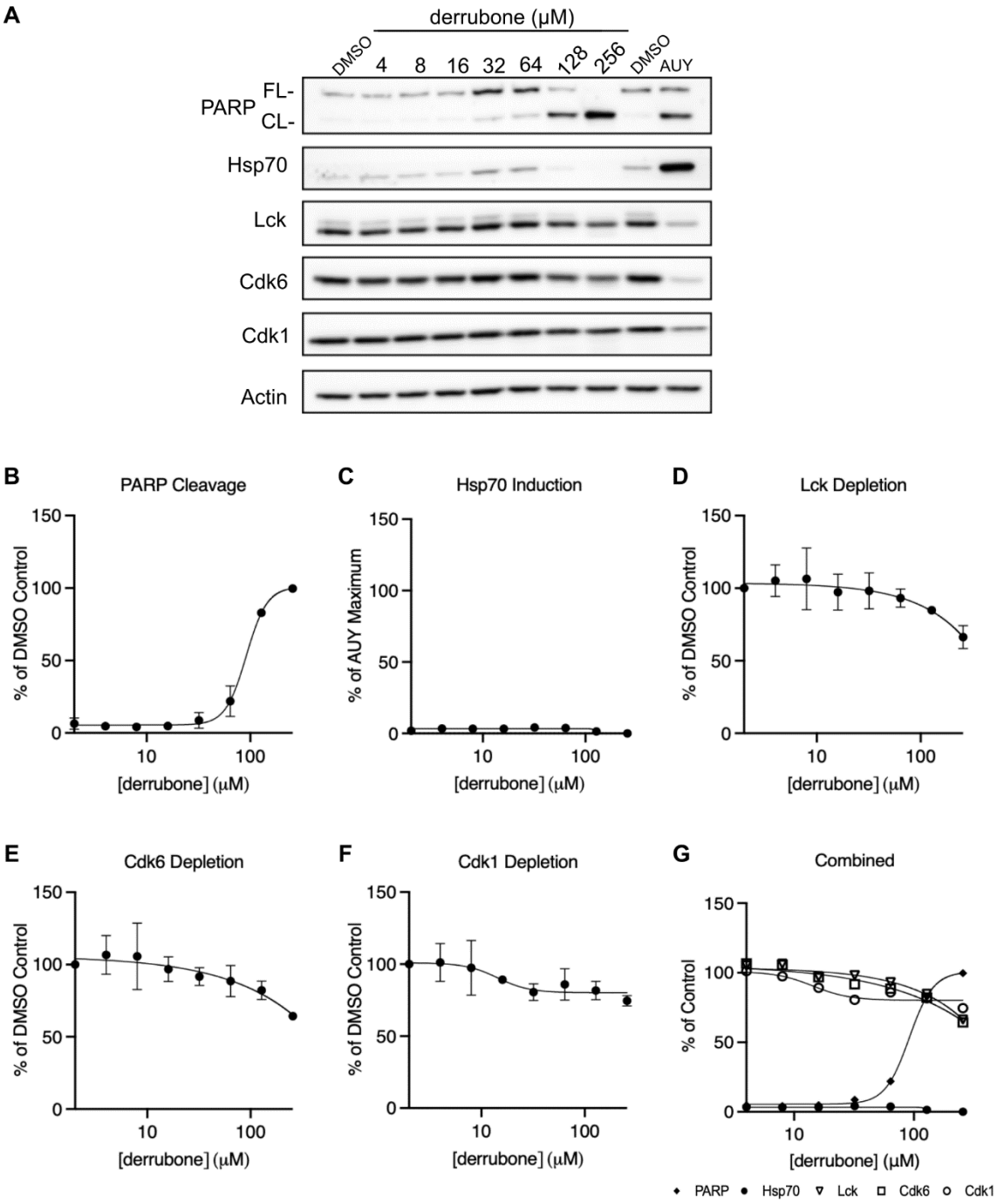

Figure 2.8. Effects of derrubone on Jurkat cells. Jurkat cells were treated with DMSO or derrubone as indicated for 24 hours as described previously in **Figure 2.2** and Methods, with DMSO and 128 nM AUY serving as negative and positive controls. Panel A: A representative Western blot. Panels B-F: Densitometries for indicated targets. Panel G: Panels B-F combined (◆ PARP-cleavage, ● Hsp70 induction, ▽ Lck depletion, □ Cdk6 depletion, ○ Cdk1 depletion).

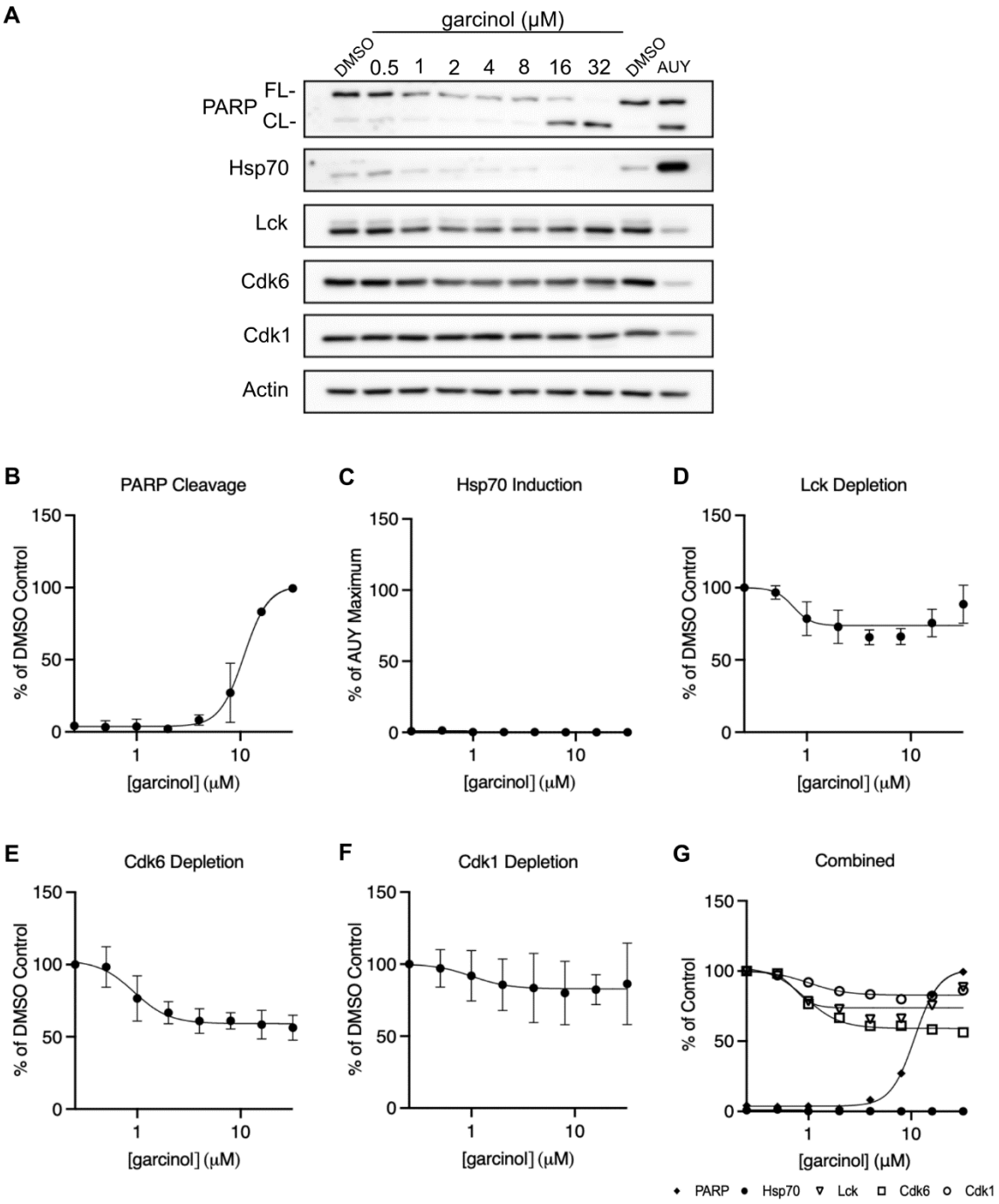

Figure 2.9. Effects of garcinol on Jurkat cells. Jurkat cells were treated with DMSO or garcinol as indicated for 24 hours as described previously in **Figure 2.2** and Methods, with DMSO and 128 nM AUY serving as negative and positive controls. Panel A: A representative Western blot. Panels B-F: Densitometries for indicated targets. Panel G: Panels B-F combined (◆ PARP-cleavage, ● Hsp70 induction, ▽ Lck depletion, □ Cdk6 depletion, ○ Cdk1 depletion).

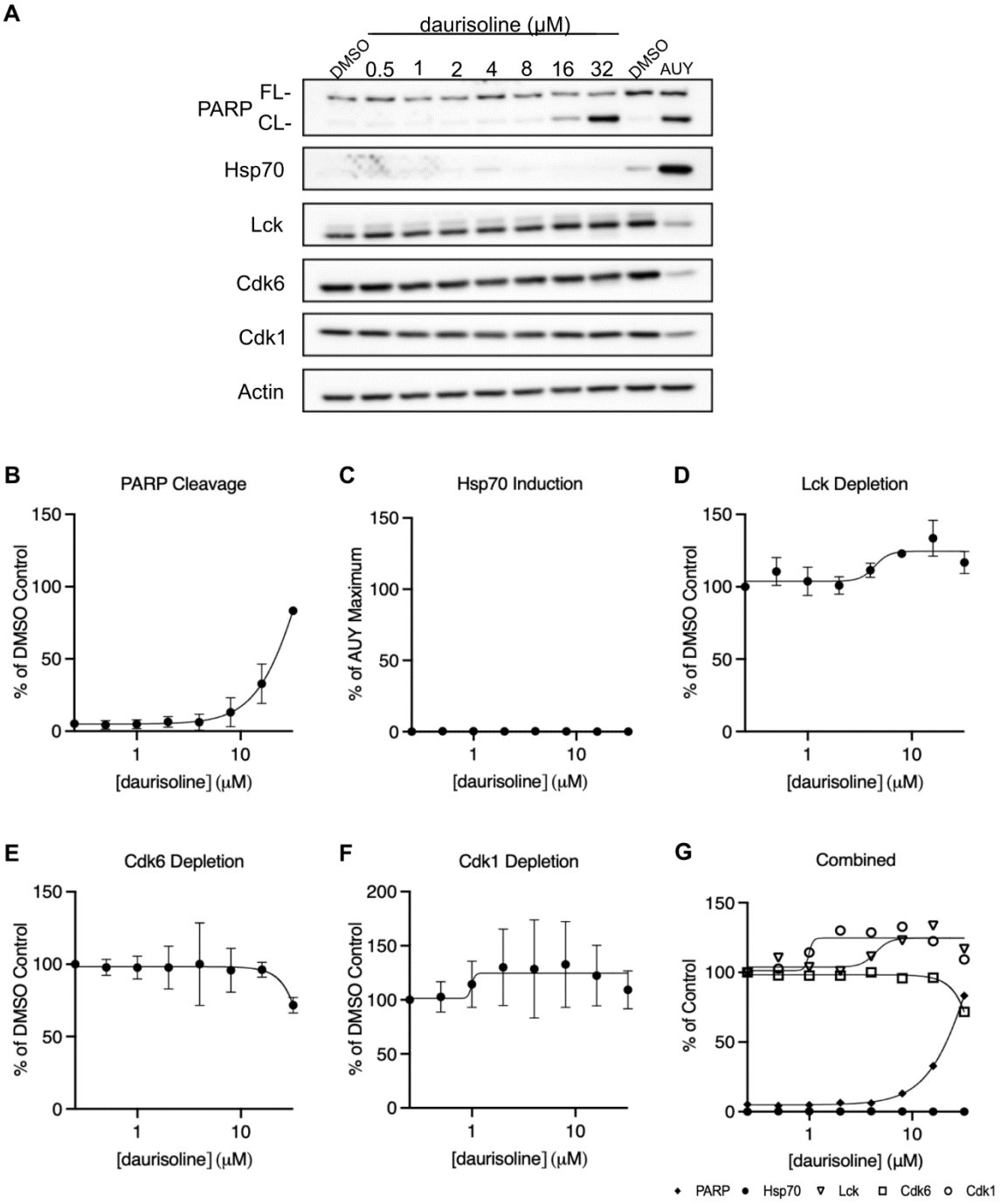

Figure 2.10. Effects of daurisoline on Jurkat cells. Jurkat cells were treated with DMSO or daurisoline as indicated for 24 hours as described previously in **Figure 2.2** and Methods, with DMSO and 128 nM AUY serving as negative and positive controls. Panel A: A representative Western blot. Panels B-F: Densitometries for indicated targets. Panel G: Panels B-F combined (◆ PARP-cleavage, ● Hsp70 induction, ▽ Lck depletion, □ Cdk6 depletion, ○ Cdk1 depletion).

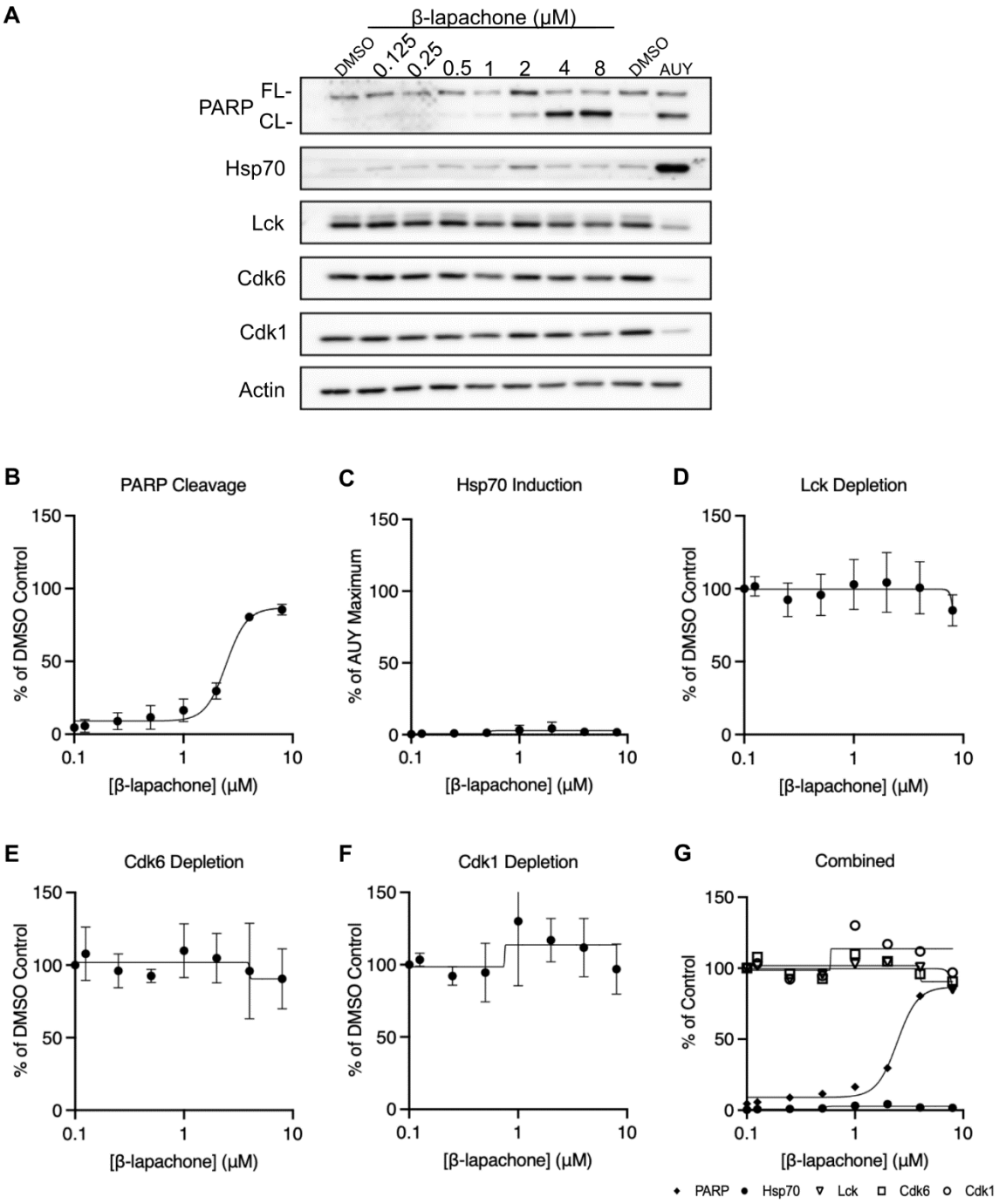

Figure 2.11. Effects of β-lapachone on Jurkat cells. Jurkat cells were treated with DMSO or β-lapachone as indicated for 24 hours as described previously in **Figure 2.2** and Methods, with DMSO and 128 nM AUY serving as negative and positive controls. Panel A: A representative Western blot. Panels B-F: Densitometries for indicated targets. Panel G: Panels B-F combined (◆ PARP-cleavage, ● Hsp70 induction, ▽ Lck depletion, □ Cdk6 depletion, ○ Cdk1 depletion).

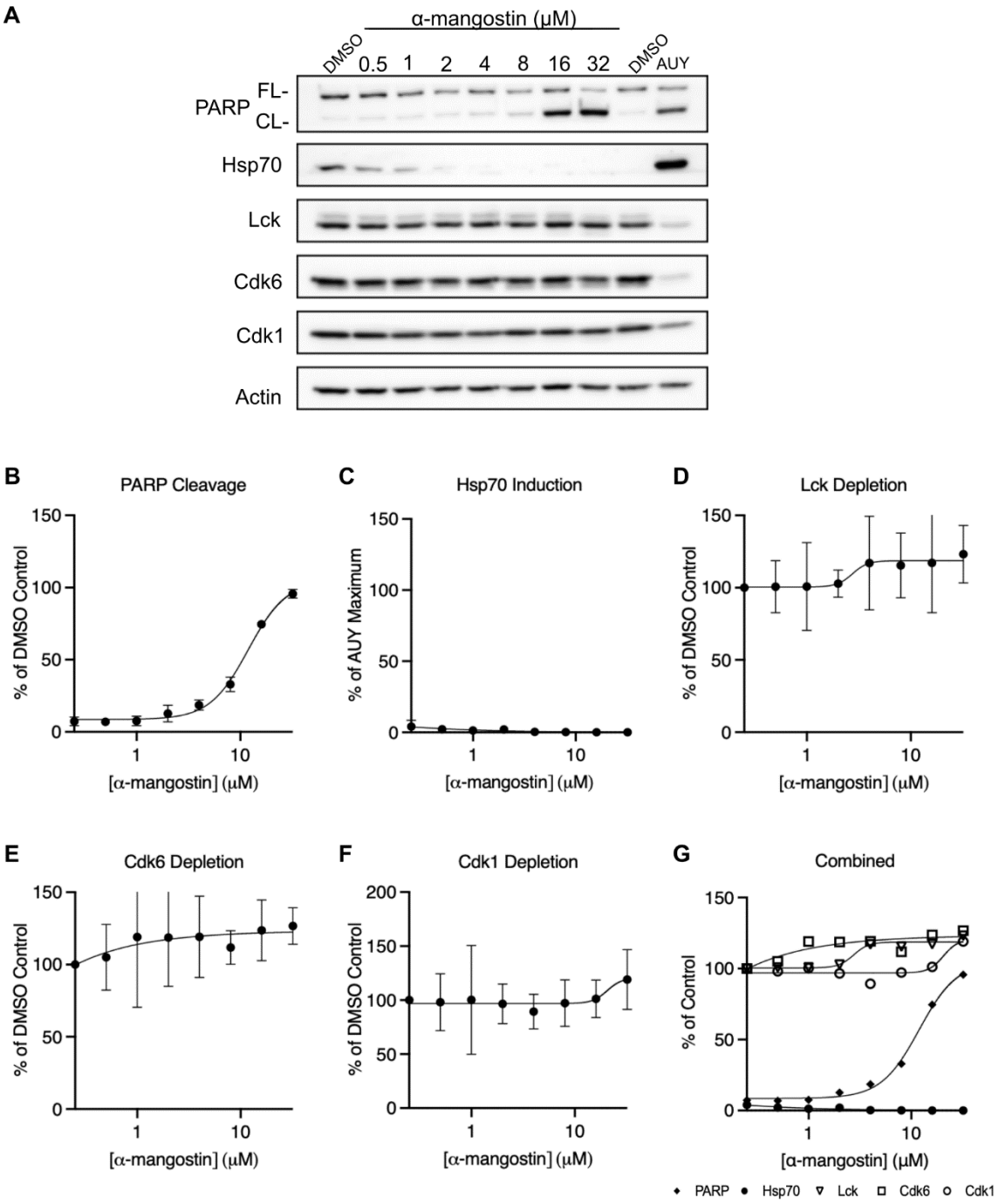

Figure 2.12. Effects of α-mangostin on Jurkat cells. Jurkat cells were treated with DMSO or α-mangostin as indicated for 24 hours as described previously in **Figure 2.2** and Methods, with DMSO and 128 nM AUY serving as negative and positive controls. Panel A: A representative Western blot. Panels B-F: Densitometries for indicated targets. Panel G: Panels B-F combined (◆ PARP-cleavage, ● Hsp70 induction, ▽ Lck depletion, □ Cdk6 depletion, ○ Cdk1 depletion).

	AUY	PTL	ATN	CSL	CLB	GBA	CMA	DUN	GRL	DRL	LAP	MAN
Lysate yield												
% DMSO +/- Standard deviation	52.8 +/- 11.2	56.2 +/- 10.7	40.2 +/- 4.1	38.5 +/- 2.3	34.5 +/- 7.0	30.4 +/- 9.2	38.2 +/- 14.1	26.2 +/- 0.2	24.6 +/- 1.8	52.6 +/- 10.9	47.5 +/- 2.6	14.0 +/- 0.6
PARP-CL												
% DMSO +/- Standard deviation	65.1 +/- 19.5	93.1 +/- 6.6	98.0 +/- 1.2	92.5 +/- 1.4	88.8 +/- 3.9	97.1 +/- 2.7	99.9 +/- 0.1	99.6 +/- 0.2	99.4 +/- 0.4	83.3 +/- 2.3	85.6 +/- 3.6	95.7 +/- 3.1
Lck												
% DMSO +/- Standard deviation	33.0 +/- 12.9	78.5 +/- 11.5	62.8 +/- 3.4	99.8 +/- 18.1	116.0 +/- 28.8	93.6 +/- 18.3	98.0 +/- 42.3	66.3 +/- 7.9	88.6 +/- 13.1	116.8 +/- 7.6	85.1 +/- 10.7	123.2 +/- 19.9
Sigmoidal depletion fit?	Yes	Yes	No	No	No	Yes	No	No	Yes	No	No	No
Cdk6												
% DMSO +/- Standard deviation	21.5 +/- 20.3	75.7 +/- 12.0	36.6 +/- 5.5	40.6 +/- 26.5	51.1 +/- 12.7	49.9 +/- 8.8	46.7 +/- 26.3	64.4 +/- 1.8	56.3 +/- 8.6	71.6 +/- 5.5	90.6 +/- 20.7	126.7 +/- 12.6
Sigmoidal depletion fit?	Yes	No	Yes	No	No	No	Yes	No	Yes	No	No	No
Cdk1												
% DMSO +/- Standard deviation	17.4 +/- 6.6	106.9 +/- 18.1	76.4 +/- 7.7	88.3 +/- 48.6	49.7 +/- 18.5	98.9 +/- 18.6	110.8 +/- 15.5	74.6 +/- 3.6	86.3 +/- 28.3	109.3 +/- 17.5	96.9 +/- 17.3	119.1 +/- 27.7
Sigmoidal depletion fit?	Yes	No	Yes	No	No	No	No	Yes	No	No	No	No

Table 2.1: Summary of compound panel effects at highest dose in series.

To choose the appropriate dose for proteomic characterization of our panel, we returned to the Western blots. Based on robust kinase depletion at 60 % PARP-cleavage in AUY922 treated cells, we chose 60 % PARP-cleavage as the appropriate dose target to characterize and compare our panel (Figure 2.1). Applying this criterion, we prepared lysates for mass spectrometry by treating cells with DMSO, or with 32 nM AUY922, 3.5 nM paclitaxel, 90 nM ailanthone, 350 nM celastrol, 30 μM clorobiocin, 150 nM gambogic acid, 5 μM coumermycin A1, 90 μM derrubone, 12.5 μM garcinol, 22.5 μM daurisoline, 3 μM β-lapachone, and 12.5 μM α-mangostin.

To validate the actual lysates used for mass spectrometry analysis, we confirmed state of apoptosis by Western blotting them for the marker PARP. As predicted, AUY922, ailanthone, clorobiocin, coumermycin A1, daurisoline, and β-lapachone induced 60 % PARP-cleavages as intended (Table 2.2). Paclitaxel, celastrol, gambogic acid, derrubone, and α-mangostin induced slightly less than cleavage than intended, while garcinol induced greater than intended PARP-cleavage (Table 2.2). Results confirmed that cells represented by each lysate were at the desired stage of apoptosis for proteomic characterization.

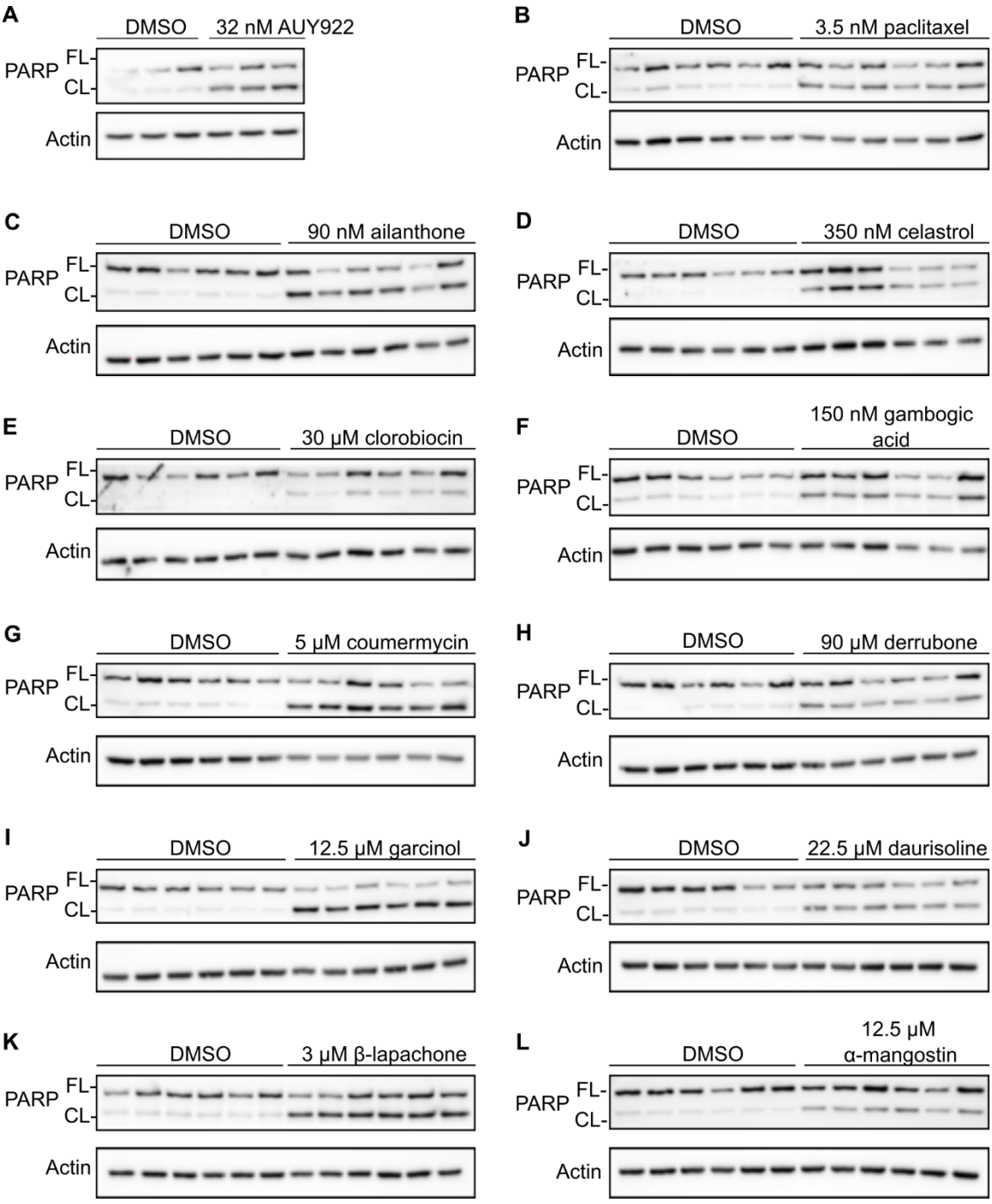

Figure 2.13. Induction of PARP-cleavage with selected drug dose for mass spectrometry. Jurkat cells were treated with either DMSO or drug for 24 hours and then lysed as previously described in Chapter 2 Methods. Western blot analysis of PARP-cleavage (FL- full length and CL- cleaved) with Actin loading control as indicated. Panel A: Three biological replicants for DMSO or AUY922 treated Jurkat lysates. Panels B-L: Six biological replicants for DMSO or drug treated Jurkat lysates as indicated, (B) paclitaxel, (C) ailanthone, (D) celastrol, (E) clorobiocin, (F) gambogic acid, (G) coumermycin A1, (H) derrubone, (I) garcinol, (J) daurisoline, (K) β-lapachone, and (L) α-mangostin.

	DMSO biological replicates PARP-cleavage							Treated biological replicates PARP-cleavage						
	1	2	3	4	5	6	Average	1	2	3	4	5	6	Average
AUY922	27.8	23.1	12.4				21.1	67.7	51.7	67.1				62.2
paclitaxel	19.8	16.3	18.9	11.2	12.6	7.1	14.3	42.0	47.5	45.3	54.6	53.5	41.0	47.3
ailanthone	8.7	8.8	10.1	10.0	6.6	6.1	8.4	57.5	71.4	64.9	63.4	67.4	49.1	62.3
celastrol	7.6	0.9	1.1	1.5	1.6	0.9	2.3	26.9	37.3	44.9	65.1	49.2	52.3	46.0
clorobiocin	10.1	15.9	13.3	5.8	7.7	4.7	9.6	65.7	33.8	49.9	46.0	57.6	53.4	51.1
gambogic acid	13.4	13.8	16.1	14.2	15.4	15.2	14.7	35.6	35.9	34.4	47.1	50.9	34.7	39.8
coumermycin A1	13.7	8.4	11.0	14.9	6.3	1.3	9.3	66.5	67.9	54.0	52.7	72.9	70.2	64.0
derrubone	0.1	0.0	10.4	8.5	14.5	7.0	6.8	45.7	31.8	48.8	41.8	38.0	34.0	40.0
garcinol	5.4	10.7	6.9	12.1	8.8	9.6	8.9	82.4	83.7	76.1	84.2	85.5	80.9	82.1
daurisoline	8.2	9.1	7.5	8.5	12.5	10.9	9.5	49.1	40.6	52.5	64.0	62.8	48.1	52.9
β-lapachone	16.8	12.8	15.9	12.4	14.1	14.7	14.5	64.6	65.6	54.9	57.4	50.1	58.6	58.5
α-mangostin	9.3	5.9	7.4	4.1	5.0	2.7	5.7	25.2	20.7	17.3	36.8	36.1	23.4	26.6

Table 2.2 PARP-cleavage of mass spectrometry samples.

To validate the robustness of our mass spectrometry and proteomics pipeline, we analyzed the number of proteins identified among the biological replicates. Results showed that approximately 6000 proteins common to all of the biological replicates for our compound panel (Table 2.3). Table 2.4 reports the number of proteins with quantifiable ratios of (treated/control) and the number of significant changes in each individual experiment. Results confirmed that we collected highly robust data capable of characterizing proteomic changes induced by our panel.

Volcano plots were used to visualize the changes in protein expression (Figure 2.14). Different compounds induced different degrees of differential protein expression. Paclitaxel, derrubone, and α-mangostin induced minor proteomic perturbations (< 5 % proteome significantly changed) (Table 2.4). AUY922, ailanthone, celastrol, clorobiocin, gambogic acid, coumermycin A1, garcinol, daurisoline, and β-lapachone all induced larger proteomic perturbations (> 5 % proteome significantly changed) (Table 2.4).

To validate our perturbation fingerprint of Hsp90 inhibition, seen in our Jurkat cells, we compared this fingerprint between our 32 nM AUY922 sample to those previously published for 75 nM AUY922[‡], 150 nM 17-DMAG[‡], and 1 μM geldanamycin[†] ([‡][105], [†][106]). Our AUY922 induced changes were highly correlated to previous AUY922 (Pearson correlation coefficient, *r*, of 0.71), and similarly to the previously published 17-DMAG (*r* = 0.70) (Table 2.5). Moreover, AUY922 and geldanamycin (*r* = 0.63), despite changes in labs and methods (Table 2.5). Therefore, we concluded that we could compare the proteomic fingerprints of our novel compound panel to those of our N-terminal Hsp90 inhibitor AUY922 to identify and quantify conserved mechanisms of action.

Proteins identified in n, samples	AUY	PTL	ATN	CSL	CLB	GBA	CMA	DUN	GRL	DRL	LAP	MAN
1	2	0	2	5	3	2	0	3	1	3	2	3
2	0	3	4	6	2	6	1	1	1	2	1	1
3	0	1	1	8	3	2	2	1	3	3	5	0
4	1	3	2	9	0	3	2	3	1	3	2	1
5	8	6	8	23	5	7	5	5	6	8	6	8
6	6022	589	608	692	678	803	630	756	613	708	739	629
7		4	2	8	2	4	0	3	5	3	2	1
8		1	4	9	4	3	2	0	1	3	3	2
9		4	4	11	1	3	3	1	2	2	4	1
10		3	4	13	5	1	9	1	1	10	2	3
11		9	12	9	7	9	12	7	7	9	4	7
12		6484	6390	5954	6301	6021	6493	6249	6488	6315	6251	6486

Table 2.3 Summary of number of proteins identified in n, number of mass spectrometry samples (control and treated).

	Number of log2(treated/control) proteins with valid values	Number of proteins significantly changed	% of proteins significantly changed	Number of proteins significantly up-regulated	Number of proteins significantly down-regulated	Ratio of proteins significantly regulated (up:down)
AUY922	6031	792	13.1	247	545	1:2.2
paclitaxel	7106	12	0.2	6	6	1:1
ailanthone	7039	655	9.3	155	500	1:3.2
celastrol	6739	379	5.6	188	191	1:1
clorobiocin	7005	384	5.5	123	261	1:2.1
gambogic acid	6860	285	4.2	169	116	1.5:1
coumermycin A1	7159	589	8.2	114	475	1:4.2
derrubone	7026	78	1.1	39	39	1:1
garcinol	7128	532	7.5	195	337	1:1.7
daurisoline	7065	516	7.3	336	180	1.9:1
β-lapachone	7019	484	6.9	132	352	1:2.7
α-mangostin	7139	169	2.4	52	117	1:2.3

Table 2.4 Summary of the effects of compound treatment on global protein expression.

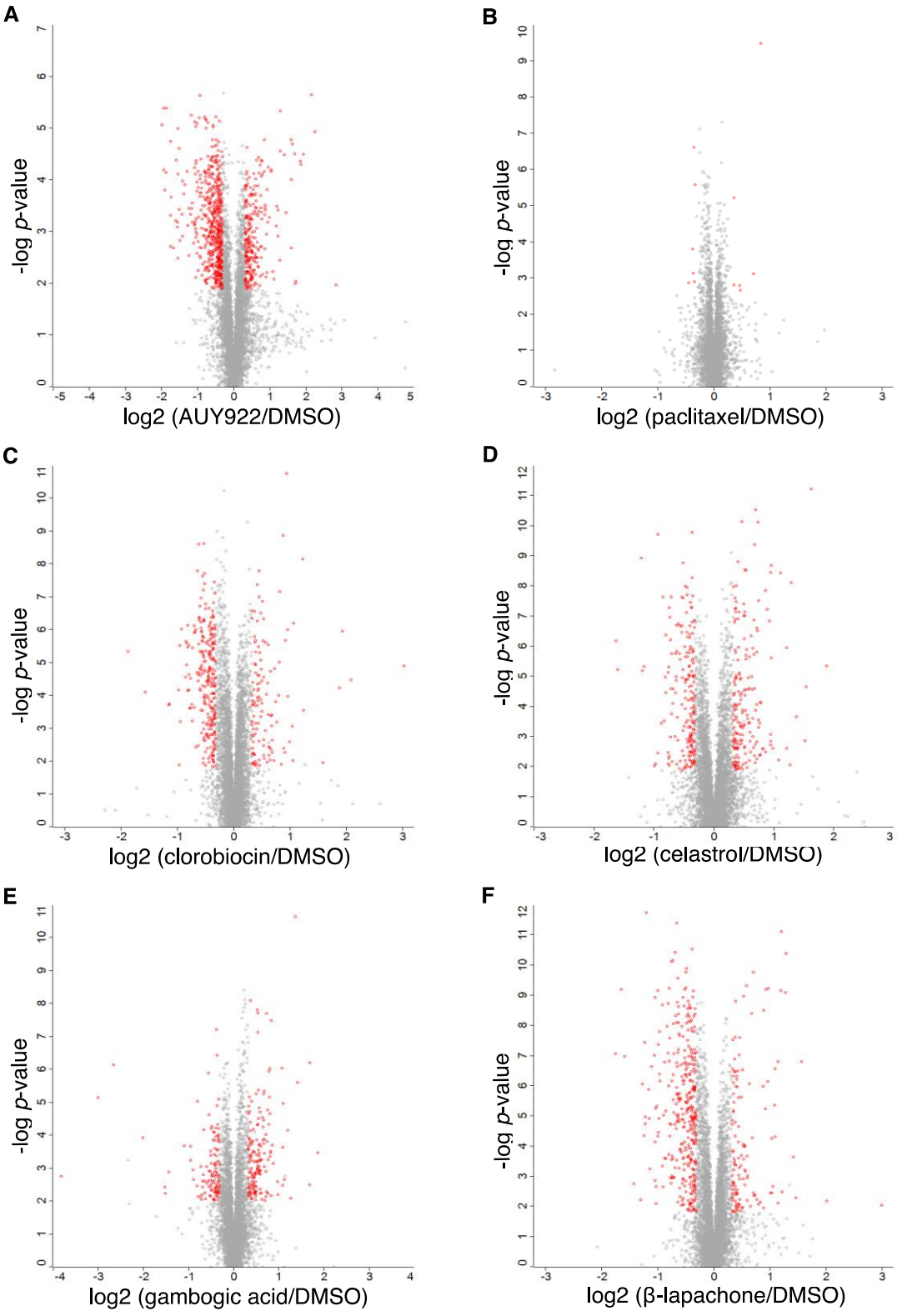

Figure 2.14. Effects of drug treatment on global protein expression. To visualize the relative contributions of fold-change to *p*-value thresholds induced by drug treatment, these values were graphed against each other ("volcano plots"). Panels A-F: volcano plots of indicated drug treatment. Red points indicate significantly changed proteins by Benjamini-Hochberg testing, FDR 0.05, with log2 fold changes greater that 25 %.

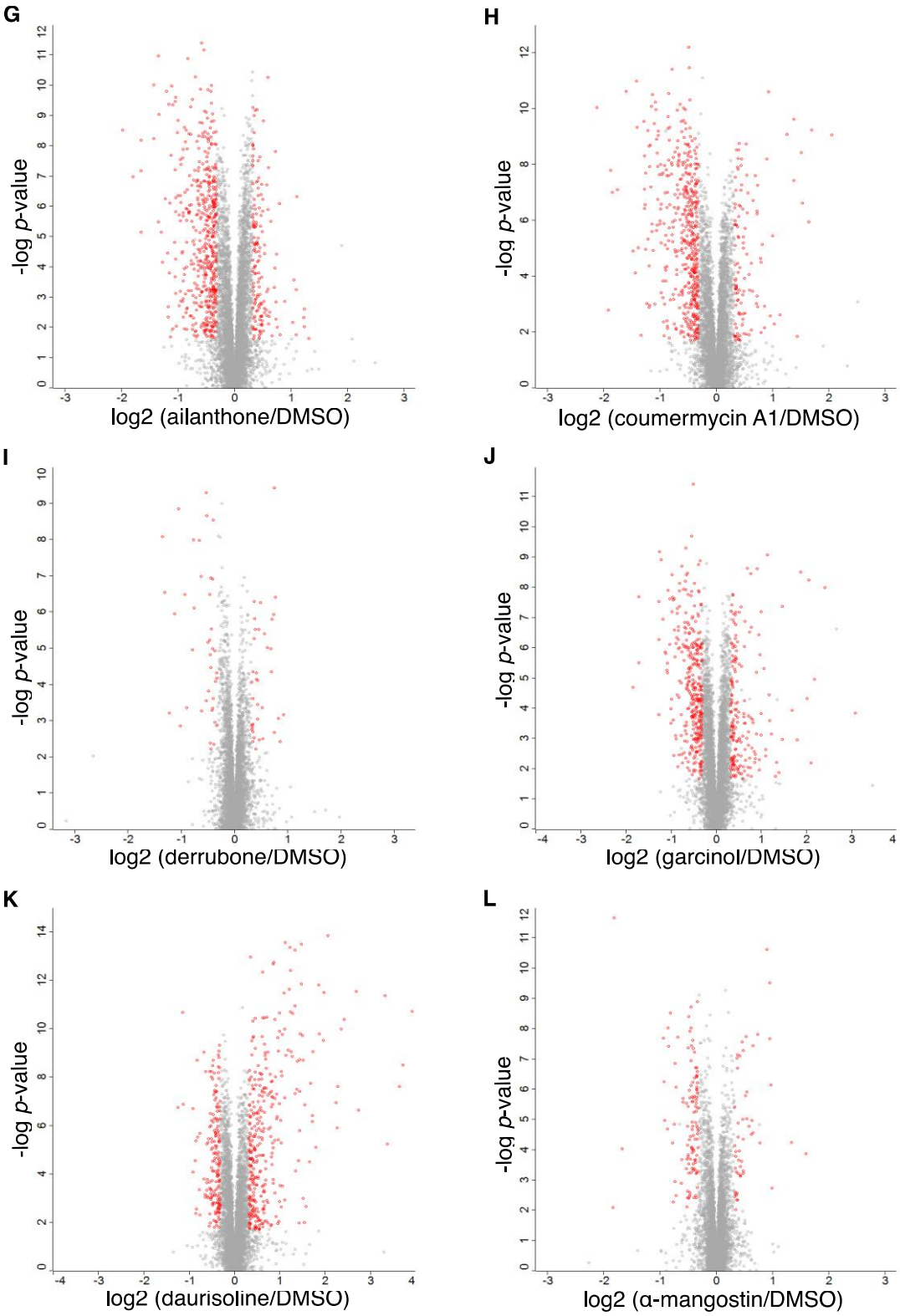

Figure 2.14 (continued). Effects of drug treatment on global protein expression.
Panels G-L: volcano plots of indicated drug treatment. Red points indicate significantly changed proteins by Benjamini-Hochberg testing, FDR 0.05, with log2 fold changes greater that 25 %.

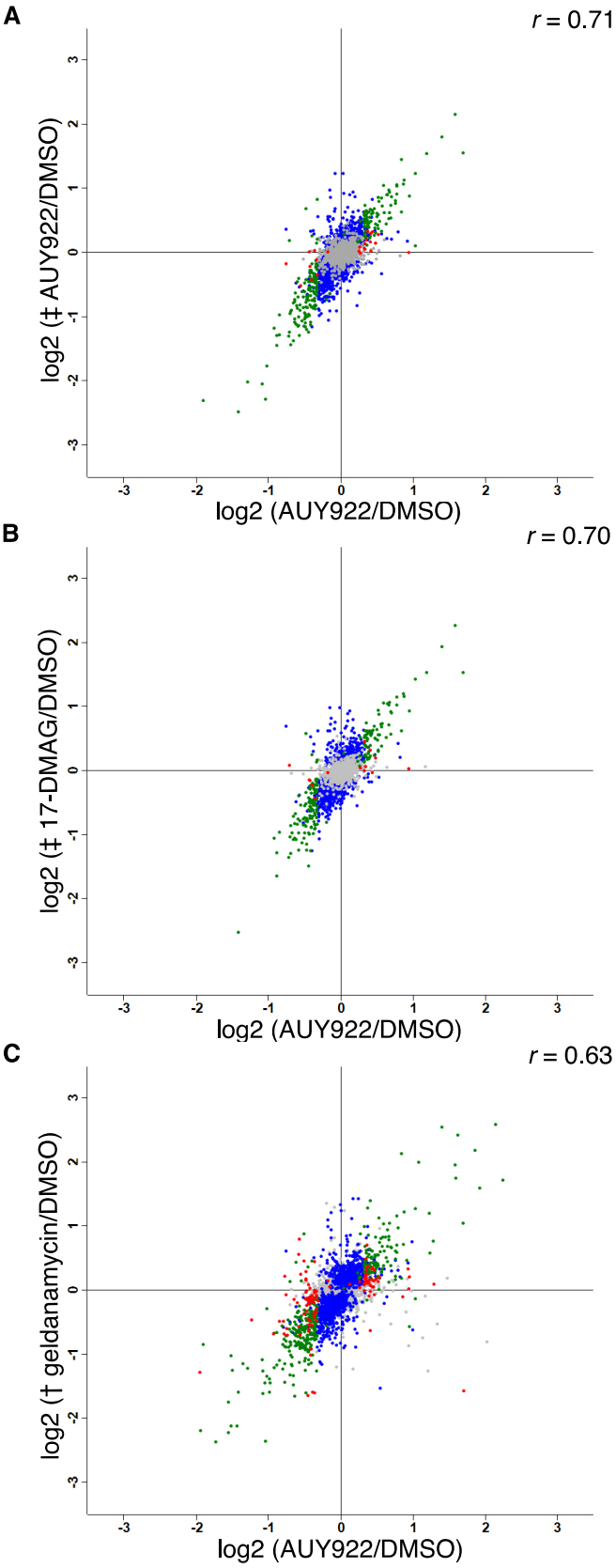

Figure 2.15. Pairwise comparison of changes in global protein expression induced by N-terminal Hsp90 inhibitors. To visualize the conserved changes in global protein expression induced by N-terminal Hsp90 inhibitors the log2 (treated/DMSO) for AUY922 was graphed against previously published N-terminal Hsp90 inhibitor datasets. Red dots indicate proteins significantly changed by AUY922 in this study. Blue dots indicate proteins significantly changed by previously published N-terminal inhibitor. Panel A: AUY922. Panel B: 17-DMAG. Panel C: geldanamycin. Green dots indicate proteins significantly changed in both. Pearson correlation (*r*) between the datasets is located in the top right of the panel.

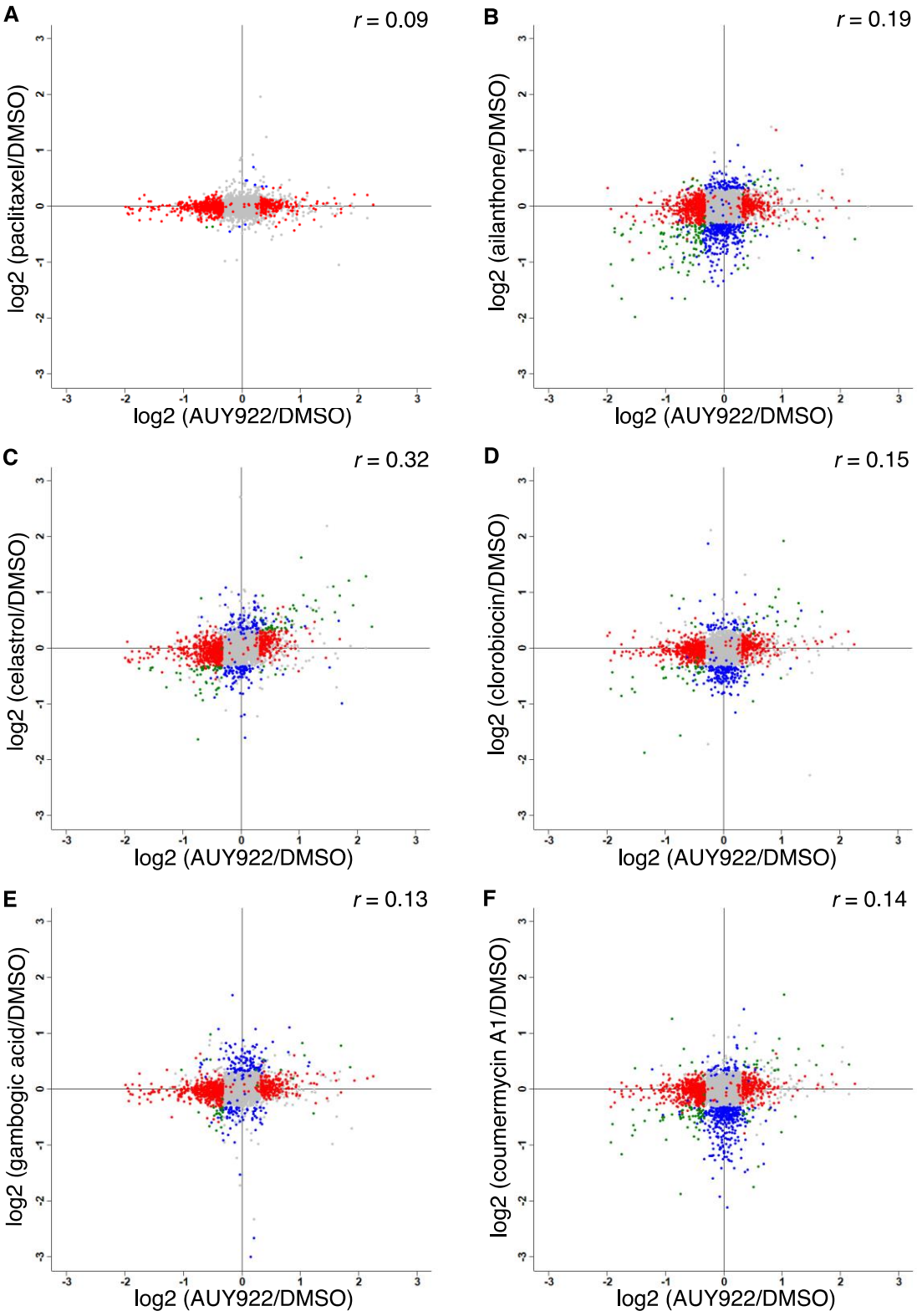

Figure 2.16. Pairwise comparison of changes in global protein expression induced by compound treatment.

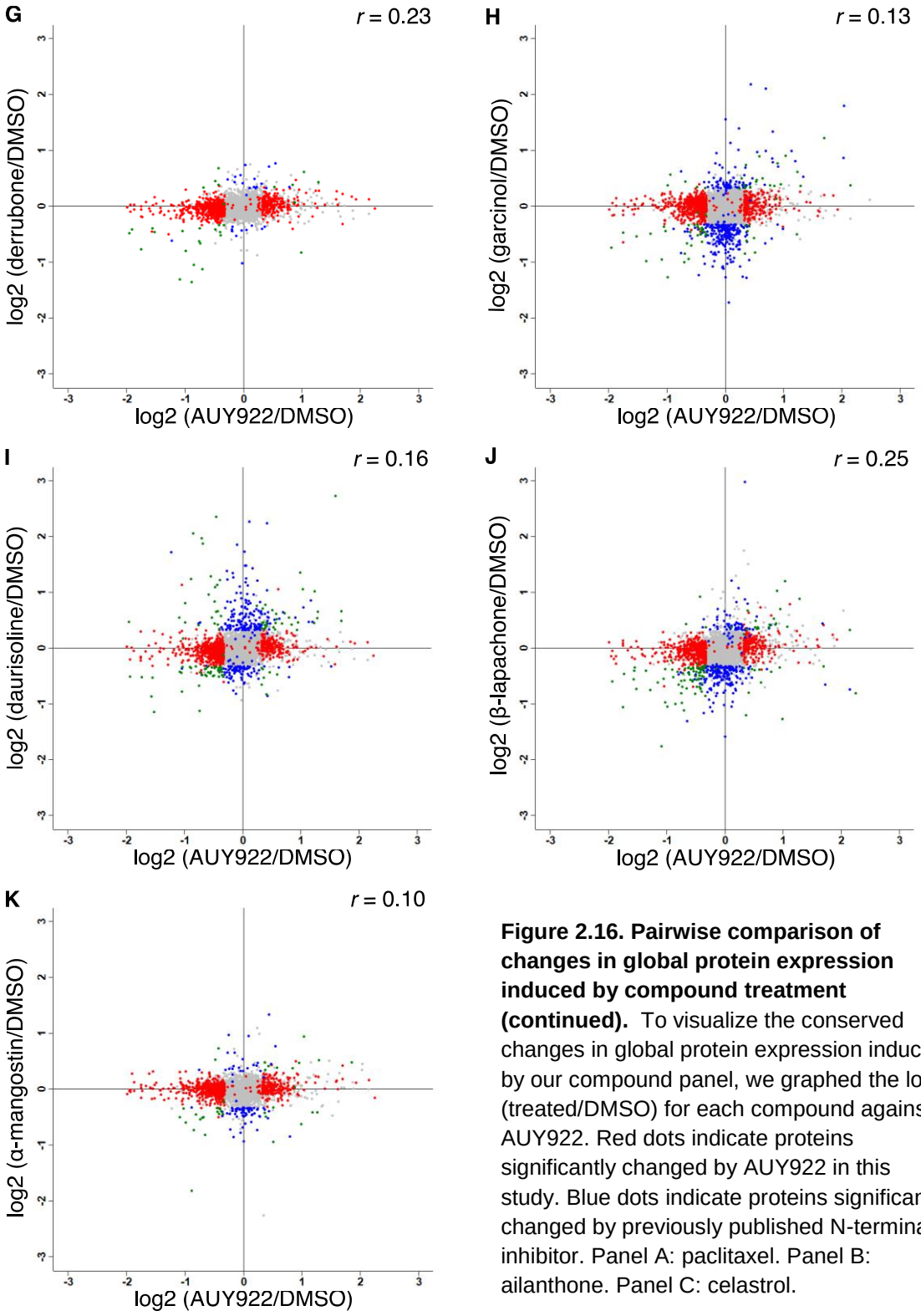

Figure 2.16. Pairwise comparison of changes in global protein expression induced by compound treatment (continued). To visualize the conserved changes in global protein expression induced by our compound panel, we graphed the log2 (treated/DMSO) for each compound against AUY922. Red dots indicate proteins significantly changed by AUY922 in this study. Blue dots indicate proteins significantly changed by previously published N-terminal inhibitor. Panel A: paclitaxel. Panel B: ailanthone. Panel C: celastrol. Panel D: clorobiocin. Panel E: gambogic acid. Panel F: coumermycin A1. Panel G: derrubone. Panel H: garcinol. Panel I: daurisoline. Panel J: β-lapachone. Panel K: α-mangostin. Green dots indicate proteins significantly changed in both. Pearson correlation (*r*) between the datasets is located in the top right of the panel.

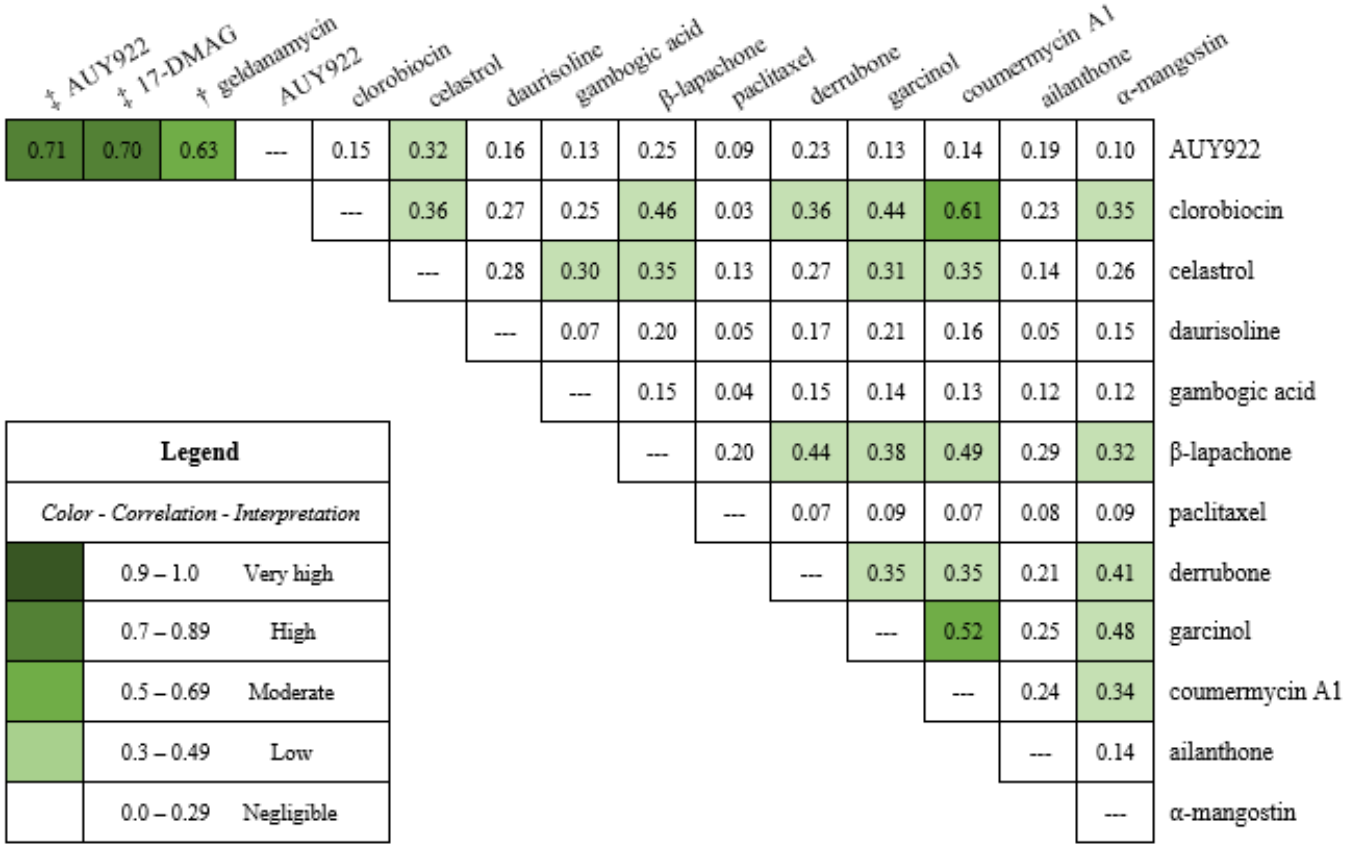

Table 2.5. Pearson correlations, *r*, of compound treatments.

After comparing the proteomic fingerprints of our novel compound panel, celastrol demonstrated a low correlation to AUY922 (r = 0.32). The other 10 compounds in our panel induced negligible correlations (r = 0.0-0.29) to AUY922 (Table 2.5). These data came as a surprise considering that the proposed hypothesis is the only difference between N- and C-terminal Hsp90 inhibition models is the lack of an induction of the heat shock response.

Next, we wanted to compare the proteomic fingerprints between our putative C-terminal compounds. We hypothesized that if these compounds were in fact all C-terminal Hsp90 inhibitors, they should have conserved proteomic fingerprints. Daurisoline had negligible correlations (r = 0.0-0.29) to our drug panel (Table 2.5). This result suggests that daurisoline is not any form of Hsp90 inhibitor and induces cell death by an unique method which is different to any of the other compounds in our panel. Coumermycin A1 was the only putative compound to have multiple moderate correlations, clorobiocin (r = 0.61), and garcinol (r = 0.52) (Table 2.5). The other 6 compounds in our panel had negligible (r = 0.0-0.29) or low correlations (r = 0.3-0.49) with the rest of the panel (Table 2.5). These results suggest that not all of our putative C-terminal inhibitors are inducing cell death through the same mechanism.

To characterize the extent of which these compounds are mechanistically related we conducted bootstrapped hierarchical clustering on the total proteomic perturbances induced by each treatment. Nodes 1, 2, 4, and 6 were determined to be statistically significant (p-value > 0.95) in our dendrogram (Figure 2.17). The node 1 (clorobiocin and coumermycin A1) comes as little surprise as they're structurally similar compounds and had the highest correlation of the putative compounds in our table (r = 0.61) (Table 2.5).

Node 2 (garcinol and α-mangostin) do not have the same scaffold structure, but do both contain multiple isoprenyl groups, and have one of the higher correlations for our panel (r = 0.48) (Figure 2.17, Table 2.5). Similarly, node 4 (celastrol and gambogic acid) are structurally different compounds that significantly clustered despite the low correlation between the compounds (r = 0.30). Both compounds do contain non-specific, cysteine-reactive chemistry in the form of Michael additions [108, 109]. This node in particular is interesting because celastrol has higher correlations with five of the other compounds in the panel, but this motif has been shown to be critical in the anti-proliferative effects of both of these compounds. This result suggests the strength of bootstrap hierarchical clustering technique to not just cluster based on the strength of the correlation between two compounds, but to potentially elucidate conserved mechanisms. The significant super cluster located at node 6 suggests that clorobiocin, coumermycin A1, β-lapachone, derrubone, garcinol, and α-mangostin have a common mechanism or over-arching phenotype (Figure 2.17).

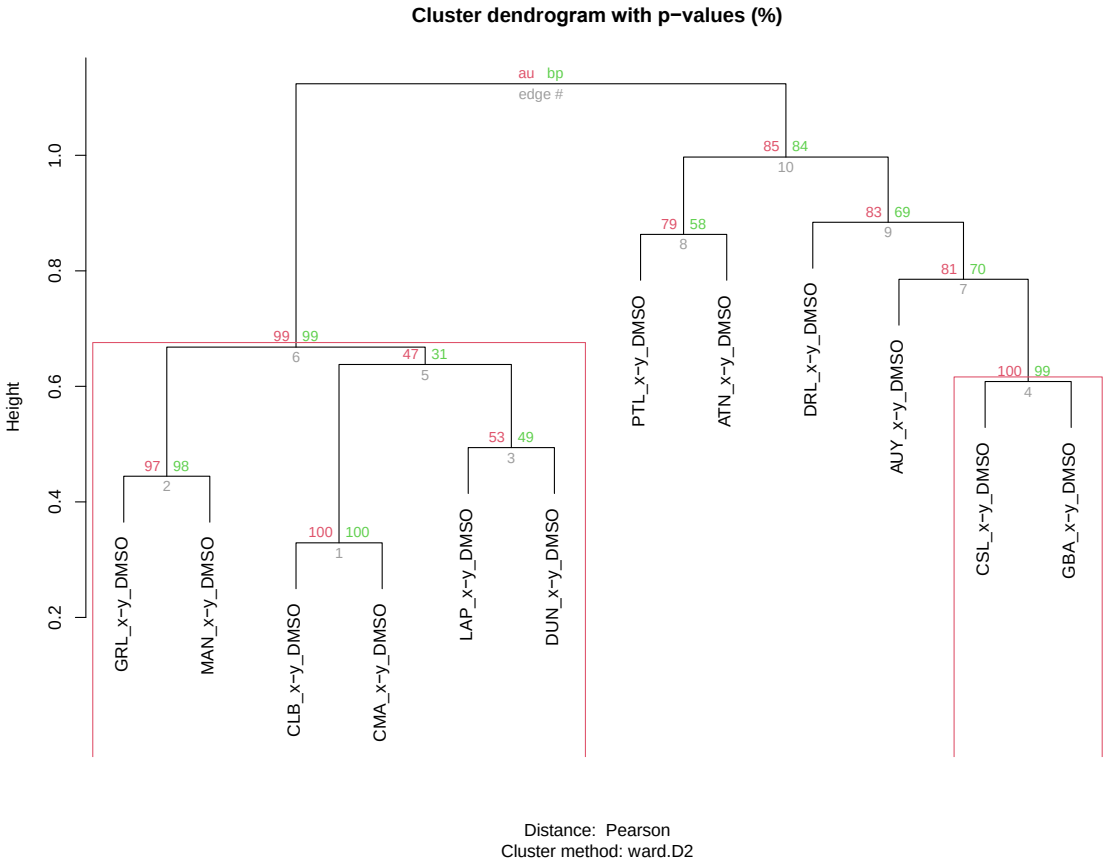

Figure 2.17. Hierarchical clustering of compound panel. Hierarchical clustering was completed on 5,796 genes quantified in all data sets. Dendrogram was created using the Pvclust R package as described in Methods. Clustering was completed using ward.D2 and Pearson correlation for distance measurement. Data were bootstrap resampled for n=1,000. Approximately unbiased (AU), and boostrap probability (BP) *p*-values are present at each node of the branch. Clusters with AU p-values greater than 95% are highlighted by red rectangles, and indicate clusters supported by data.

To expand on the observations made above we increased the number of compounds used to generate the dendrogram by adding samples previously generated by our lab group and from literature [105, 106, 110]. The dendrogram generated is highly consistent with the one generated by Kline. Our AUY922 significantly clustered with the three other N-terminal Hsp90 inhibitors node 7 (Figure 2.18). Additionally, daurisoline significantly clustered with structurally similar compounds berbamine and cepharantine (Figure 2.18 node 21). Surprisingly, it appears the dendrogram is dominated by lysis technique with node 27 being the urea lysates generated in this study, and nodes 29 and 30 being comprised of RIPA samples (exception being AUY922 and daurisoline) previously published (Figure 2.18). These results suggest that hierarchical clustering is a method capable of elucidating conserved mechanism between compounds. However, the lack of control compounds (mechanisms other than proteostasis perturbation) in our datasets prevents us from concluding mechanisms for our putative inhibitors. Attempts to add control compounds from other cell lines lead to clusters driven by cell line differences, therefore we discontinued that approach (data not shown).

The whole-proteome comparisons above lacked the precision needed to address specific Hsp90 regulated protein groups, namely Hsp90 dependent kinases, Hsp90 interacting proteins, and the Hsf1-regulated cassette. Therefore, we extracted from our larger data sets, just those data for these probes of Hsp90 chaperone function and used these subsets of the data to generate heatmaps. None of the compounds in our panel generated heatmaps that resembled AUY922 (Figures 2.19-2.29). Therefore, we concluded that none of the putative compounds in our panel demonstrated the hallmarks of Hsp90 inhibition in Jurkat cells.

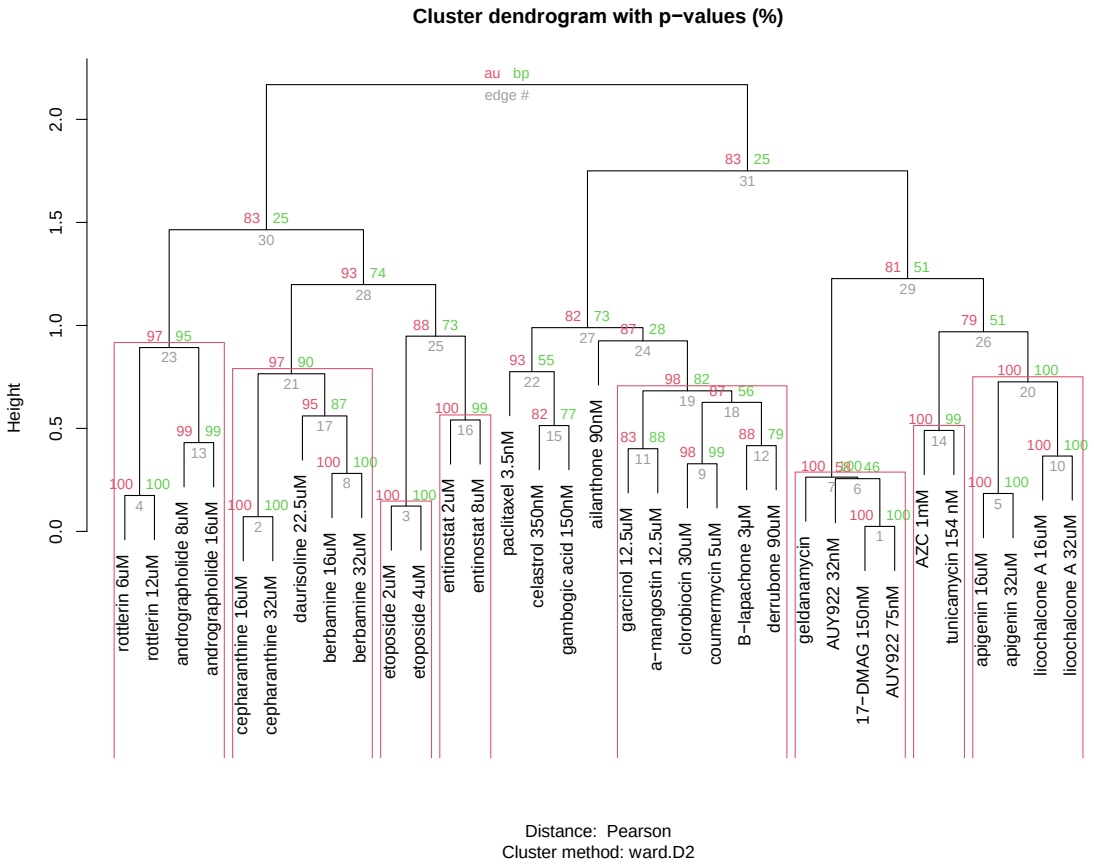

Figure 2.18. Hierarchical clustering of expanded compound panel. Hierarchical clustering was completed on 8,571 genes. Data includes compounds characterized in this study along with Kline, Voruganti, and Fierro-Monti *et al*. Dendrogram was created using the Pvclust R package as described in Methods. Clustering was completed using ward.D2 and Pearson correlation for distance measurement. Data were bootstrap resampled for n=1,000. Approximately unbiased (AU), and boostrap probability (BP) *p*-values are present at each node of the branch. Clusters with AU p-values greater than 95% are highlighted by red rectangles, and indicate clusters supported by data.

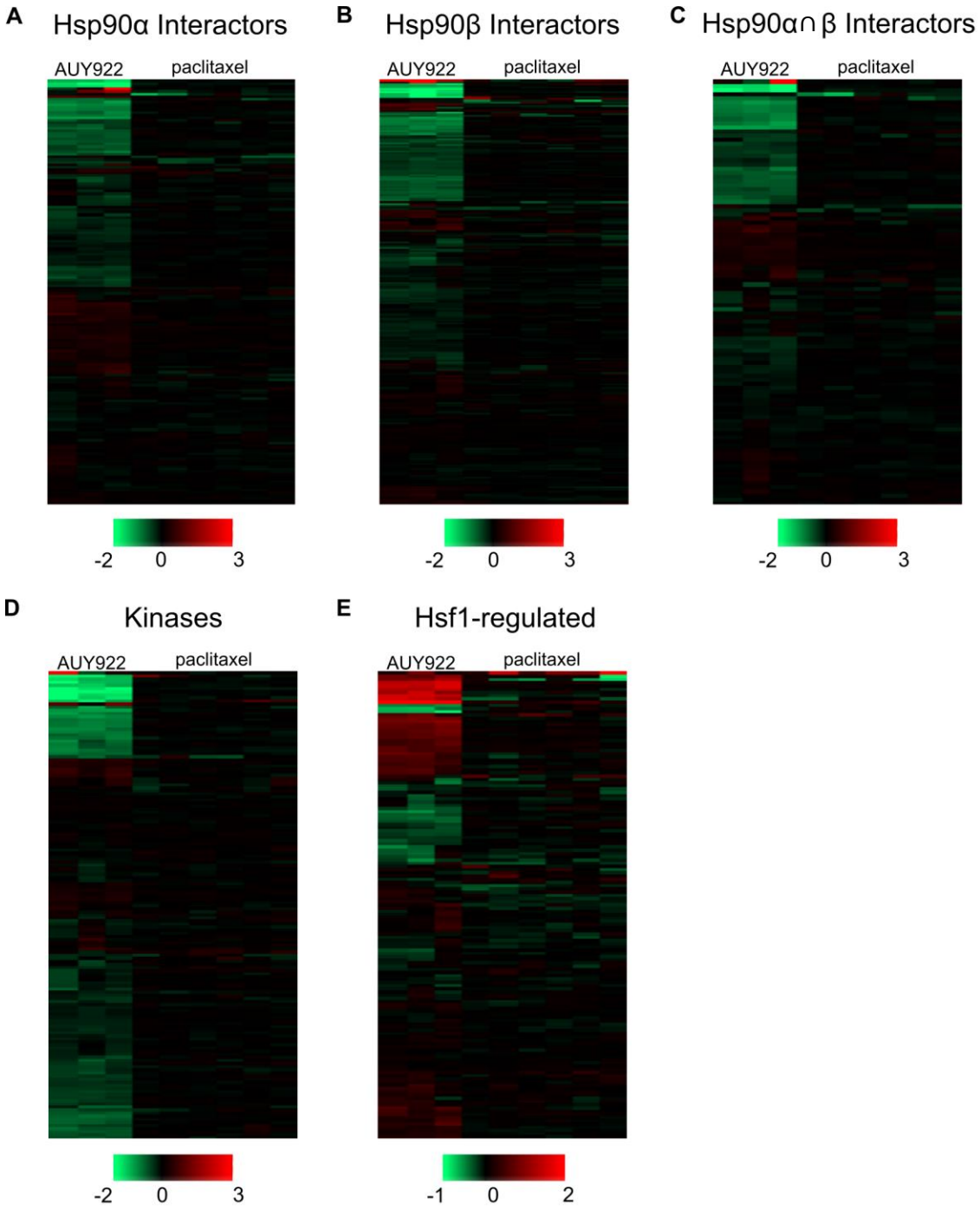

Figure 2.19. Comparison of AUY922 and paclitaxel changes on protein expression of Hsp90 inhibition probes. Protein expression was analyzed as described in Methods, and heat maps representing changes in protein expression were constructed for the Hsp90 inhibition probes. The numbers in the color keys located at the bottom of each panel are the log2(treated/control) for each biological experiment (n=3 for AUY922, n=6 for paclitaxel). Panel A: Hsp90α interactors. Panel B: Hsp90β interactors. Panel C: Intersect (∩) of Hsp90α and Hsp90β interactors. Panel D: Kinases. Panel E: Hsf1-regulated proteins.

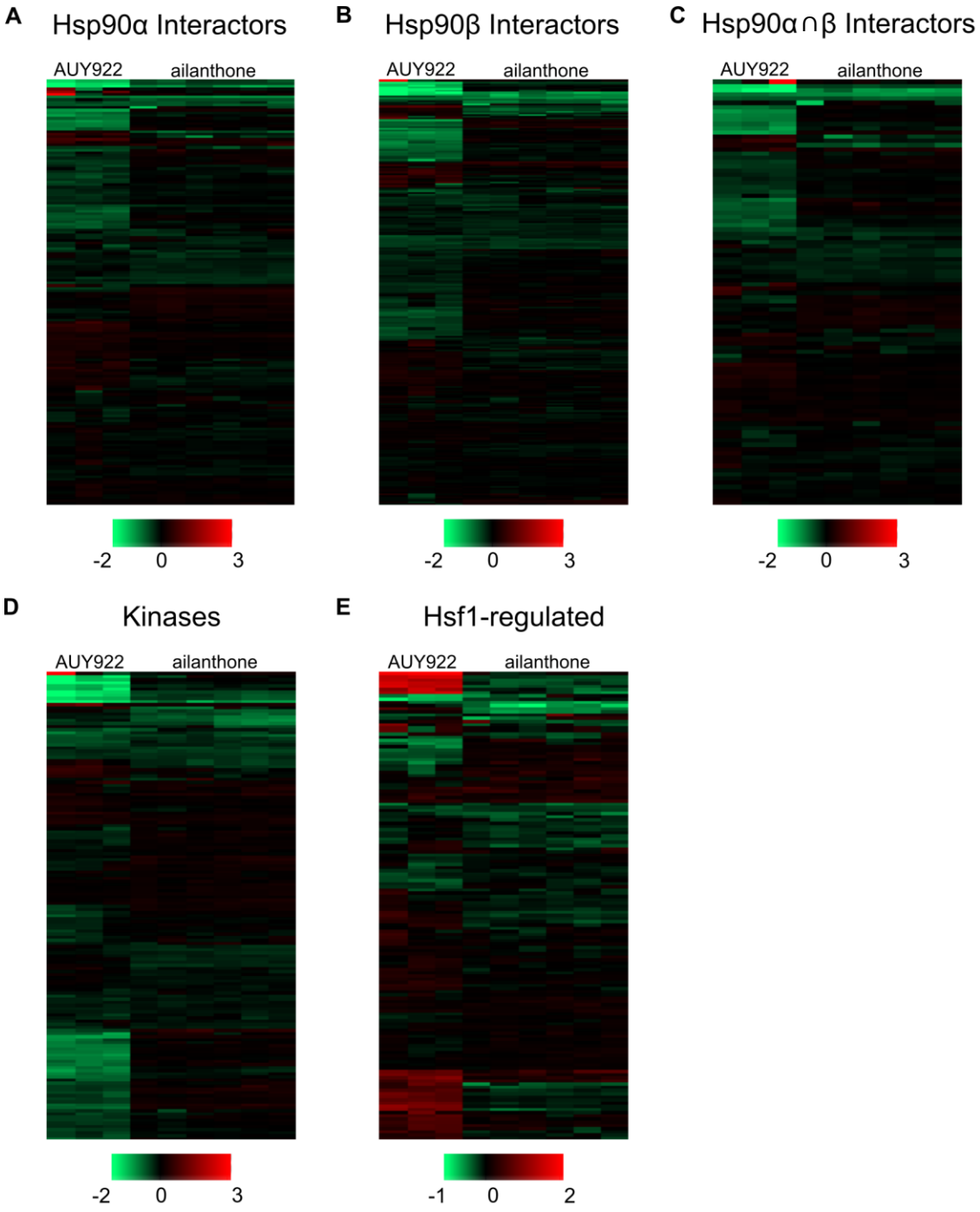

Figure 2.20. Comparison of AUY922 and ailanthone changes on protein expression of Hsp90 inhibition probes. Heatmaps of protein expression changes were made as previously described in **Figure 2.19**. The numbers in the color keys located at the bottom of each panel are the log2(treated/control) for each biological experiment (n=3 for AUY922, n=6 for ailanthone). Panel A: Hsp90α interactors. Panel B: Hsp90β interactors. Panel C: Intersect (∩) of Hsp90α and Hsp90β interactors. Panel C: Hsp90 dependent. Panel E: Kinases. Panel F: Hsf1-regulated.

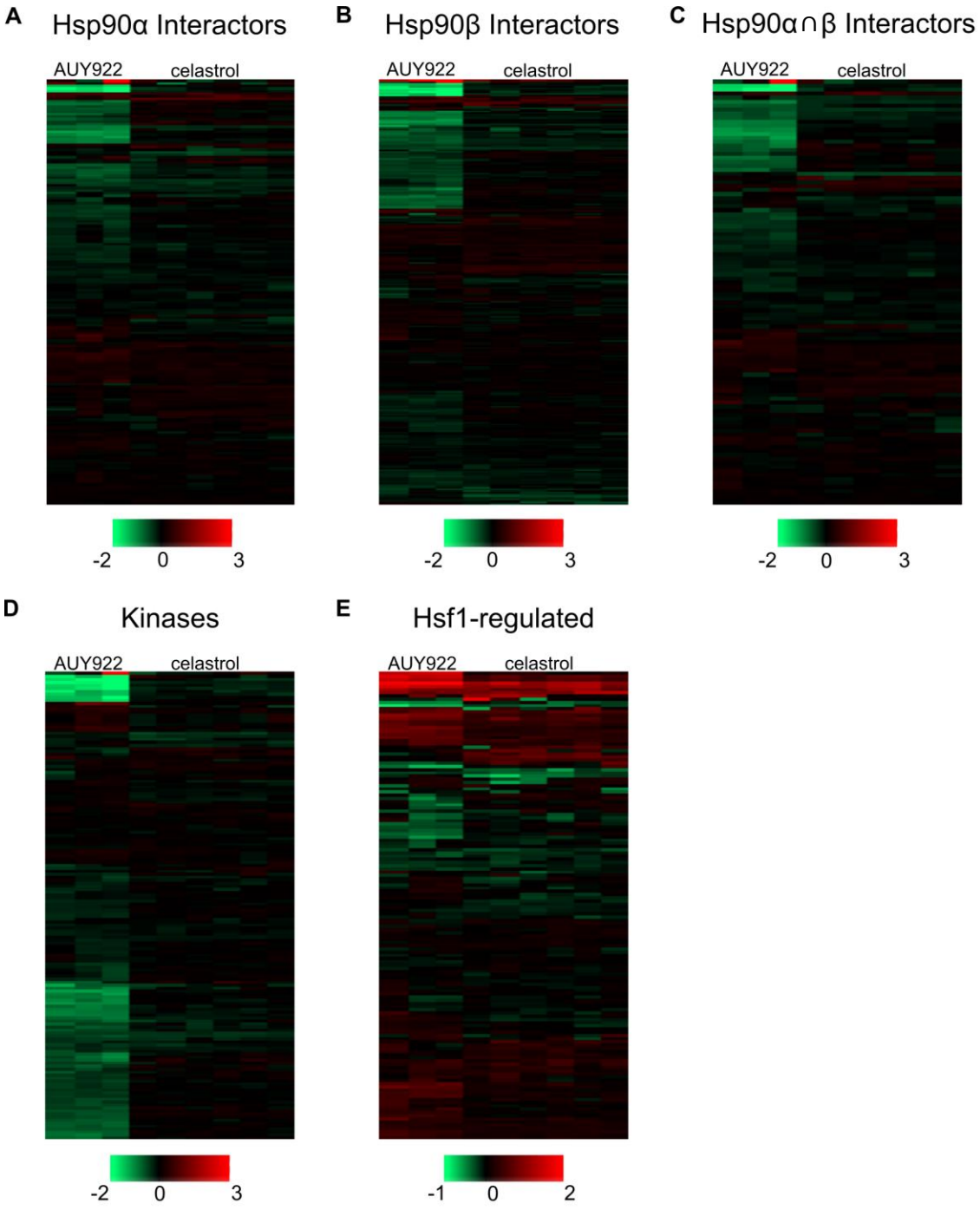

Figure 2.21. Comparison of AUY922 and celastrol changes on protein expression of Hsp90 inhibition probes. Heatmaps of protein expression changes were made as previously described in **Figure 2.19**. The numbers in the color keys located at the bottom of each panel are the log2(treated/control) for each biological experiment (n=3 for AUY922, n=6 for celastrol). Panel A: Hsp90α interactors. Panel B: Hsp90β interactors. Panel C: Intersect (∩) of Hsp90α and Hsp90β interactors. Panel C: Hsp90 dependent. Panel E: Kinases. Panel F: Hsf1-regulated.

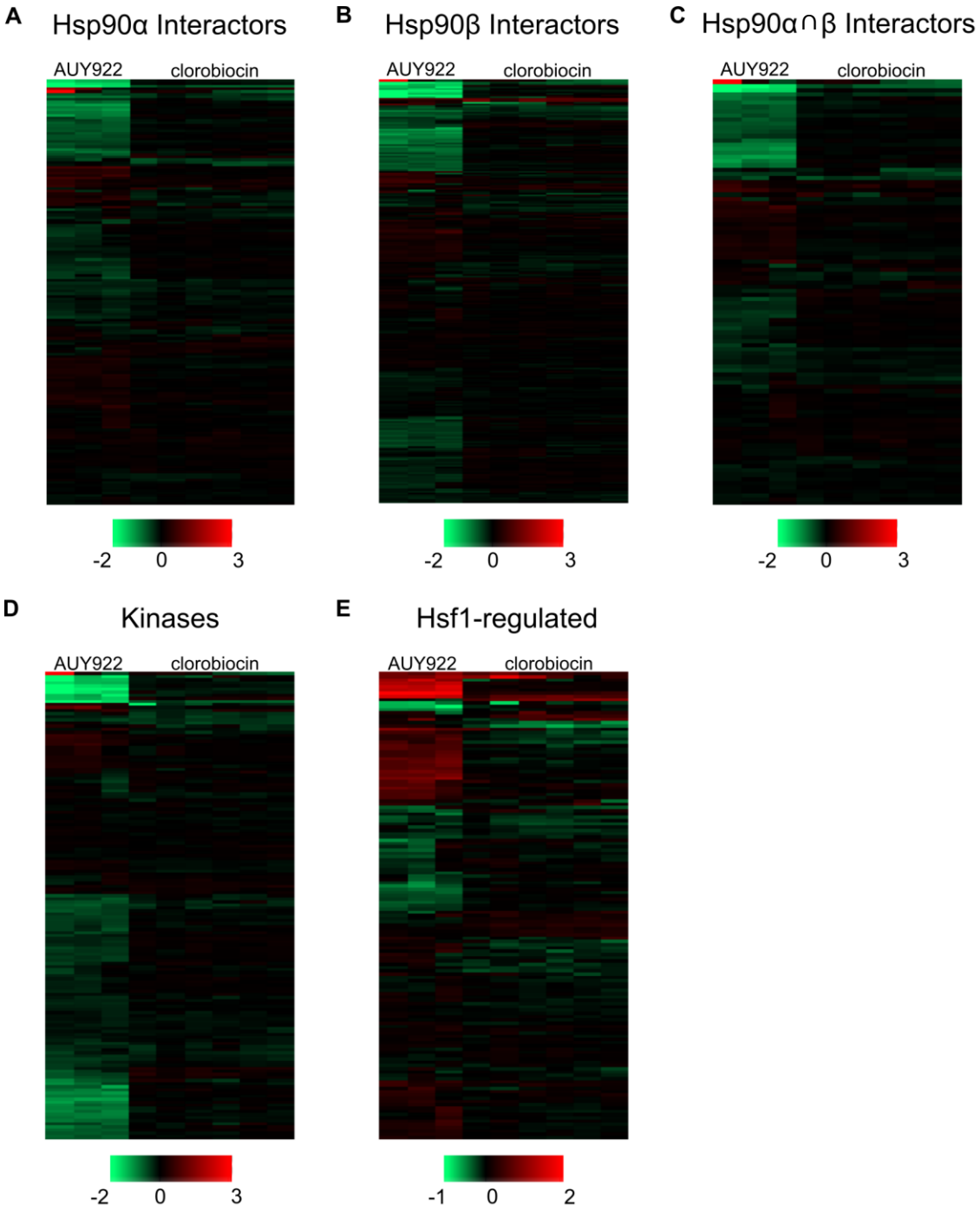

Figure 2.22. Comparison of AUY922 and clorobiocin changes on protein expression of Hsp90 inhibition probes. Heatmaps of protein expression changes were made as previously described in **Figure 2.19**. The numbers in the color keys located at the bottom of each panel are the log2(treated/control) for each biological experiment (n=3 for AUY922, n=6 for clorobiocin). Panel A: Hsp90α interactors. Panel B: Hsp90β interactors. Panel C: Intersect (∩) of Hsp90α and Hsp90β interactors. Panel C: Hsp90 dependent. Panel E: Kinases. Panel F: Hsf1-regulated.

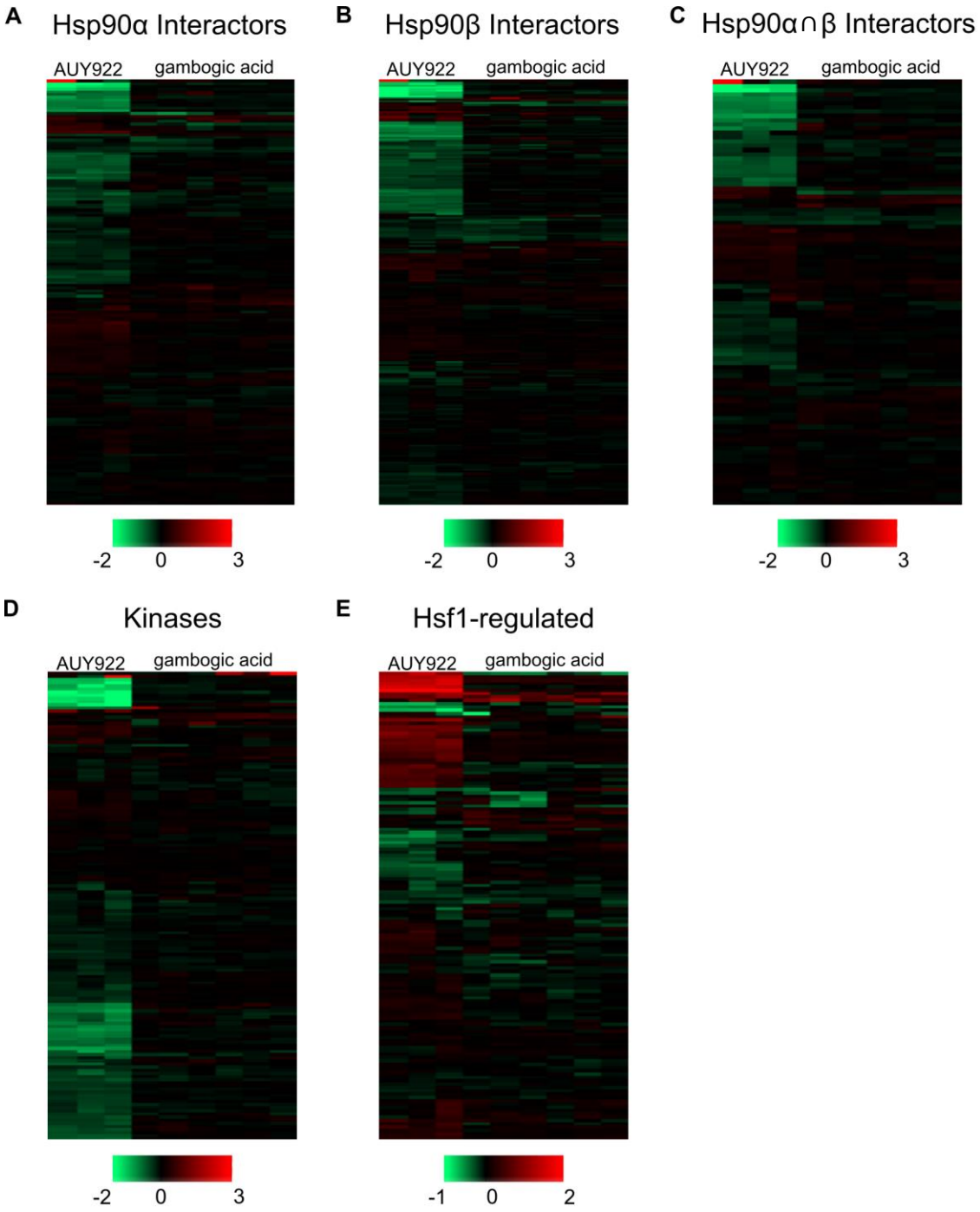

Figure 2.23. Comparison of AUY922 and gambogic acid changes on protein expression of Hsp90 inhibition probes. Heatmaps of protein expression changes were made as previously described in **Figure 2.19**. The numbers in the color keys located at the bottom of each panel are the log2(treated/control) for each biological experiment (n=3 for AUY922, n=6 for gambogic acid). Panel A: Hsp90α interactors. Panel B: Hsp90β interactors. Panel C: Intersect (∩) of Hsp90α and Hsp90β interactors. Panel C: Hsp90 dependent. Panel E: Kinases. Panel F: Hsf1-regulated.

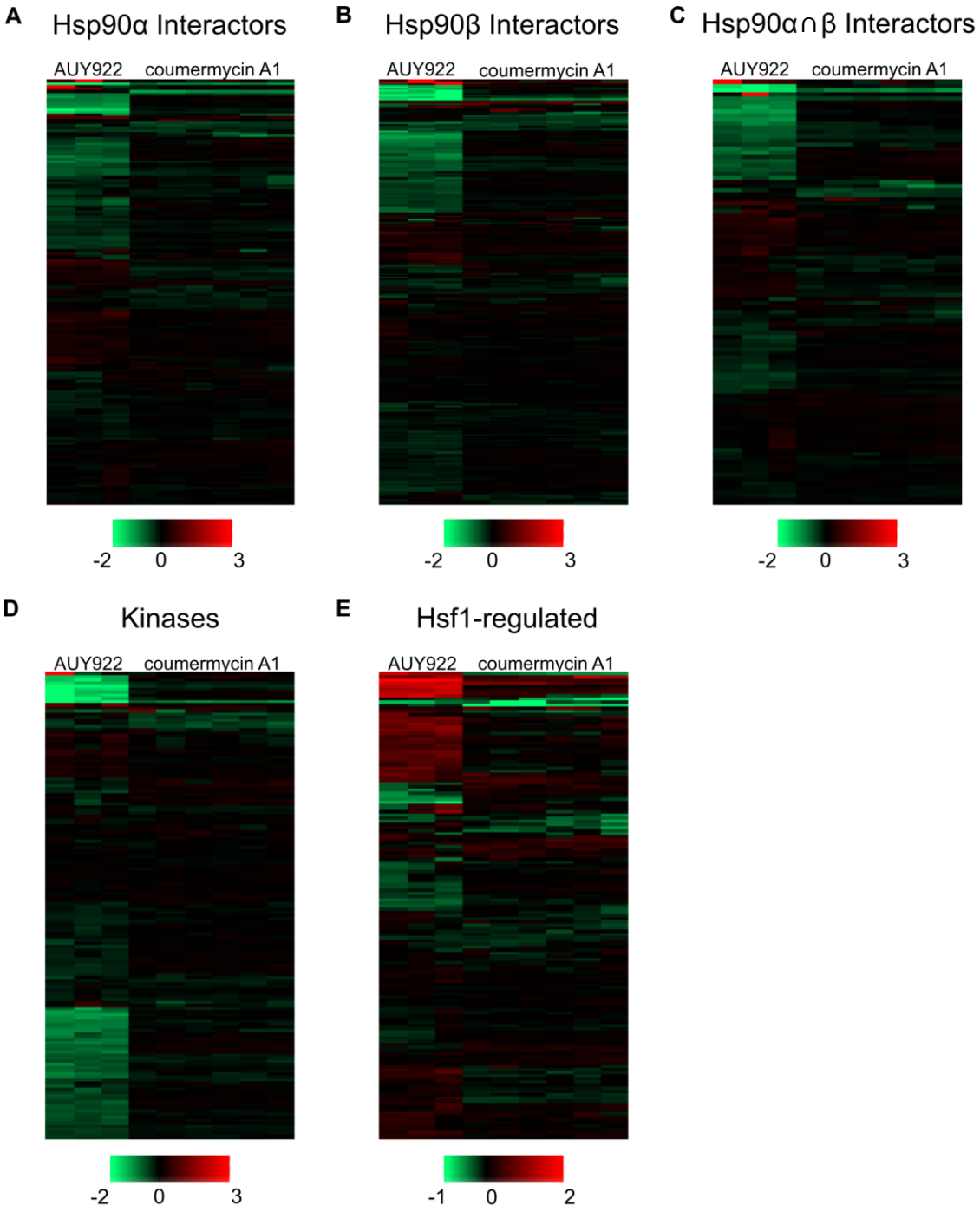

Figure 2.24. Comparison of AUY922 and coumermycin A1 changes on protein expression of Hsp90 inhibition probes. Heatmaps of protein expression changes were made as previously described in **Figure 2.19**. The numbers in the color keys located at the bottom of each panel are the log2(treated/control) for each biological experiment (n=3 for AUY922, n=6 for coumermycin A1). Panel A: Hsp90α interactors. Panel B: Hsp90β interactors. Panel C: Intersect (∩) of Hsp90α and Hsp90β interactors. Panel C: Hsp90 dependent. Panel E: Kinases. Panel F: Hsf1-regulated.

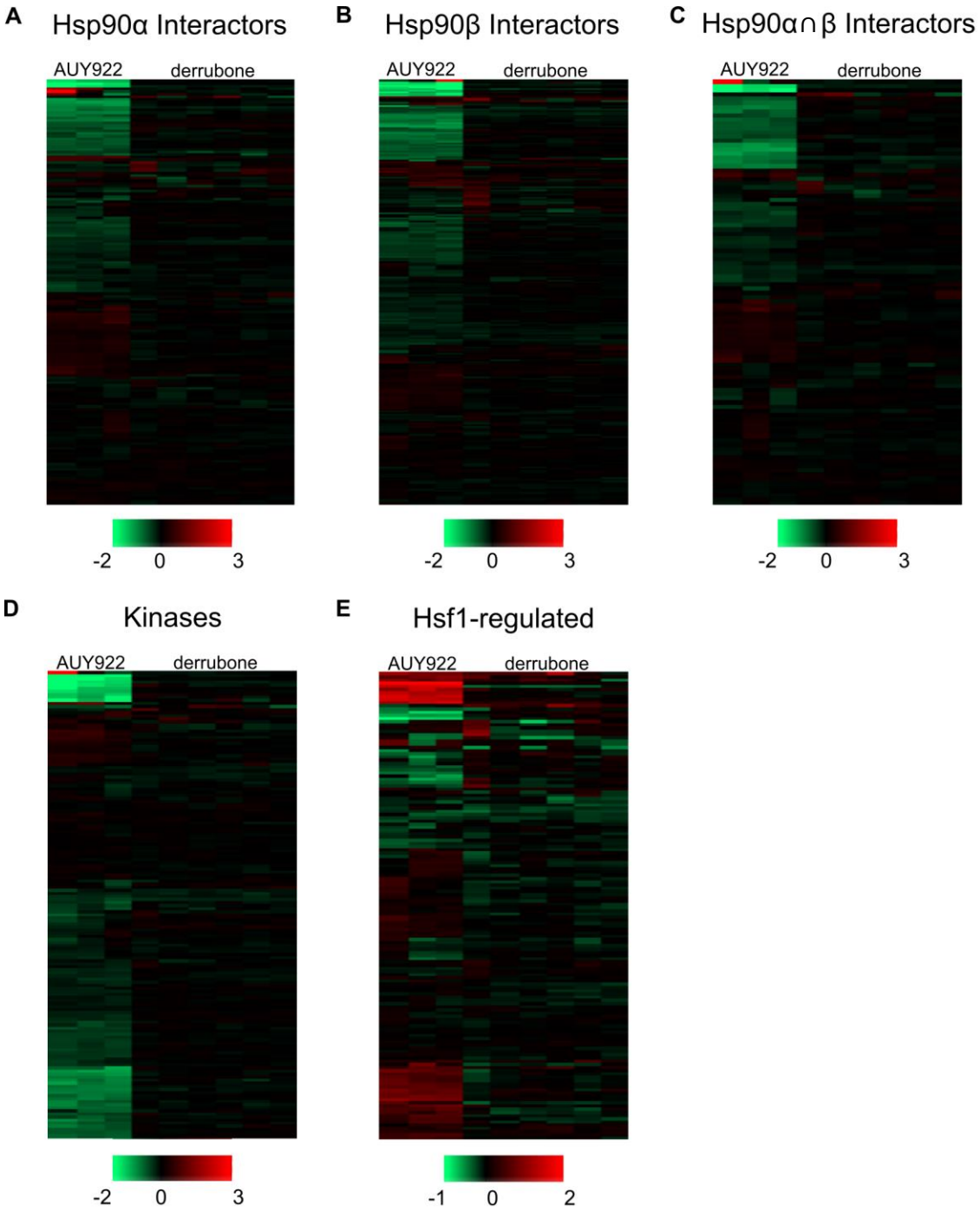

Figure 2.25. Comparison of AUY922 and derrubone changes on protein expression of Hsp90 inhibition probes. Heatmaps of protein expression changes were made as previously described in **Figure 2.19**. The numbers in the color keys located at the bottom of each panel are the log2(treated/control) for each biological experiment (n=3 for AUY922, n=6 for derrubone). Panel A: Hsp90α interactors. Panel B: Hsp90β interactors. Panel C: Intersect (∩) of Hsp90α and Hsp90β interactors. Panel C: Hsp90 dependent. Panel E: Kinases. Panel F: Hsf1-regulated.

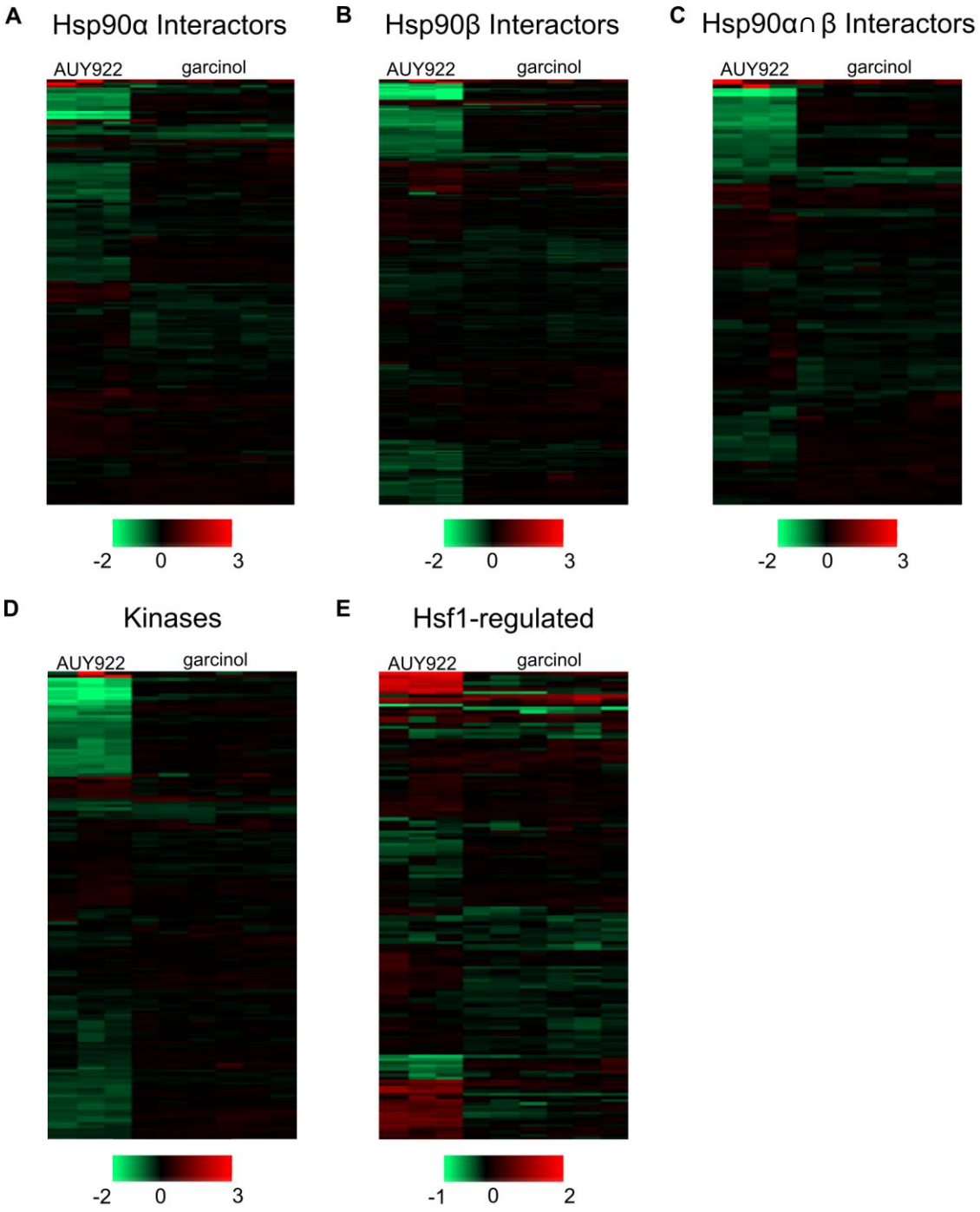

Figure 2.26. Comparison of AUY922 and garcinol changes on protein expression of Hsp90 inhibition probes. Heatmaps of protein expression changes were made as previously described in **Figure 2.19**. The numbers in the color keys located at the bottom of each panel are the log2(treated/control) for each biological experiment (n=3 for AUY922, n=6 for garcinol). Panel A: Hsp90α interactors. Panel B: Hsp90β interactors. Panel C: Intersect (∩) of Hsp90α and Hsp90β interactors. Panel C: Hsp90 dependent. Panel E: Kinases. Panel F: Hsf1-regulated.

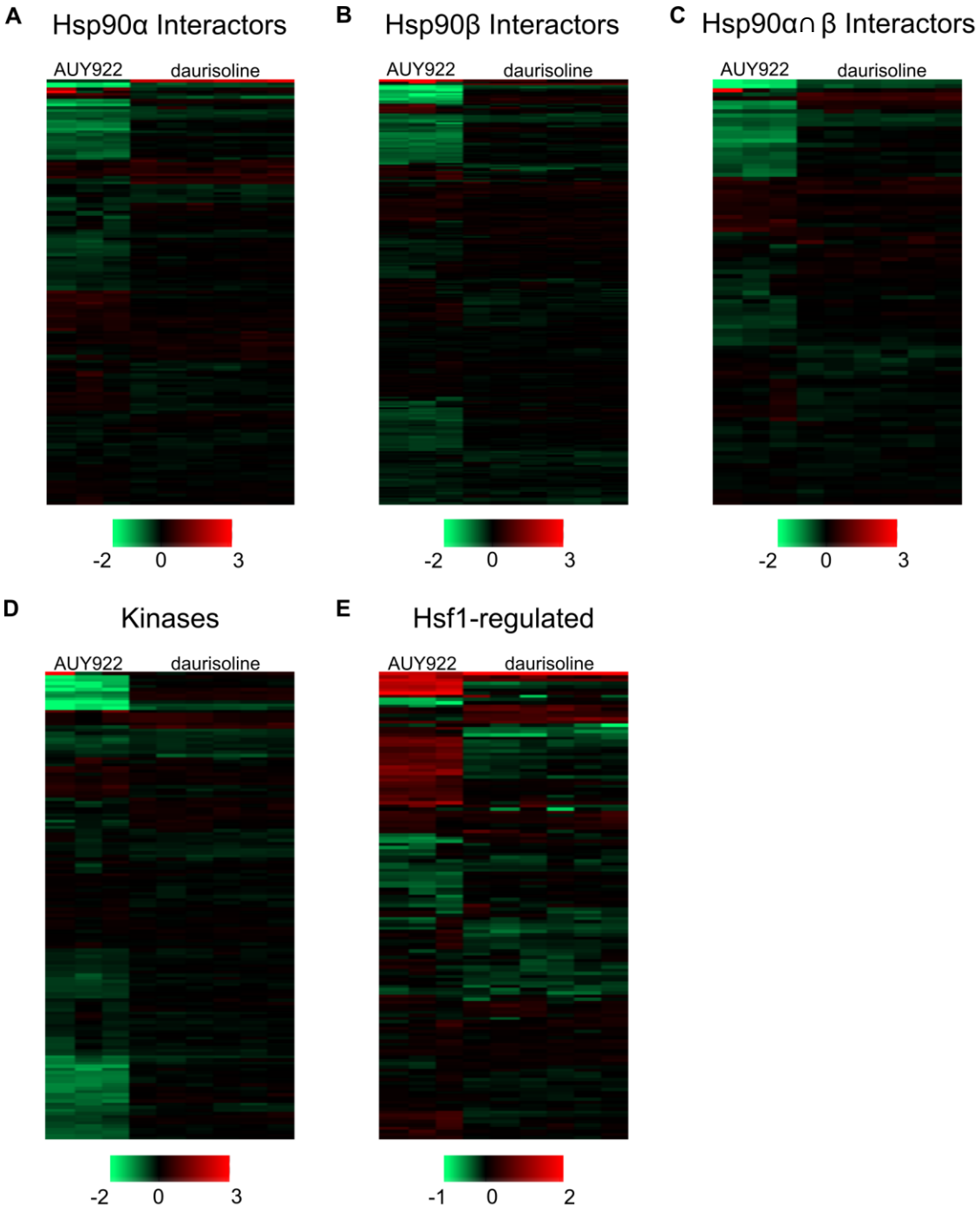

Figure 2.27. Comparison of AUY922 and daurisoline changes on protein expression of Hsp90 inhibition probes. Heatmaps of protein expression changes were made as previously described in **Figure 2.19**. The numbers in the color keys located at the bottom of each panel are the log2(treated/control) for each biological experiment (n=3 for AUY922, n=6 for daurisoline). Panel A: Hsp90α interactors. Panel B: Hsp90β interactors. Panel C: Intersect (∩) of Hsp90α and Hsp90β interactors. Panel C: Hsp90 dependent. Panel E: Kinases. Panel F: Hsf1-regulated.

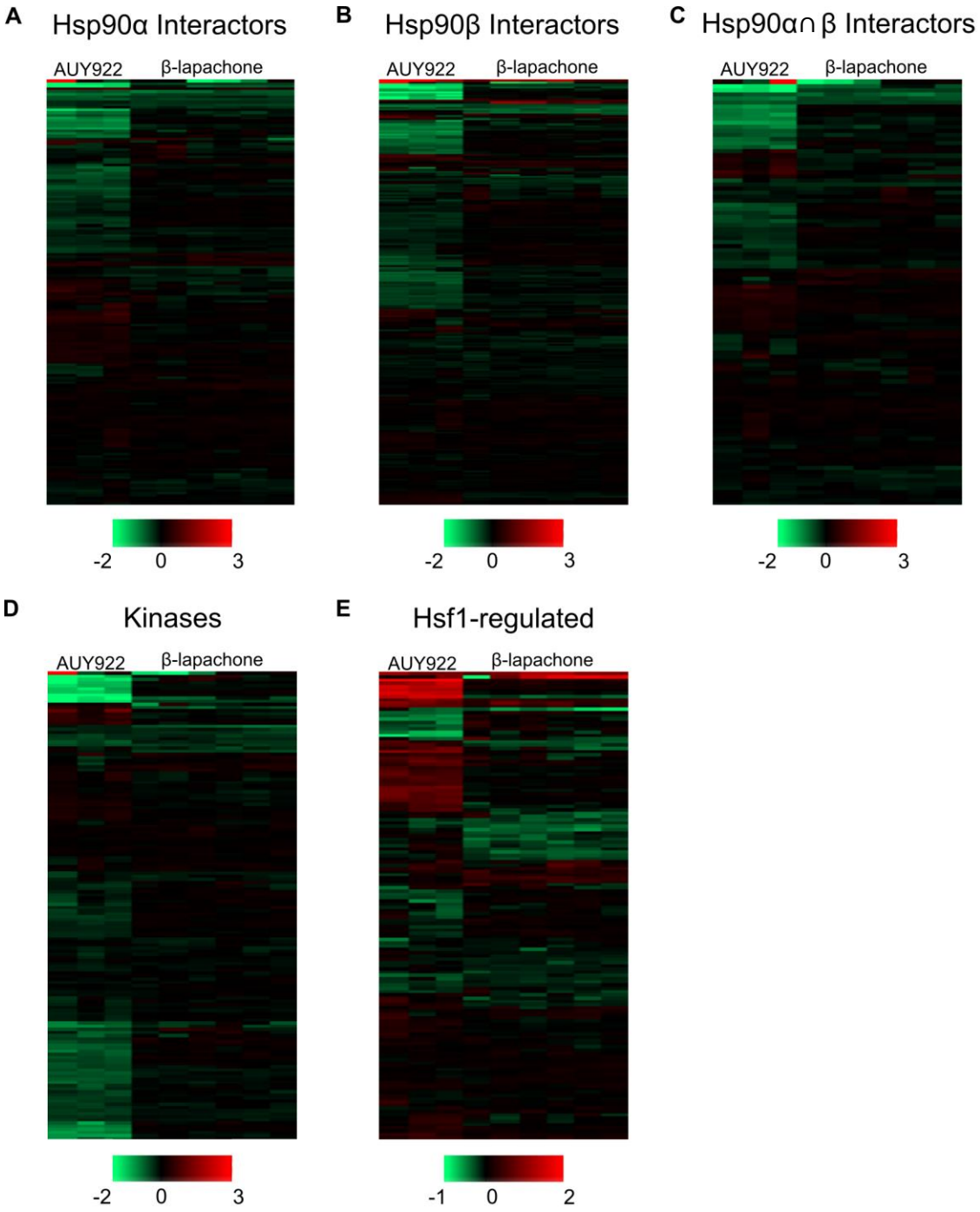

Figure 2.28. Comparison of AUY922 and β-lapachone changes on protein expression of Hsp90 inhibition probes. Heatmaps of protein expression changes were made as previously described in **Figure 2.19**. The numbers in the color keys located at the bottom of each panel are the log2(treated/control) for each biological experiment (n=3 for AUY922, n=6 for β-lapachone). Panel A: Hsp90α interactors. Panel B: Hsp90β interactors. Panel C: Intersect (∩) of Hsp90α and Hsp90β interactors. Panel C: Hsp90 dependent. Panel E: Kinases. Panel F: Hsf1-regulated.

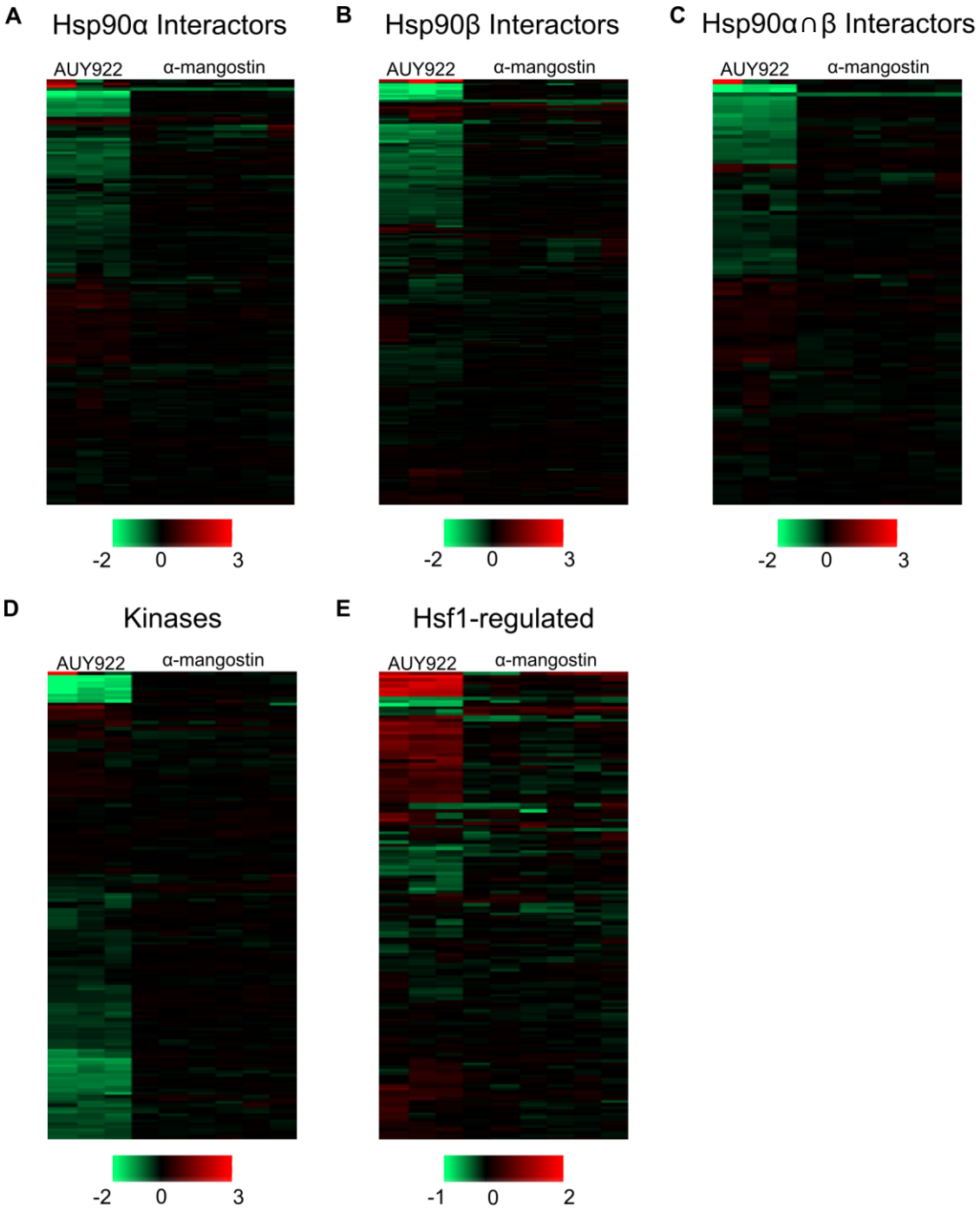

Figure 2.29. Comparison of AUY922 and α-mangostin changes on protein expression of Hsp90 inhibition probes. Heatmaps of protein expression changes were made as previously described in **Figure 2.19**. The numbers in the color keys located at the bottom of each panel are the log2(treated/control) for each biological experiment (n=3 for AUY922, n=6 for α-mangostin). Panel A: Hsp90α interactors. Panel B: Hsp90β interactors. Panel C: Intersect (∩) of Hsp90α and Hsp90β interactors. Panel C: Hsp90 dependent. Panel E: Kinases. Panel F: Hsf1-regulated.

Discussion

I conclude none of the putative compounds in our panel are C-terminal Hsp90 inhibitors. By definition, C-terminal Hsp90 inhibitors are described to deplete Hsp90-dependent clients without inducing the heat shock response. But contrary to previously published literature, none of the compounds in our panel deplete Hsp90-dependent clients. Thus, that is not how these compounds are killing Jurkat cells. However, our data does not refute the *in vitro* assays of compound-Hsp90 interactions previously published, but strongly implies that Hsp90 be re-classified as secondary minor target.

I suggest that the putative C-terminal Hsp90 inhibitors in our panel should be repurposed for other avenues of research. Our data shows that none of the putative C-terminal Hsp90 inhibitors in our compound panel fulfill the requirements of the C-terminal Hsp90 inhibition model, therefore, they cannot be labelled as C-terminal Hsp90 inhibitors. Despite not being C-terminal inhibitors, we have shown that these compounds are capable of inducing apoptosis and robust changes in the proteome dissimilar to AUY922, and with variable degrees of similarity to one another (Table 2.5).

For example, paclitaxel, ailanthone, and daurisoline all have negligible correlations (r = 0.0-0.29) with each compound in our panel (Table 2.5). The lack of conserved proteomic perturbances suggests that each of these compounds induces cell death through a unique mechanism different from the other compounds in the panel. In contrast, coumermycin A1 has the two highest correlations (both moderate) to other compounds in our panel with clorobiocin (r = 0.61) and garcinol (r = 0.52) (Table 2.5). Additionally, coumermycin A1 has low correlations with celastrol (r = 0.35), derrubone

(r = 0.35), β-lapachone (r = 0.49), and α-mangostin (r = 0.34) (Table 2.5). Despite the varying degree of structural similarities between these compounds, their correlations in proteome perturbance suggests a conserved mechanism (Table 2.5).

I propose that clorobiocin, coumermycin A1, derrubone, garcinol, β-lapachone, and α-mangostin induce cell death through a common motif. These six compounds significantly clustered in both of our dendrograms (Figure 2.17, 2.18). As previously shown by our lab group, and repeated here, bootstrapped hierarchical clustering is capable of generating significant clusters of compounds that induce cell death through common mechanisms (compound dose pairs, N-terminal Hsp90 inhibitors, and proteostasis perturbers). I would posit that our current compound library is underpowered and over-varied to postulate a specific mechanism let alone a broader mechanism based on the hierarchical clusters alone. Of the 24 unique compounds in our combined library only 8 are controls, of which 3 are N-terminal Hsp90 inhibitors. In an attempt to use hierarchical clustering to determine (or predict) the mechanism of the compounds in our panel we increased the number of control compounds by adding additional proteomic data from the literature [107]. Unfortunately, the number of proteomic data sets completed in Jurkat cells is sparse so we tried to use data sets from cell lines other than Jurkat. The dendrograms created were heavily dominated by cell line instead of drug induced phenotype (data not shown). Because of this we concluded that the compounds' mechanism of action would need to elucidated through other bioinformatics approaches.

I propose that the C-terminal Hsp90 inhibition model should be scrapped. Our study was conducted with the most readily available C-terminal Hsp90 inhibitors and

none of them showed any indication of inducing cell death through inhibition of Hsp90. Moreover, it is difficult to envision how the inhibition of Hsp90's chaperone function could not lead to disruption of cellular proteostasis and the induction of the heat shock response. With the data presented here, I argue, the number of *post hoc* caveats required to keep the C-terminal Hsp90 inhibition model are too great. Instead, the principle of Occam's razor should be applied. I hypothesize that the previous reports that these compounds are C-terminal Hsp90 inhibitors are artifacts which could be attributed to false positives of high-throughput screening, mortuary science, and off-target effects.

High-throughput screening is a powerful approach for discovering novel compounds as potential drug targets. Unfortunately, high-throughput screening (both experimental and computational) has been well documented for introducing a large number of compounds that no amount of optimization or effort would prevent from being dead ends [111].

Mortuary science is a jargon term that describes conducting research on cells that are in late stage apoptosis. When re-examining the literature, we noticed that many of the studies did not characterize apoptotic status. Additionally, the observations that concluded that these compounds are C-terminal Hsp90 inhibitors (e.g. depletion of Hsp90 clients) were at the tail end of dose series that went up to almost 1 mM in some cases. At these extreme doses, depletion of clients could be due to degradation, and not Hsp90 inhibition.

I conclude celastrol is not an inhibitor of Hsp90 or co-chaperones cdc37, and p23. Celastrol has contradicting reports on molecular targets and mechanism of action in

the literature. Here, celastrol shows no evidence of depleting Hsp90-dependent clients or disruption of the chaperone machinery (**Figures 2.4** and **2.21**). Similarly, Cdc37 has been shown to be pivotal in ensuring proper function of more than 50 % of all kinases. Our data show celastrol treatment causes almost no perturbations in kinase expression (**Figure 2.21, Panel D**). Thus, I argue that celastrol's interactions with Hsp90 should be classified as a secondary or minor target, at best.

Celastrol has also been reported as an inhibitor of the Hsp90 co-chaperone p23. P23 has been shown to be critical in the chaperoning of androgen, glucocorticoid, progesterone, and estrogen steroid hormone receptors. Our mass spectrometry data only detected glucocorticoid (NR3C1), and two progesterone (PGRMC1, and PGRMC2) receptors. None were significantly differentially expressed. NR3C1 was slightly down-regulated, log2(treated/control) -0.38. PGRMC1, and PGRMC2 were slightly up-regulated, log2(treated/control) 0.33, and 0.08 respectively. Based on these results I must conclude that p23 inhibition is not a major mechanism of action for celastrol in our data.

As first reported by the Morimoto lab [80], we see celastrol does induce the heat shock response with the induction of Hsp70 (**Figure 2.4**) and the induction of the HSF1 cassette (**Figure 2.21**), both of which are highly similar to AUY922. There are reports in literature on the significance of celastrol's ability to form Michael adducts with the thiol groups of cysteine, non-specifically. In fact, pre-incubation with DTT is capable of reducing celastrol toxicity, and induction of the antioxidant response [112, 113]. Therefore, I conclude celastrol's induction of the Hsf1-cassette is through the non-specific reaction with protein cysteines.

I conclude ailanthone is not an inhibitor of Hsp90 co-chaperone p23.

Following our procedure for celastrol, we combed our mass spectrometry data for changes in expression of NR3C1, PGRMC1, and PGRMC2 induced by ailanthone treatment. Again, we observed no significant changes for any of the receptors: log2(treated/control) 0.12, 0.07, and -0.03 for NR3C1, PGRMC1, and PGRMC2 respectively. Without the significant down-regulation of these steroid hormone receptors in our data I fail to see how ailanthone is an inhibitor of p23 whose function is obligatory for the stabilization of steroid hormone receptors. Therefore, I conclude that ailanthone is inducing apoptosis through a different mechanism in our cells.

Our data suggest that using Hsp90-dependent client depletion by compound treatment should be framed by a statement of apoptosis. After analyzing our data, we returned to the published literature for explanations for the stark contrast between the conclusions drawn here versus those previously made on these compounds target. We see that many times in the literature, the depletion of Hsp90-dependent clients is not framed by a statement of apoptosis. Indeed, when comparing the treatment concentrations used here and those reported in the literature, these precedents used heroic (greater than 4 times the IC_{50} of cell death marker) amounts of compound to observe client depletion. Moreover, our data show the importance of framing client depletion in relation to a positive control.

CHAPTER III

BIOINFORMATICS ANALYSIS OF PROTEOMIC PERTURBATIONS

Introduction

After concluding that none of the putative compounds in our panel are Hsp90 inhibitors we wanted to further investigate alternative targets and/or mechanisms. Therefore, we completed a bioinformatics study on our proteomics data for enriched GO terms, KEGG pathways, and STRING protein-protein interaction networks. These enriched targets along with literature insights were then used to support alternative targets and mechanisms.

Methods

Enrichment of GO terms and KEGG pathways

The proteins with significantly changed expression were analyzed for enriched GO terms and KEGG pathways using ShinyGO (version 0.75) [114]. The top 30 enriched terms and pathways were generated separately for up- and down-regulated proteins with a FDR *p*-value cutoff of 0.05. A background gene list of proteins detected in the mass

spectrometry experiments for each individual compound was used to filter enrichments. Figures were made using hierarchical clustering trees generated by ShinyGO software in which terms and pathways that share genes cluster together. Dots and *p*-values are reported next to each enrichment; larger dots indicate more significant *p*-values.

Protein-protein interaction networks

Protein-protein interaction networks of significantly changed proteins were created using STRING (version 11.5) [115]. Networks were made with high confidence interaction score (0.7), and medium false discovery rate (5 %). Network edges report confidence, with thicker lines indicating strength of data support. Disconnected protein nodes are hidden from the output figures. A background gene list of proteins detected in the mass spectrometry experiments was used for filtering functional enrichment terms.

Probes of mitochondrial perturbation

Gene lists for the probes of mitochondrial perturbation were obtained from the HUGO Gene Nomenclature Committee [116], and our data. A complete gene list used to make heat maps for mitochondrial ribosome proteins, and each of the five electron transport chain complexes can be found in the digital Appendix.

Results

To validate our bioinformatics pipeline we compared the results obtained from shinyGO and our AUY922 data to N-terminal inhibitors previously published [117-119]. Consistent with the literature our enriched down-regulated terms included: nucleotide

binding, protein kinase activity, cell cycle, DNA metabolic process, RNA processing, protein phosphorylation, rRNA processing, ribosome biogenesis, and helicase activity (**Figure 3.1**). Additionally, our enriched up-regulated terms included: response to unfolded protein, unfolded protein binding, and response to organic substance (**Figure 3.2**). Based on these results we concluded that bioinformatics pipeline is capable of characterizing the other compounds in our panel.

To elucidate potential alternative mechanisms and/or targets of ailanthone we completed bioinformatics analysis on the down- and up-regulated proteins from our proteomics data. Interestingly, ailanthone treatment enriches a plethora of terms indicting down-regulation of proteins involved in the cell cycle, specifically, the metaphase to anaphase transition, and chromosome separation (**Figure 3.3**). Additionally, we enriched terms indicating that ailanthone treatment disrupts mitochondrial health, specifically the mitochondrial electron transport chain (**Figure 3.3**). Ailanthone did not enrich any GO terms or KEGG pathways for the up-regulated protein set.

To visualize the bioinformatics enrichments for ailanthone we created a protein-protein interaction network using STRING. The enriched nodes associated with the electron transport chain are colored yellow (**Figure 3.4**). Additionally, we see a very large number of down-regulated genes associated in ubiquitin proteolysis, indicated by light green and cyan nodes (**Figure 3.4**). The STRING visualization helps illuminate the ubiquitin mediated proteolysis, and oxidative phosphorylation enriched KEGG pathways. These results indicate that ailanthone cytotoxicity can be attributed in part to disruption of mitochondrial health.

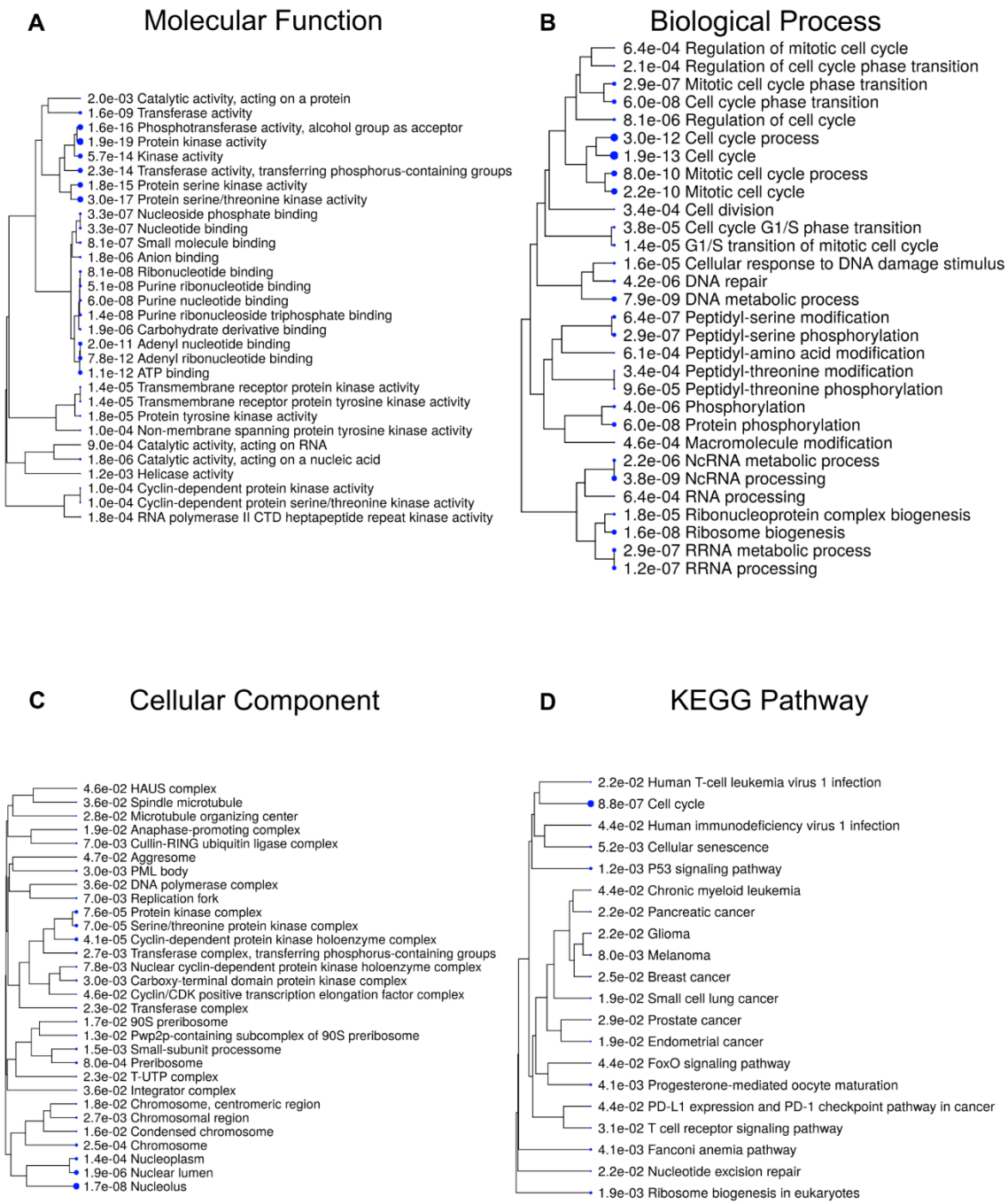

Figure 3.1. GO analysis for AUY922 down-regulated proteins. Enrichment of GO terms and KEGG pathways for the significant differentially expressed proteins were generated using ShinyGO as described in Methods. Enriched terms and *p*-values are reported in hierarchical cluster trees with pathways sharing multiple genes clustering together. Larger blue dots indicate more significant *p*-values. Panel A: Molecular function. Panel B: Biological process. Panel C: Cellular component. Panel D: KEGG pathway.

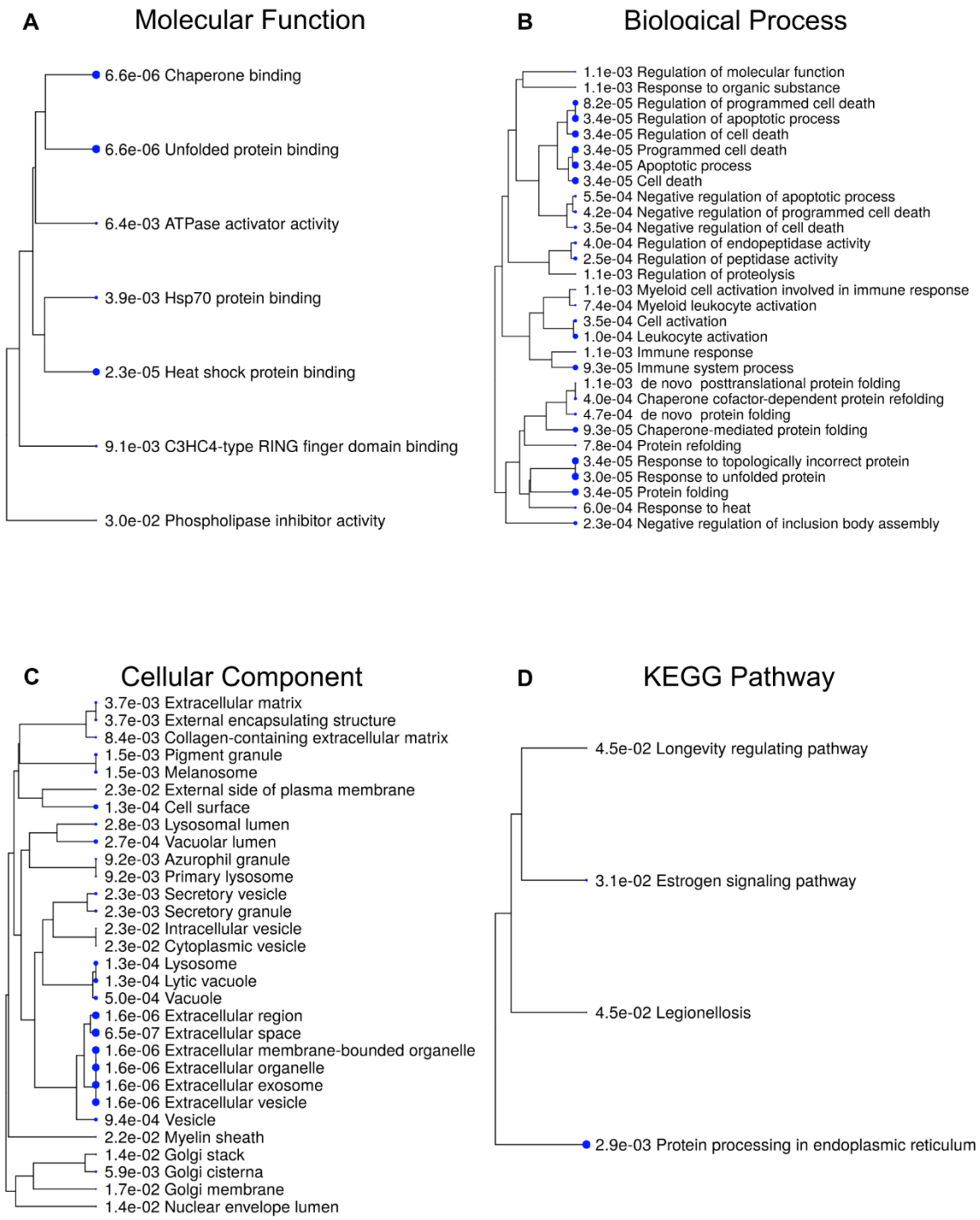

Figure 3.2. GO analysis for AUY922 up-regulated proteins. Enrichment of GO terms and KEGG pathways for the significant differentially expressed proteins were generated as described in **Figure 3.1** and Methods. Enriched terms and *p*-values are reported. Larger blue dots indicate more significant *p*-values. Panel A: Molecular function. Panel B: Biological process. Panel C: Cellular component. Panel D: KEGG pathway.

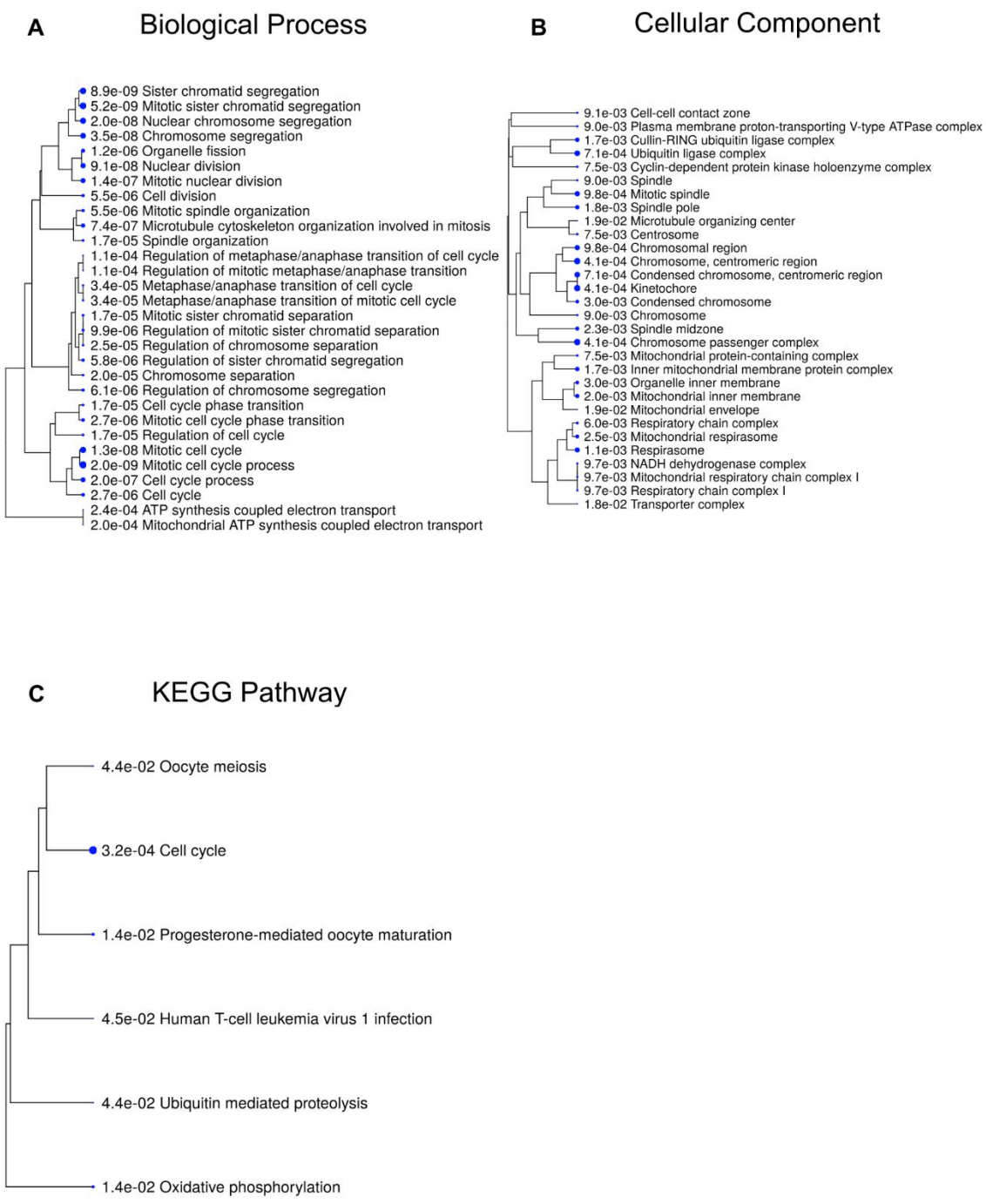

Figure 3.3. GO analysis for ailanthone down-regulated proteins. Enrichment of GO terms and KEGG pathways for the significant differentially expressed proteins were generated as described in **Figure 3.1** and Methods. Enriched terms and *p*-values are reported. Larger blue dots indicate more significant *p*-values. Panel A: Biological process. Panel B: Cellular component. Panel C: KEGG pathway.

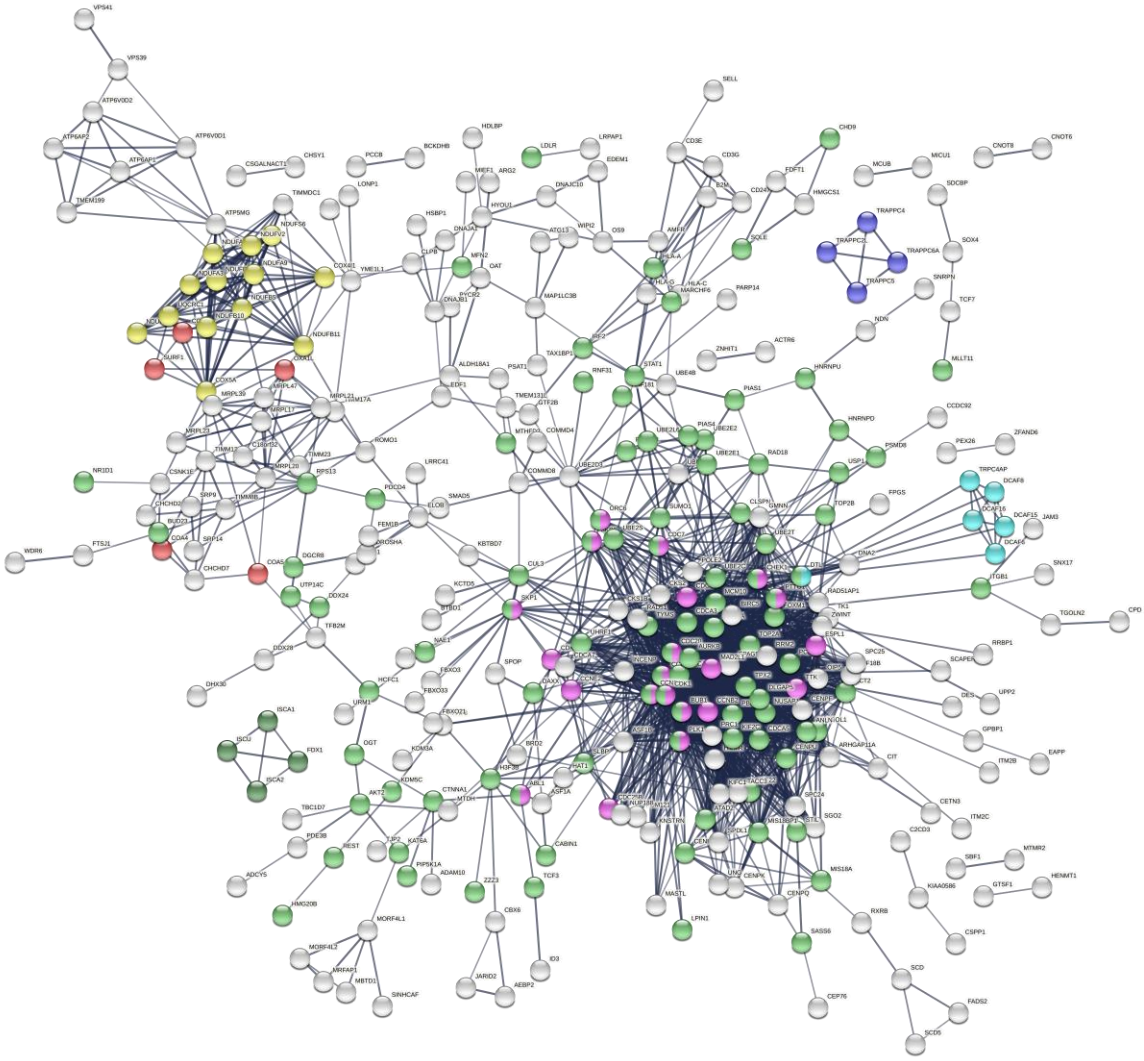

Figure 3.4. Protein-protein interaction network of ailanthone down-regulated proteins. Protein-protein interaction network for the significant differentially expressed proteins were generated using STRING as described in Methods. Protein nodes are colored based on functional enrichments: Yellow: GO 0042775 Mitochondrial ATP synthesis coupled electron transport, Blue: GOCC:0030008 TRAPP complex, Light green: KW-0832 Ubl conjugation, Red: GO:0017004 Cytochrome complex assembly, Pink: hsa04110 cell cycle, Dark green: GOCC:1990230 Iron-sulfur cluster transfer complex, Cyan: GO:0080008 Cul4-Ring E3 ubiquitin ligase complex.

Again, to elucidate alternative targets and/or mechanisms of celastrol we completed bioinformatics analysis on the differentially expression proteins. Interestingly, celastrol treatment has a drastic impact on mitochondrial translation (**Figure 3.5**). The enrichment of these terms can be attributed to the fact that 19 mitochondrial ribosome proteins are significantly down-regulated. Additionally, the enrichment of the transmembrane proteins associated with the mitochondria outer membrane which transfer proteins between the TOM and SAM complex. Both of these enrichments are apparent in the protein-protein interaction network (**Figure 3.6**). These results indicate that celastrol cytotoxicity, is in part, do to disruption of mitochondrial health.

GO analysis of induced proteins by celastrol treatment was especially interesting. First, celastrol treatment appears to induce the immune response in our Jurkat cells. Terms associated with neutrophil activation, excretory granules, lysosomes, and vacuoles dominate the enriched terms for biological processes, and cellular components (**Figure 3.7**). Drugs capable of interacting, and stimulating immune receptors have been reported in literature [120]. As mentioned previously, celastrol is a promiscuous antagonist with the ability to react with the thiol groups of cysteine, non-specifically. Additionally, we also see an enrichment of serine biosynthetic pathways. Serine has been shown to aid in alleviating oxidative stress through the glutathione synthesis [121]. Both of serine family amino acid process (red nodes), and glutathione metabolism, and selenocysteine (yellow nodes) pathways are apparent in our protein-protein interaction network (**Figure 3.8**). These results indicate that celastrol is capable of inducing the immune response through interactions with immune receptors, and the cells are attempting to resolve the oxidative stress induced by celastrol treatment with synthesis of glutathione.

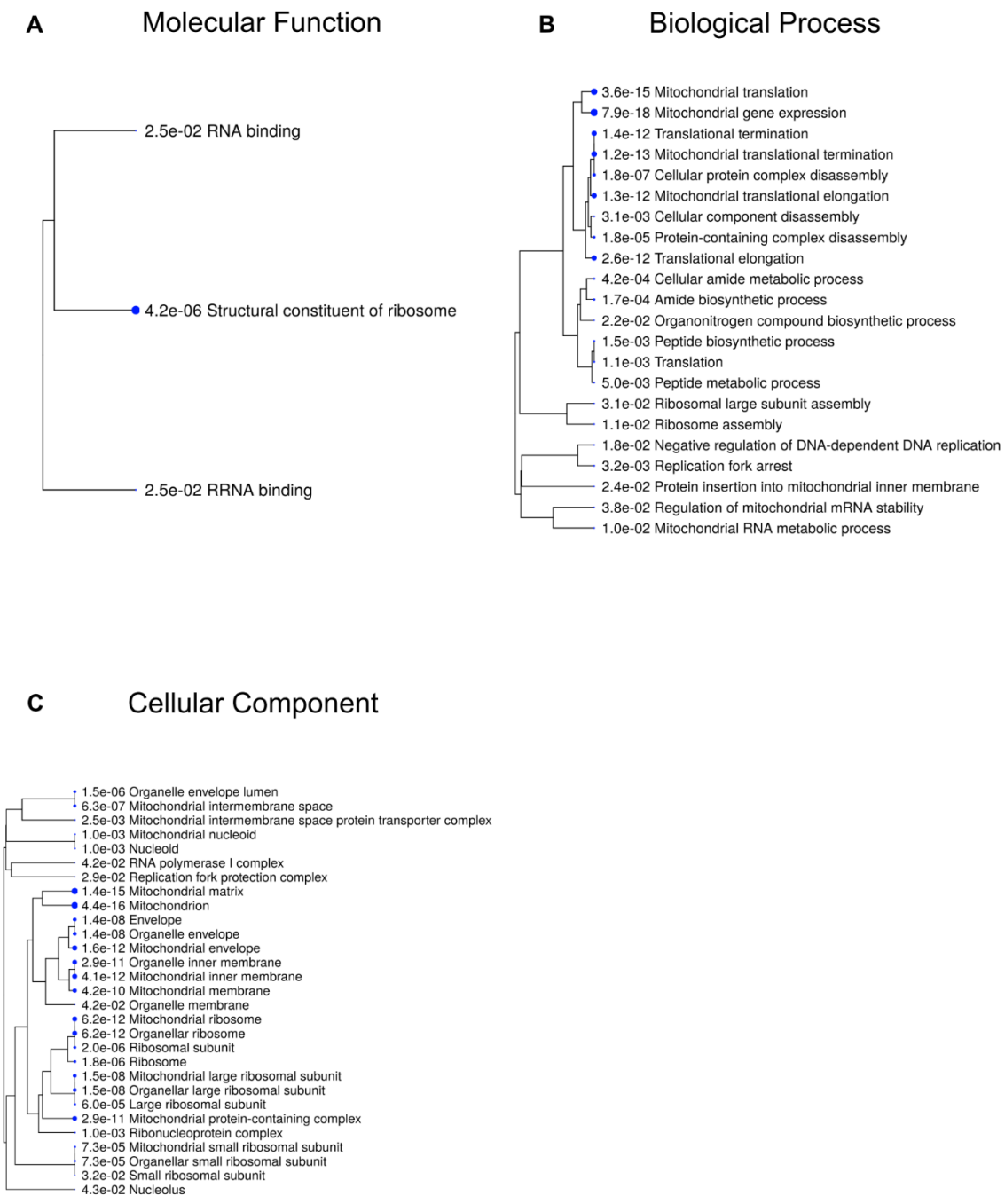

Figure 3.5. GO analysis for celastrol down-regulated proteins. Enrichment of GO terms and KEGG pathways for the significant differentially expressed proteins were generated as described in **Figure 3.1** and Methods. Enriched terms and *p*-values are reported. Larger blue dots indicate more significant *p*-values. Panel A: Molecular function. Panel B: Biological process. Panel C: Cellular component.

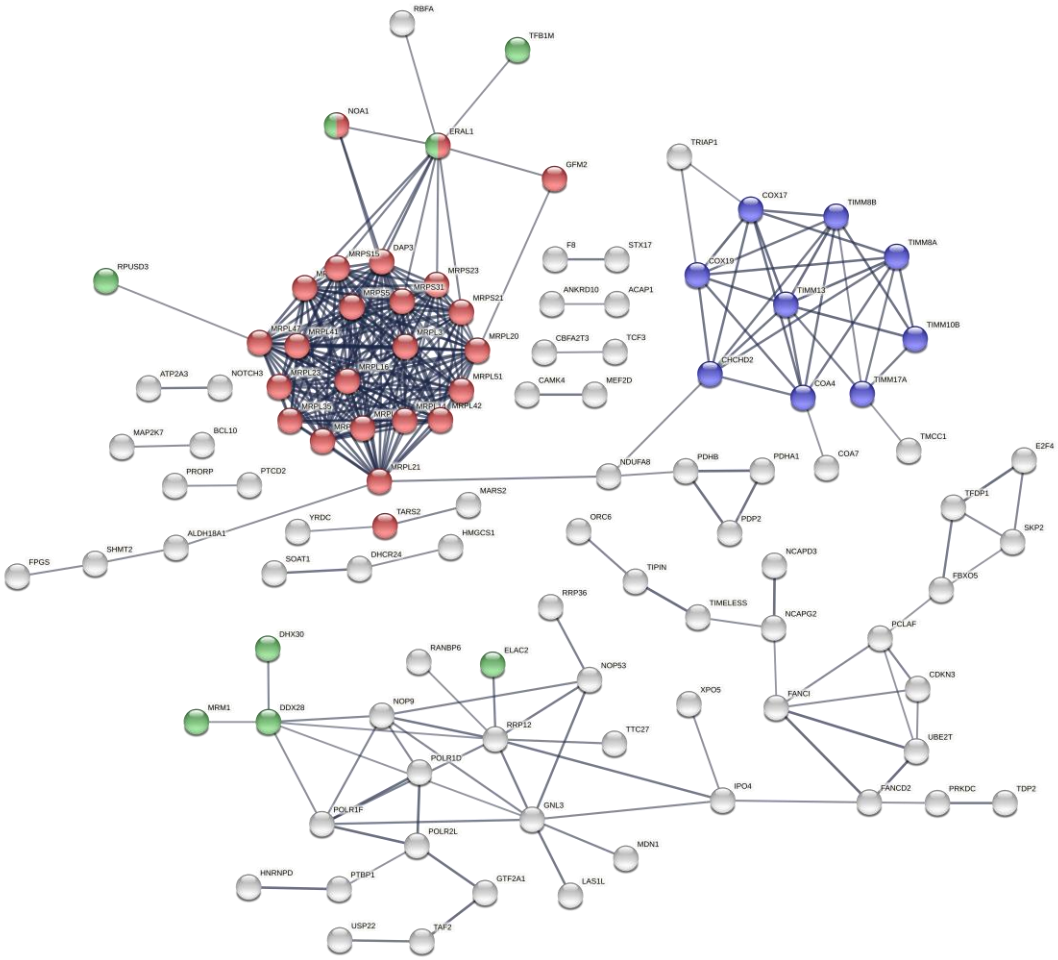

Figure 3.6. Protein-protein interaction network of celastrol down-regulated proteins. Protein-protein interaction network of the significant differentially expressed proteins as described in **Figure 3.4** and Methods. Protein nodes are colored based on functional enrichments: Red: GO:0032543 Mitochondrial translation, Blue: CL:13622 Mitochondrial protein import, and SAM complex, Green: PMID:28285835 (2017) Regulation of Mammalian Mitochondrial Gene Expression: Recent Advances.

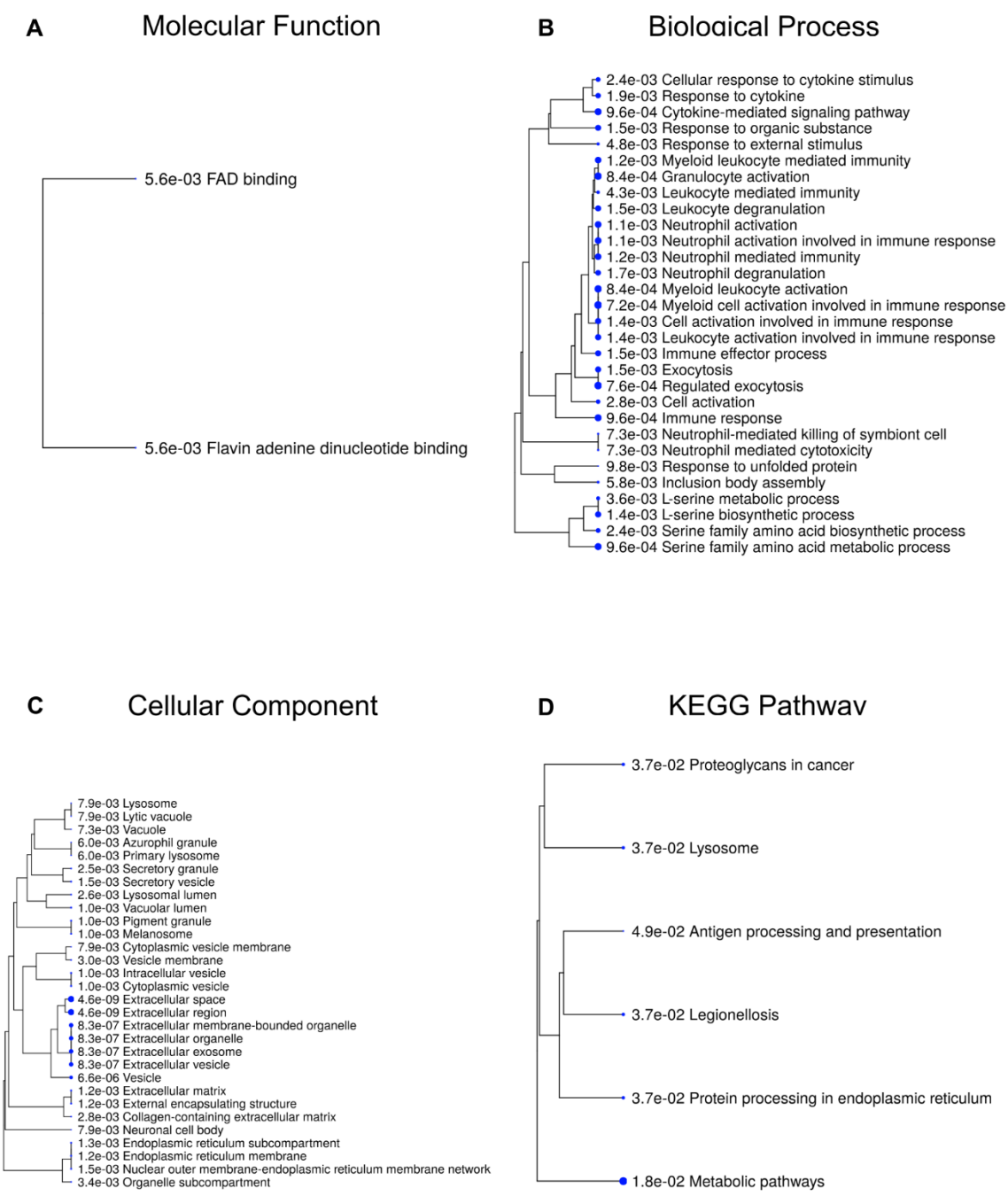

Figure 3.7. GO analysis for celastrol up-regulated proteins. Enrichment of GO terms and KEGG pathways for the significant differentially expressed proteins were generated as described in **Figure 3.1** and Methods. Enriched terms and *p*-values are reported. Larger blue dots indicate more significant *p*-values. Panel A: Molecular function. Panel B: Biological process. Panel C: Cellular component. Panel D: KEGG pathway.

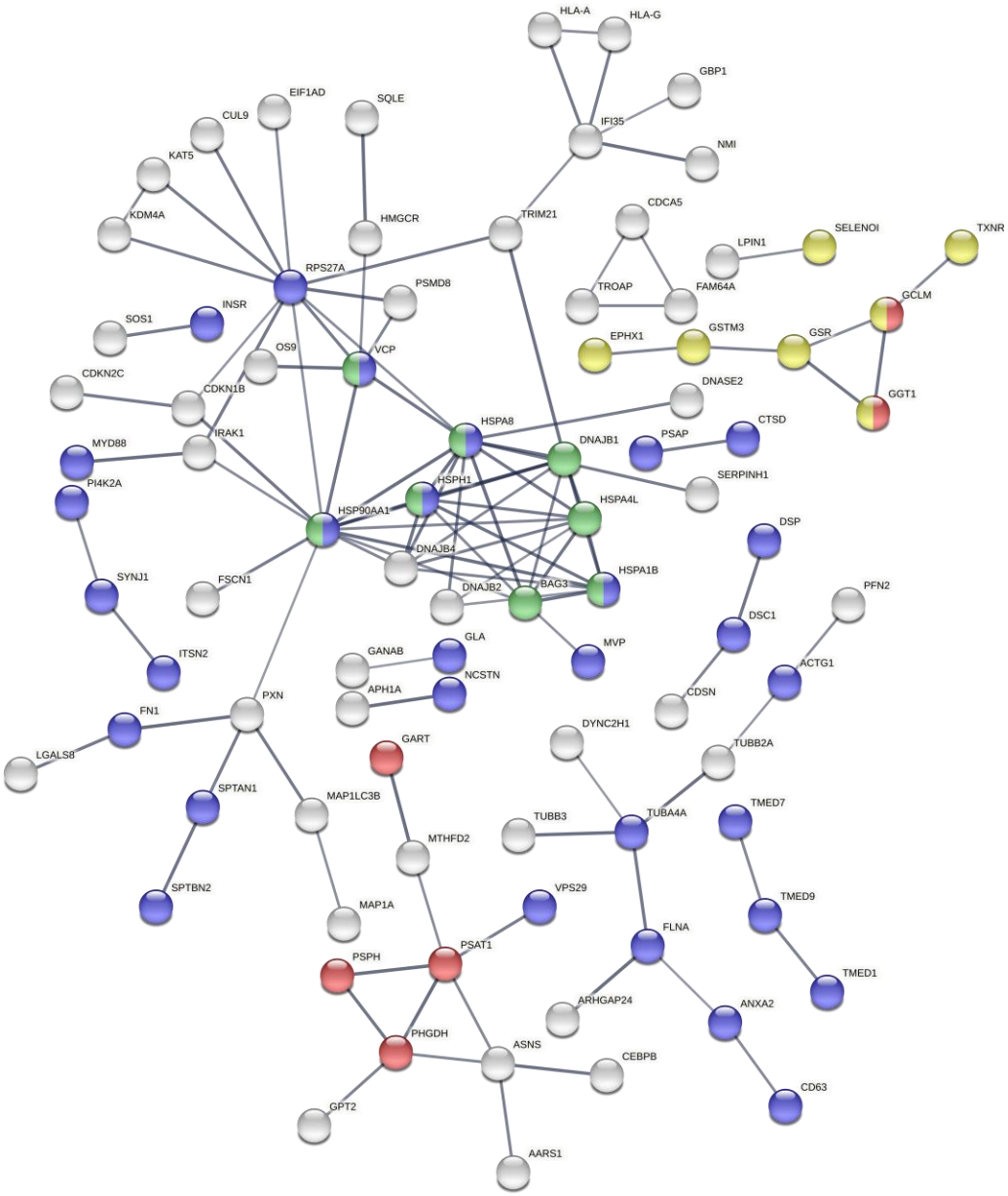

Figure 3.8. Protein-protein interaction network of celastrol up-regulated proteins. Protein-protein interaction network of the significant differentially expressed proteins as described in **Figure 3.4** and Methods. Protein nodes are colored based on functional enrichments: Red: GO:0009069 Serine family amino acid metabolic process, Yellow: CL:13061 Glutathione metabolism, and selenocysteine, Blue: GO:0016192 Vesicle-mediated transport, Green: HSA-3371556 Cellular response to heat stress.

Bioinformatics analysis of clorobiocin down-regulated proteins indicates that clorobiocin also targets the mitochondria (**Figure 3.9**). Enriched GO terms are comprised of both the electron transport chain, and the mitochondrial ribosome. These enrichments are evident in protein-protein interaction network, with essentially two-thirds of the nodes being associated with the electron transport chain (blue nodes) or the mitochondrial ribosome (green nodes) (**Figure 3.10**). These results indicate that clorobiocin also has a mitochondrial perturbation motif associated with cytotoxicity.

Clorobiocin up-regulated proteins enriched GO terms for molecular function, and biological process are dominated by amino acid transmembrane transporters followed by steroid, sterol, and cholesterol biosynthetic processes (**Figure 3.11**). These results are evident in the protein-protein interaction network (**Figure 3.12**).

Gambogic acid down-regulated GO terms indicate translation arrest to the endoplasmic reticulum. Major motifs include: cytosolic ribosomes, RNA processing, and SRP-dependent co-translational protein targeting to membrane (**Figure 3.13**). Down-regulation of ribosomes, and ribosome biogenesis is apparent in the protein-protein interaction network (**Figure 3.14**). Bioinformatics analysis of up-regulated GO terms for gambogic acid only enriched two terms: transporter complex, and transmembrane transporter complex (**Figure 3.15**). The STRING analysis showed the enrichment of mitochondria respiratory chain complex I (red nodes) (**Figure 3.16**). These results suggest that gambogic acid perturbs endoplasmic reticulum proteostasis.

Figure 3.9. GO analysis for clorobiocin down-regulated proteins. Enrichment of GO terms and KEGG pathways for the significant differentially expressed proteins were generated as described in **Figure 3.1** and Methods. Enriched terms and *p*-values are reported. Larger blue dots indicate more significant *p*-values. Panel A: Molecular function. Panel B: Biological process. Panel C: Cellular component. Panel D: KEGG pathway.

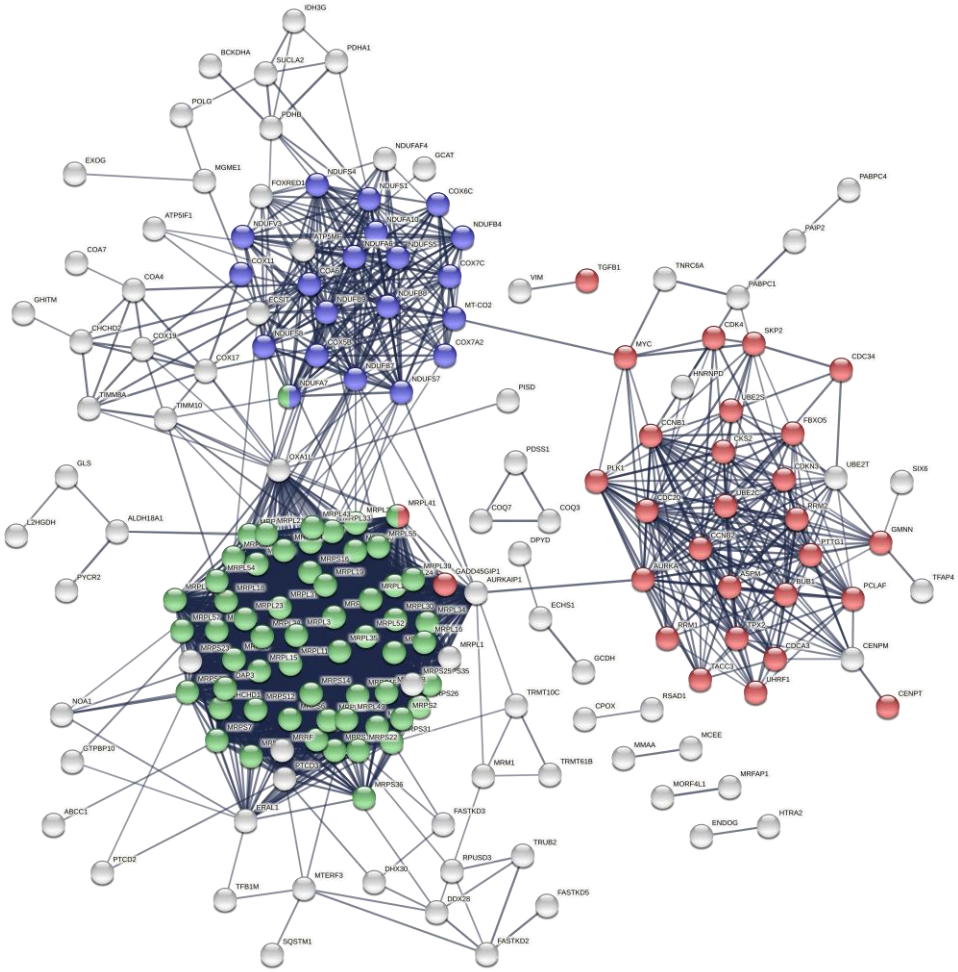

Figure 3.10. Protein-protein interaction network of clorobiocin down-regulated proteins. Protein-protein interaction network of the significant differentially expressed proteins as described in **Figure 3.4** and Methods. Protein nodes are colored based on functional enrichments: Red: GO:0007049 Cell cycle, Blue: GO:0022900 Electron transport chain, Green: GO:0005761 Mitochondrial ribosome.

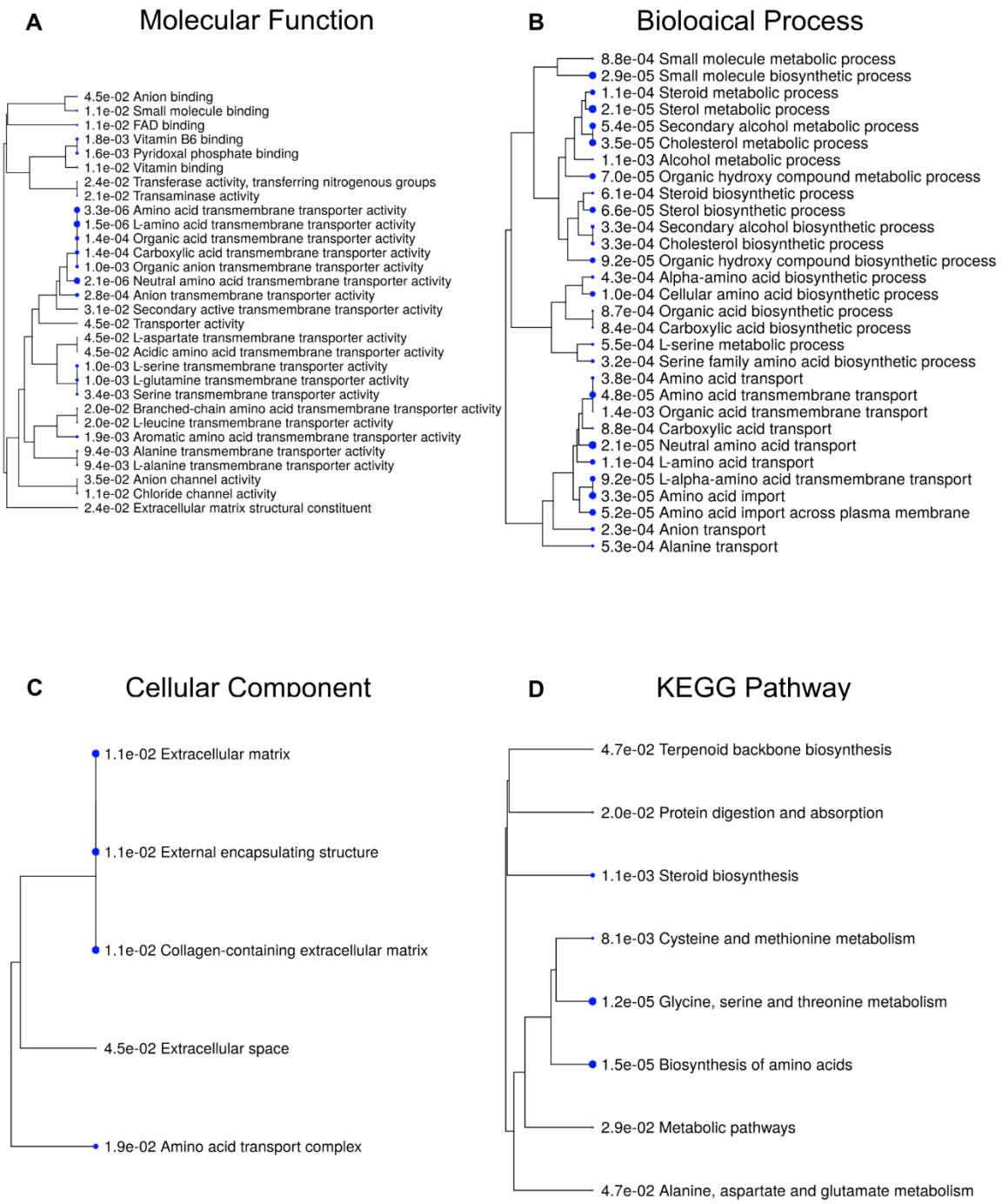

Figure 3.11. GO analysis for clorobiocin up-regulated proteins. Enrichment of GO terms and KEGG pathways for the significant differentially expressed proteins were generated as described in **Figure 3.1** and Methods. Enriched terms and *p*-values are reported. Larger blue dots indicate more significant *p*-values. Panel A: Molecular function. Panel B: Biological process. Panel C: Cellular component. Panel D: KEGG pathway.

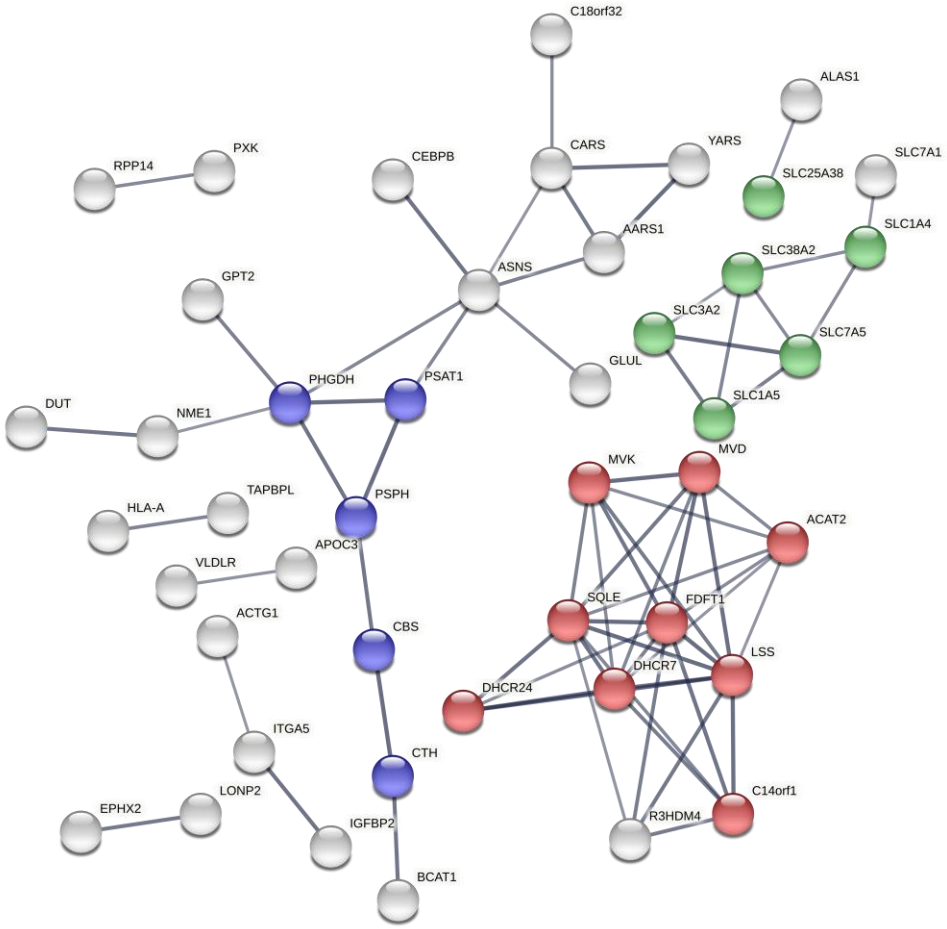

Figure 3.12. Protein-protein interaction network of clorobiocin up-regulated proteins. Protein-protein interaction network of the significant differentially expressed proteins as described in **Figure 3.4** and Methods. Protein nodes are colored based on functional enrichments: Red: GO:0016126 Sterol biosynthesis process, Blue: GO:0009069 Serine family amino acid metabolic process, Green: GO:0015175 Neutral amino acid transmembrane transporter activity.

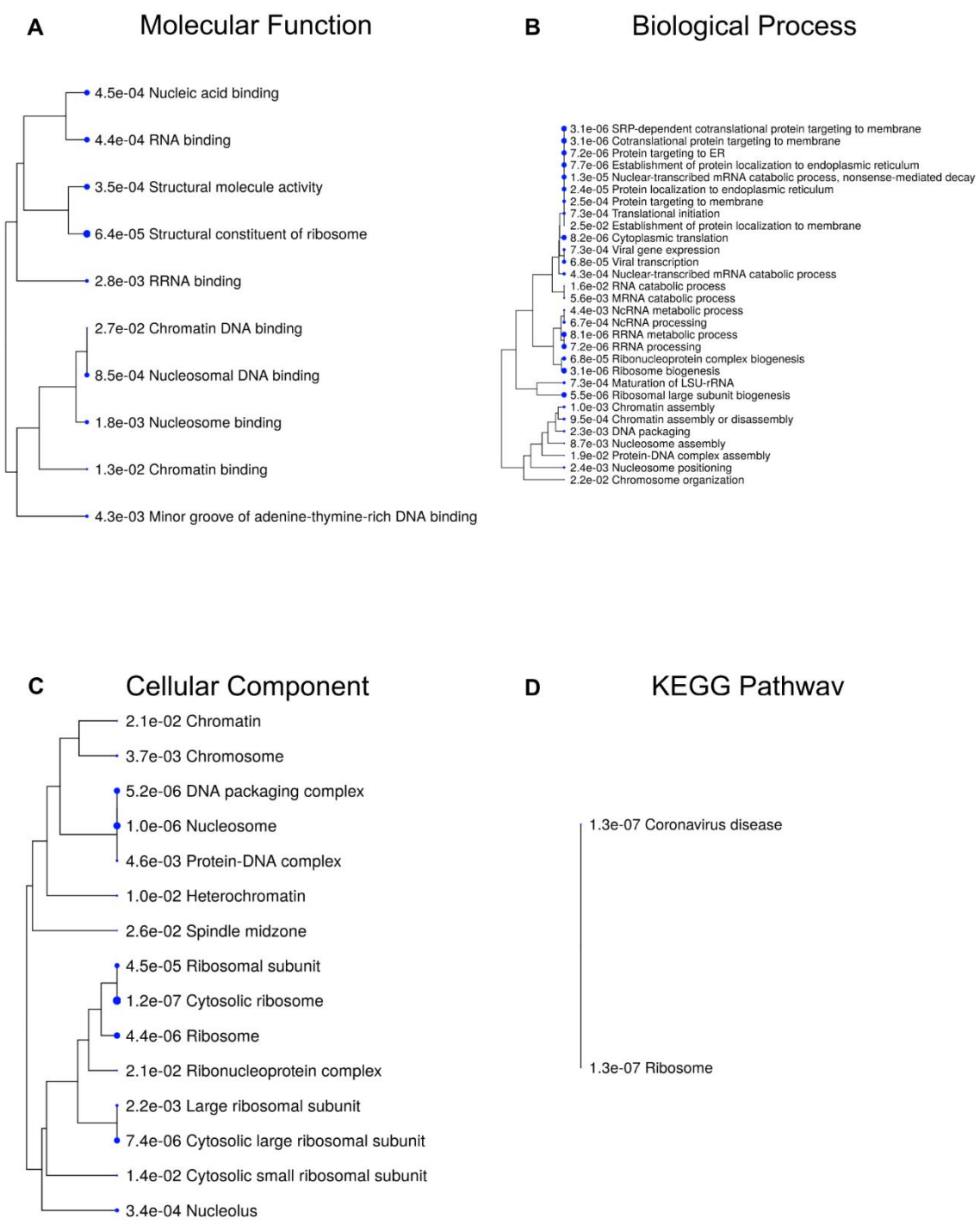

Figure 3.13. GO analysis for gambogic acid down-regulated proteins. Enrichment of GO terms and KEGG pathways for the significant differentially expressed proteins were generated as described in **Figure 3.1** and Methods. Enriched terms and *p*-values are reported. Larger blue dots indicate more significant *p*-values. Panel A: Molecular function. Panel B: Biological process. Panel C: Cellular component. Panel D: KEGG pathway.

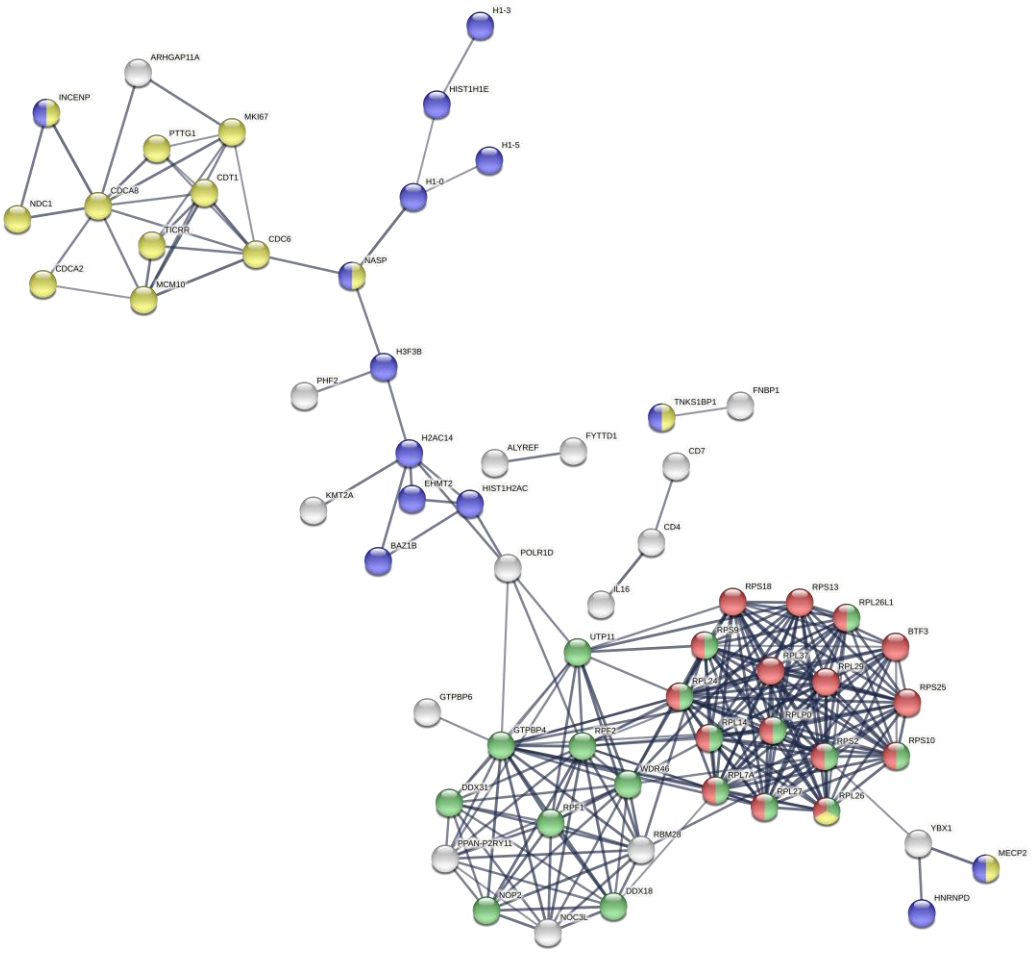

Figure 3.14. Protein-protein interaction network of gambogic acid down-regulated proteins. Protein-protein interaction network of the significant differentially expressed proteins as described in **Figure 3.4** and Methods. Protein nodes are colored based on functional enrichments: Red: GO:0005840 Ribosome, Blue: GO:0000785 Chromatin, Green: GO:0042254 Ribosome biogenesis, Yellow: GO:0007049 Cell cycle.

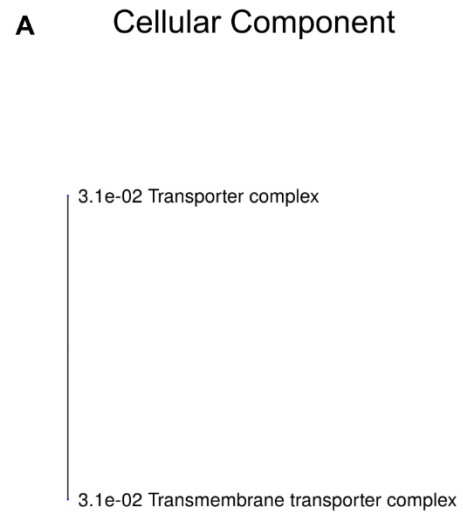

Figure 3.15. GO analysis for gambogic acid up-regulated proteins. Enrichment of GO terms and KEGG pathways for the significant differentially expressed proteins were generated as described in **Figure 3.1** and Methods. Enriched terms and *p*-values are reported. Larger blue dots indicate more significant *p*-values. Panel A: Cellular component.

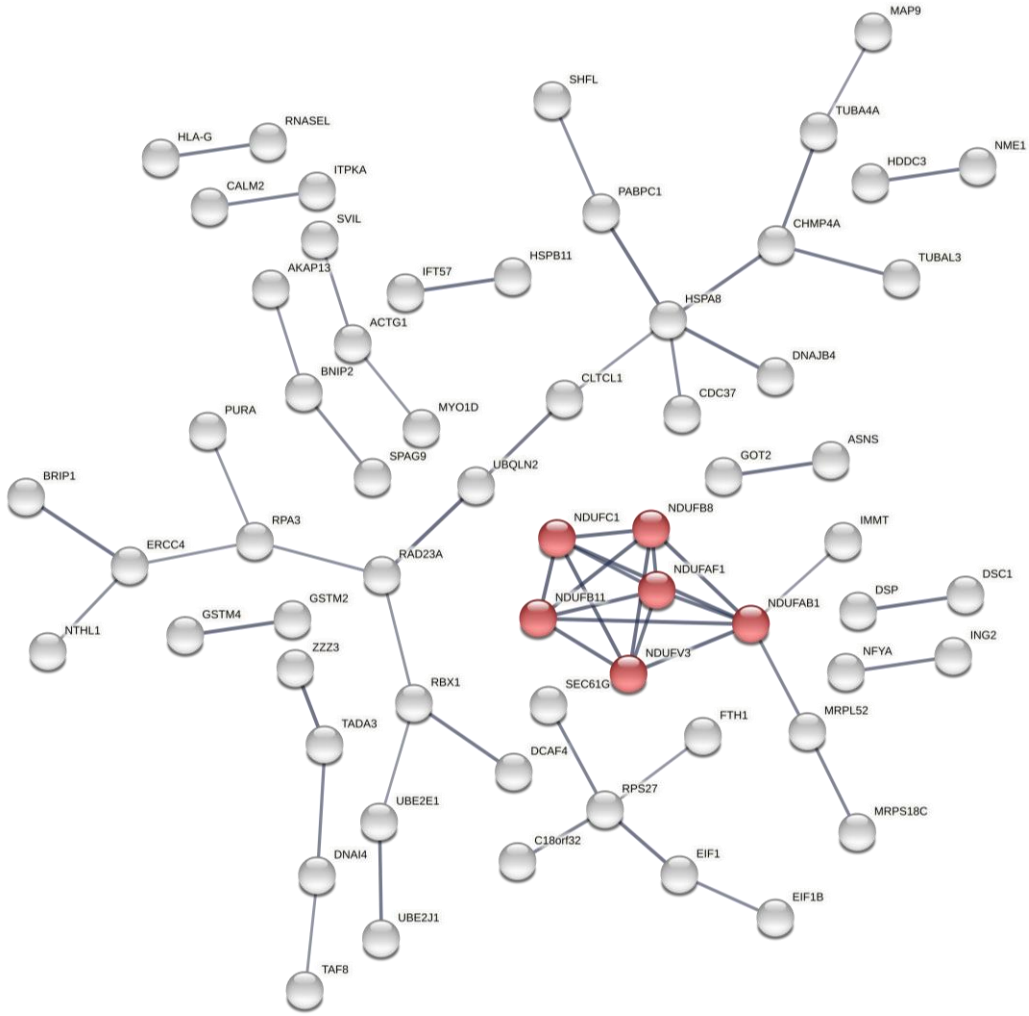

Figure 3.16. Protein-protein interaction network of gambogic acid up-regulated proteins. Protein-protein interaction network of the significant differentially expressed proteins as described in **Figure 3.4** and Methods. Protein nodes are colored based on functional enrichments: Red: GO:0005747 Mitochondrial respiratory chain complex i.

Coumermycin A1 bioinformatics analysis yielded results highly similar to clorobiocin. This was with little surprise as these compounds are structurally similar (coumarin antibiotics), and had the highest Pearson correlation of our compound panel. We observe a plethora of terms associated with the mitochondria electron transport chain (red nodes), and mitochondrial ribosome (blue nodes) down-regulated indicating antagonism of mitochondrial health (**Figure 3.17** and **Figure 3.18**). Additionally, we see terms associated with amino acid transmembrane transporters, and steroid metabolism up-regulated (**Figure 3.19** and **Figure 3.20**).

Bioinformatics analysis of differentially expressed proteins of derrubone treatement yielded a unique, and interesting set of enrichments. Down-regulated terms are dominated by fatty acid metabolism, and ubiquitin conjugation (**Figure 3.21** and **Figure 3.22**). Up-regulated terms were sparse, but comprised of serine-type peptidase, and collagen-containing extracellular matrix (**Figure 3.23** and **Figure 3.24**).

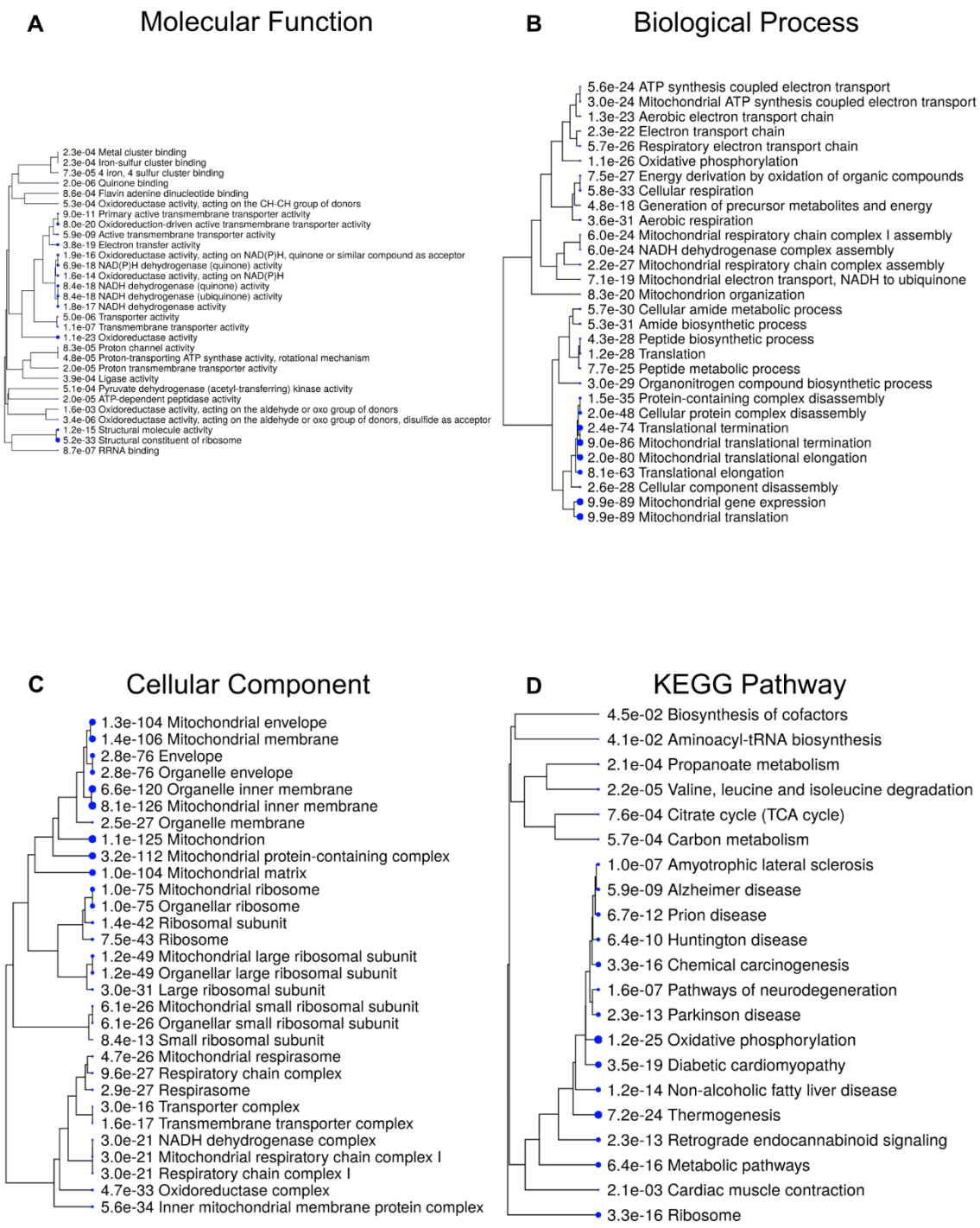

Figure 3.17. GO analysis for coumermycin A1 down-regulated proteins. Enrichment of GO terms and KEGG pathways for the significant differentially expressed proteins were generated as described in **Figure 3.1** and Methods. Enriched terms and *p*-values are reported. Larger blue dots indicate more significant *p*-values. Panel A: Molecular function. Panel B: Biological process. Panel C: Cellular component. Panel D: KEGG pathway.

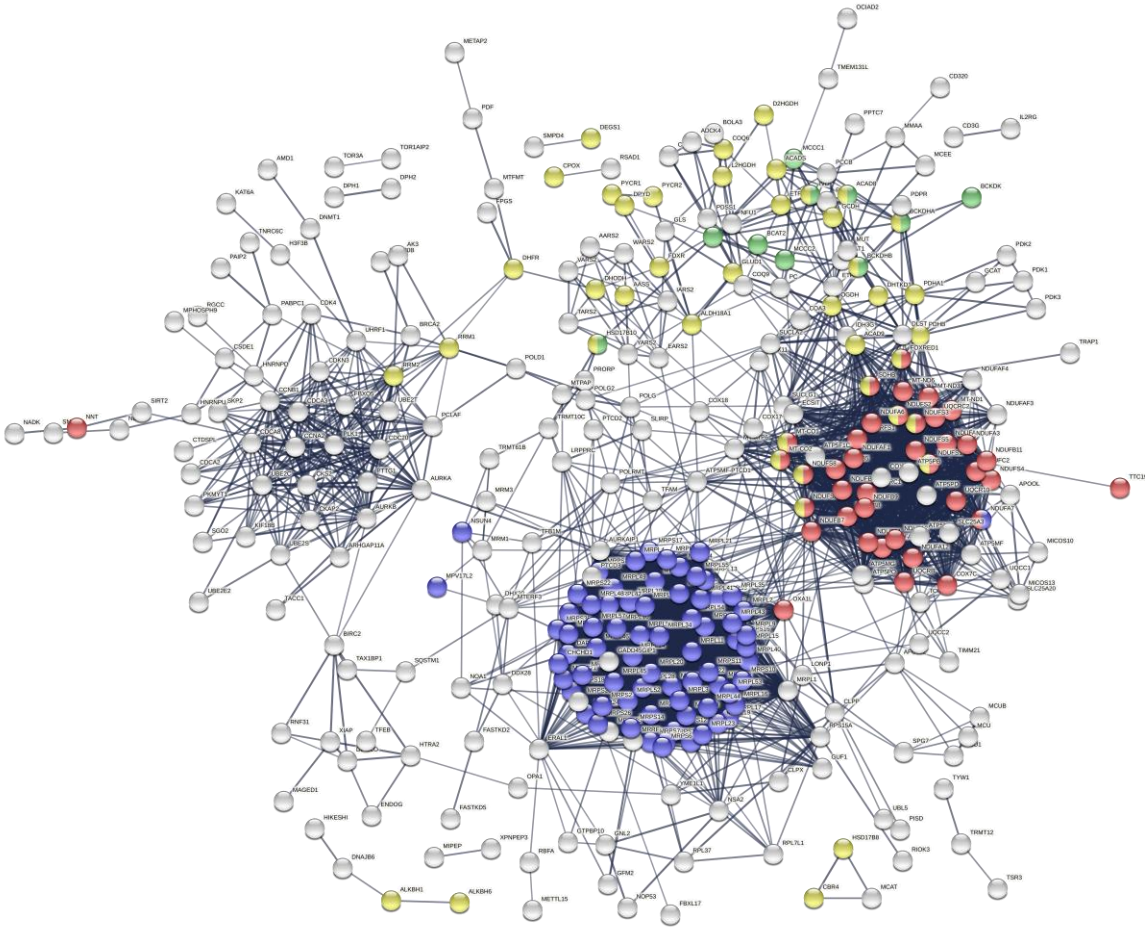

Figure 3.18. Protein-protein interaction network of coumermycin A1 down-regulated proteins. Protein-protein interaction network of the significant differentially expressed proteins as described in **Figure 3.4** and Methods. Protein nodes are colored based on functional enrichments: Red: GO:0070469 Respirasome, Blue: GO:0005761 Mitochondrial ribosome, Green: HSA-70895 Branched-chain amino acid metabolism, Yellow: KW-0560 Oxidoreductase.

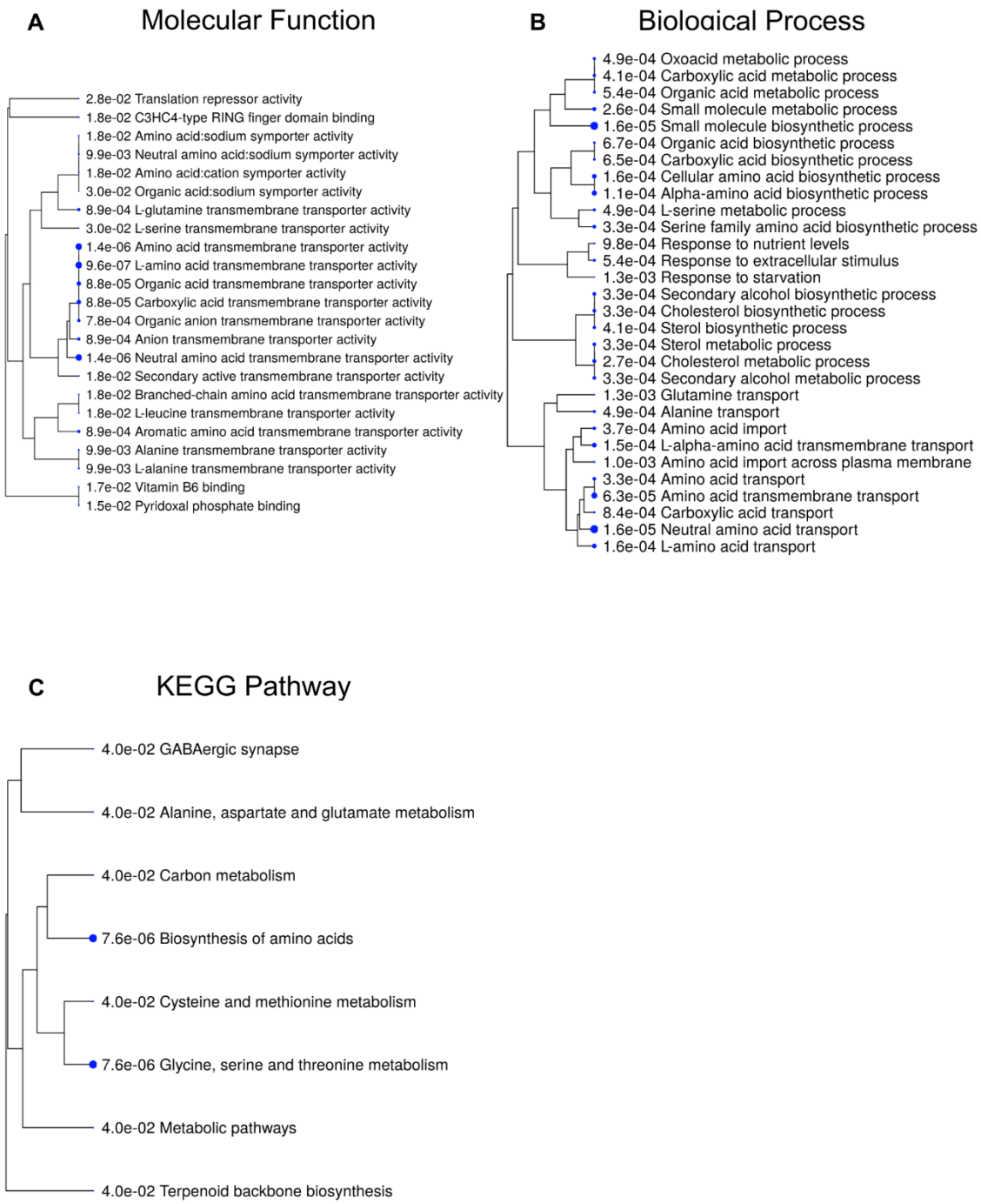

Figure 3.19. GO analysis for coumermycin A1 up-regulated proteins. Enrichment of GO terms and KEGG pathways for the significant differentially expressed proteins were generated as described in **Figure 3.1** and Methods. Enriched terms and *p*-values are reported. Larger blue dots indicate more significant *p*-values. Panel A: Molecular function. Panel B: Biological process. Panel C: KEGG pathway.

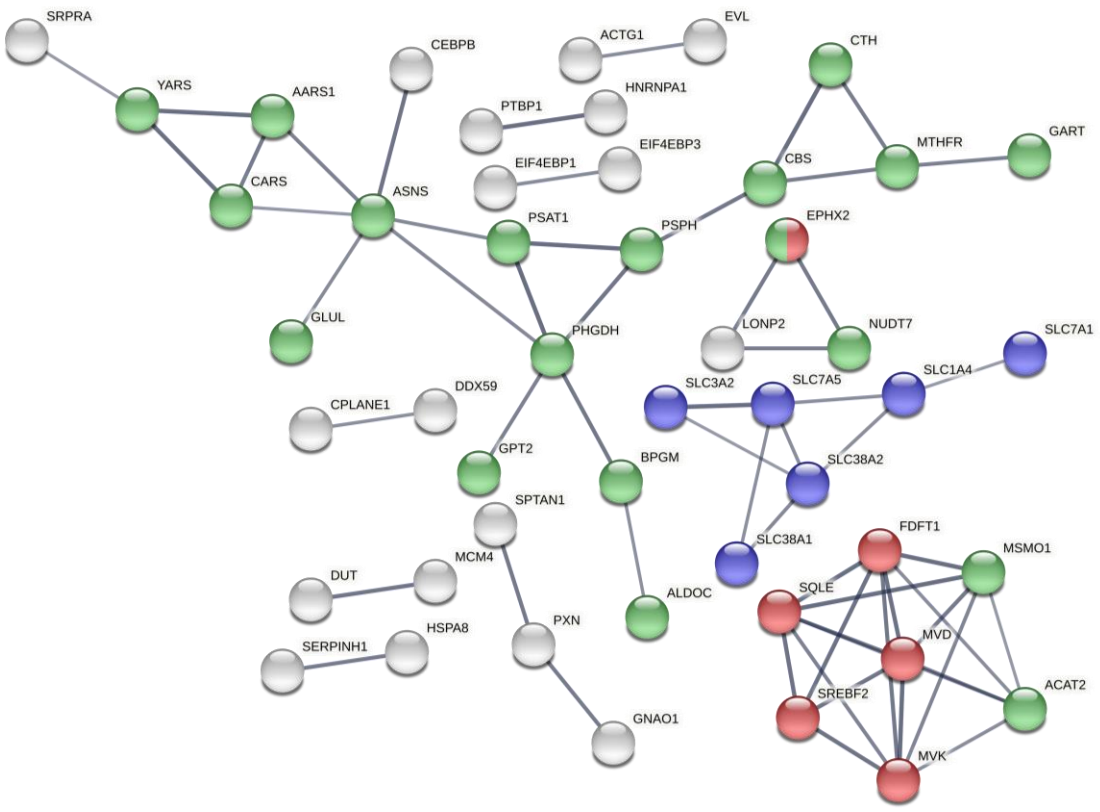

Figure 3.20. Protein-protein interaction network of coumermycin A1 up-regulated proteins. Protein-protein interaction network of the significant differentially expressed proteins as described in **Figure 3.4** and Methods. Protein nodes are colored based on functional enrichments: Red: GO:0019218 Regulation of steroid metabolic process, Blue: CL:14978 Amino acid transport across the plasma membrane, Green: GO:0019752 Carboxylic acid metabolic process.

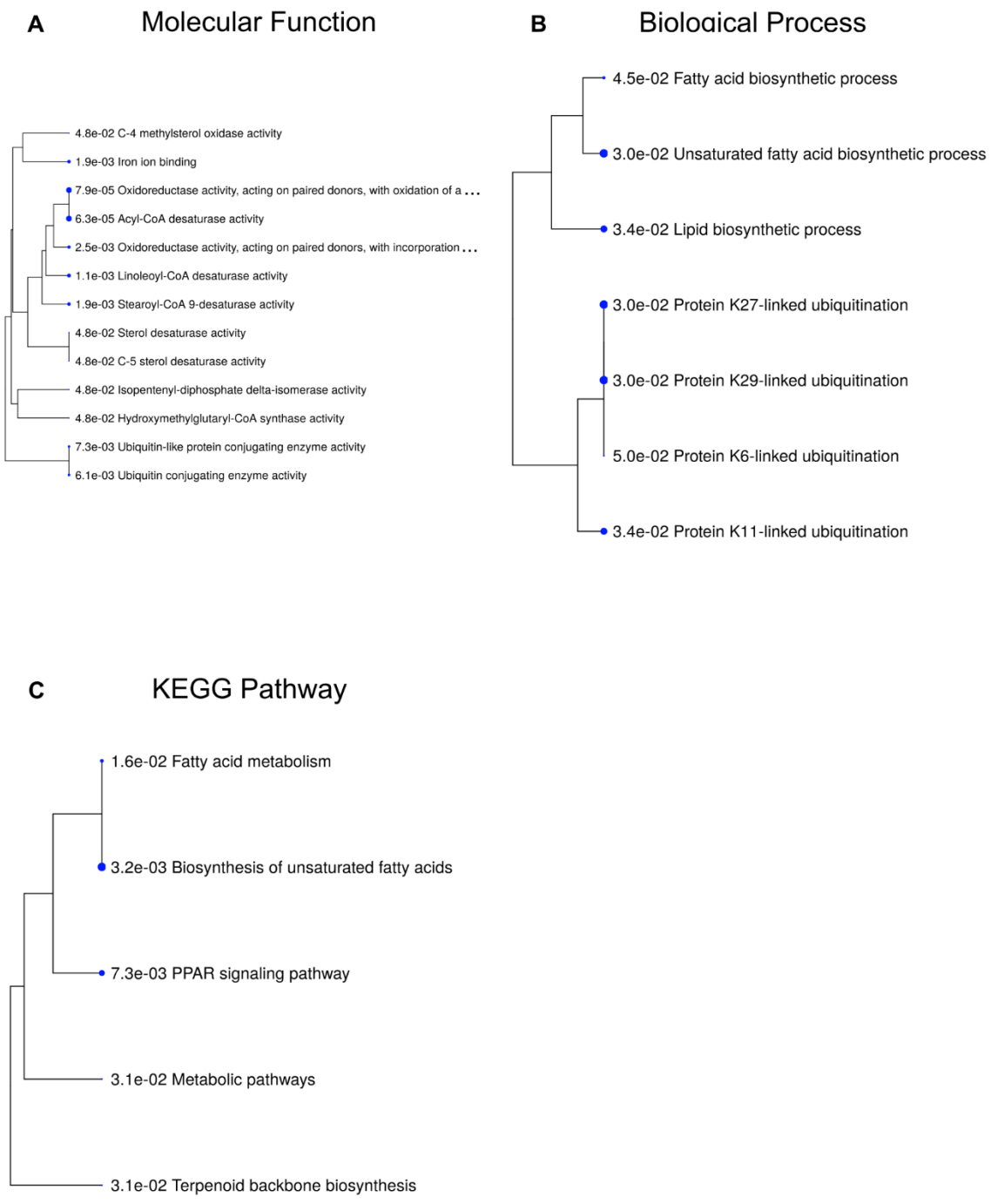

Figure 3.21. GO analysis for derrubone down-regulated proteins. Enrichment of GO terms and KEGG pathways for the significant differentially expressed proteins were generated as described in **Figure 3.1** and Methods. Enriched terms and *p*-values are reported. Larger blue dots indicate more significant *p*-values. Panel A: Molecular function. Panel B: Biological process. Panel C: KEGG pathway.

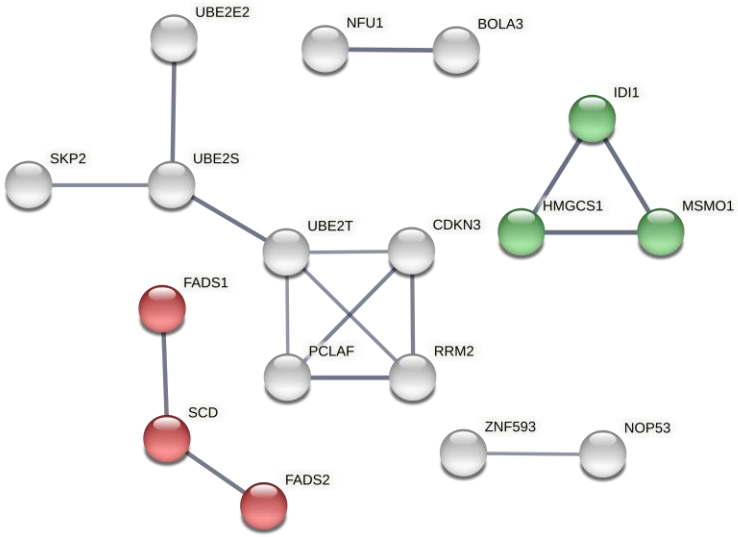

Figure 3.22. Protein-protein interaction network of derrubone down-regulated proteins. Protein-protein interaction network of the significant differentially expressed proteins as described in **Figure 3.4** and Methods. Protein nodes are colored based on functional enrichments: Red: GO:0016215 acyl-CoA desaturase activity, Green: WP197 Cholesterol biosynthesis pathway.

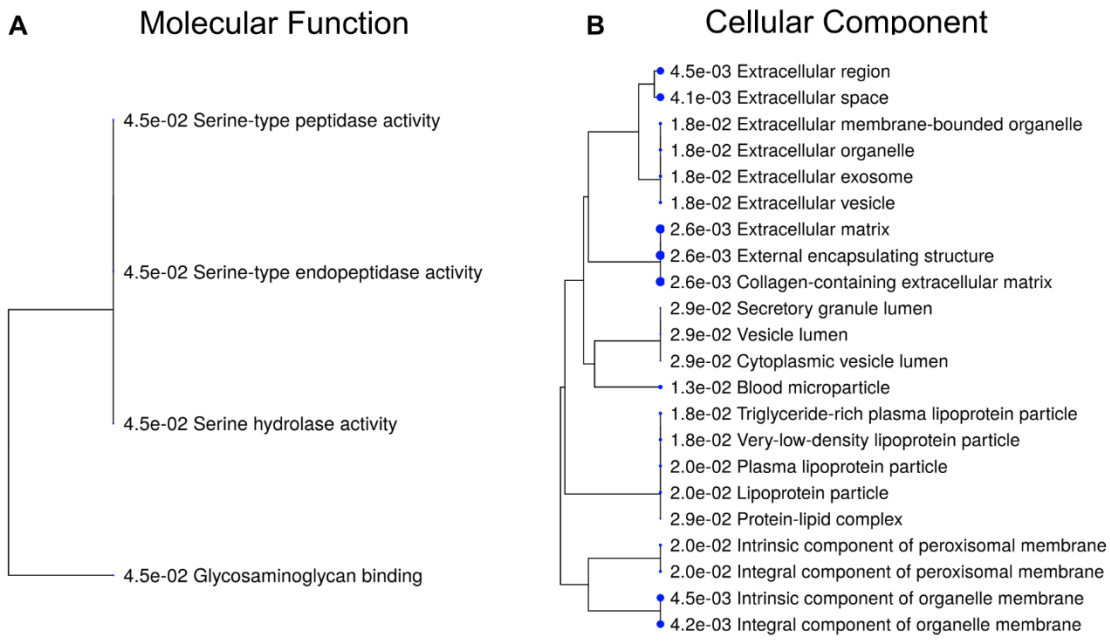

Figure 3.23. GO analysis for derrubone up-regulated proteins. Enrichment of GO terms and KEGG pathways for the significant differentially expressed proteins were generated as described in **Figure 3.1** and Methods. Enriched terms and *p*-values are reported. Larger blue dots indicate more significant *p*-values. Panel A: Molecular function. Panel B: Biological process.

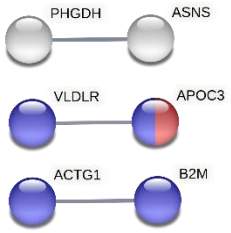

Figure 3.24. Protein-protein interaction network of derrubone up-regulated proteins. Protein-protein interaction network of the significant differentially expressed proteins as described in **Figure 3.4** and Methods. Protein nodes are colored based on functional enrichments: Red: GO:0062023 Collagen-containing extracellular matrix. Blue: GOCC:0005576 Extracellular region.

Bioinformatics analysis of differentially expressed proteins induced by garcinol treatment are similar to clorobiocin, and coumermycin A1. Again, the down-regulated enrichments are dominated by terns indicating disruption of mitochondrial health in the electron transport chain, and mitochondrial ribosomes (**Figure 3.25**). These enrichments are apparent in the protein-protein interaction network (**Figure 3.26**). These results indicate that garcinol cytotoxicity is in part attributed to disruption of mitochondrial health.

However, the similarities between garcinol, and the coumarin compounds does not carrying over into the up-regulated analysis. Here, garcinol treatment has enriched terms that indicate that garcinol is a prolific antagonist of proteostasis in the endoplasmic reticulum (**Figure 3.27** and **Figure 3.28**). Two of the most important enriched terms to acknowledge are IRE1-mediated unfolded protein response, and ERAD (endoplasmic reticulum associated degradation) pathway (**Figure 3.27 Panel B**). These pathways are part of the unfolded protein response reviewed in Chapter 1 and indicate that a major part of garcinol cytotoxicity is proteostasis perturbation in the endoplasmic reticulum.

Figure 3.25. GO analysis for garcinol down-regulated proteins. Enrichment of GO terms and KEGG pathways for the significant differentially expressed proteins were generated as described in **Figure 3.1** and Methods. Enriched terms and *p*-values are reported. Larger blue dots indicate more significant *p*-values. Panel A: Molecular function. Panel B: Biological process. Panel C: Cellular component. Panel D: KEGG pathway.

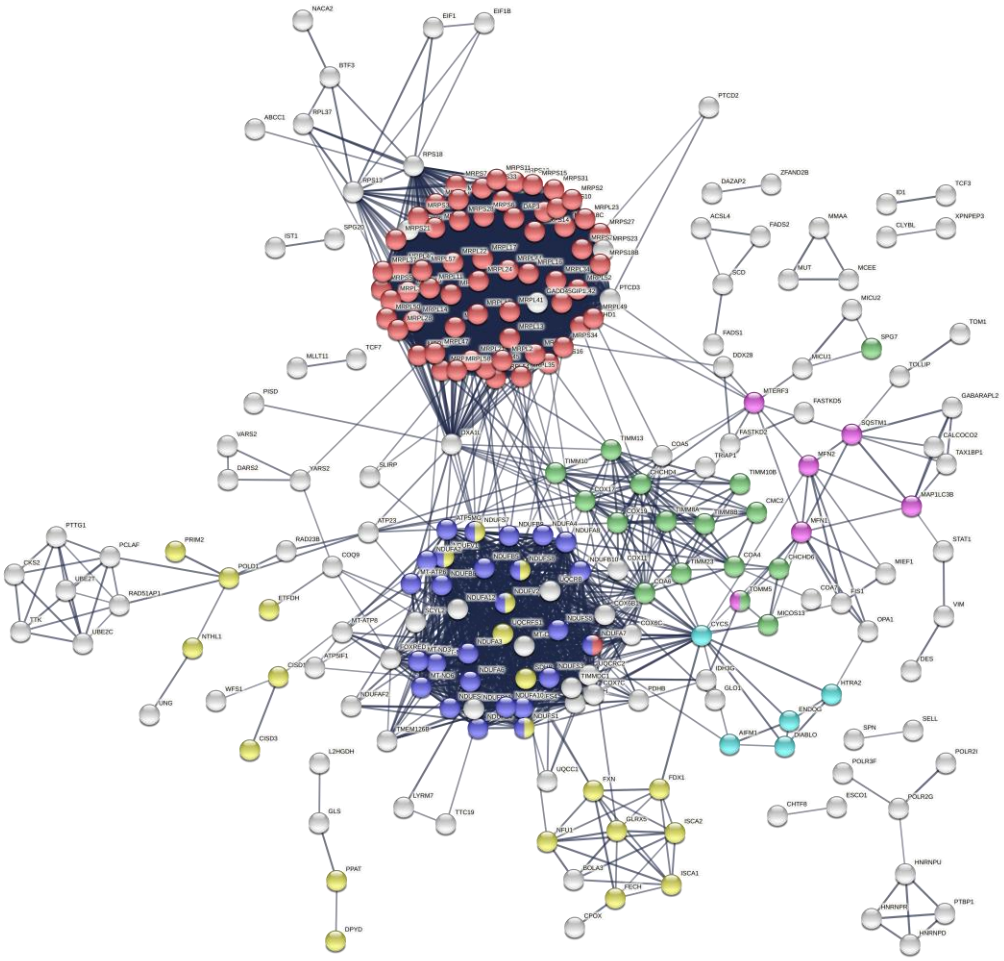

Figure 3.26. Protein-protein interaction network of garcinol down-regulated proteins. Protein-protein interaction network of the significant differentially expressed proteins as described in **Figure 3.4** and Methods. Protein nodes are colored based on functional enrichments: Red: GO:0005761 Mitochondrial ribosome, Blue: WP623 Oxidative phosphorylation, Green: CL:13621 Mitochondrial protein import, and SAM complex, Yellow: GO:0051536 Iron-sulfur cluster binding, Cyan: CL:18765 SMAC (DIABLO) binds to LAPS, and cellular response to aldosterone, Pink: HSA-5205685 Pink-1-PRKN mediated mitophagy.

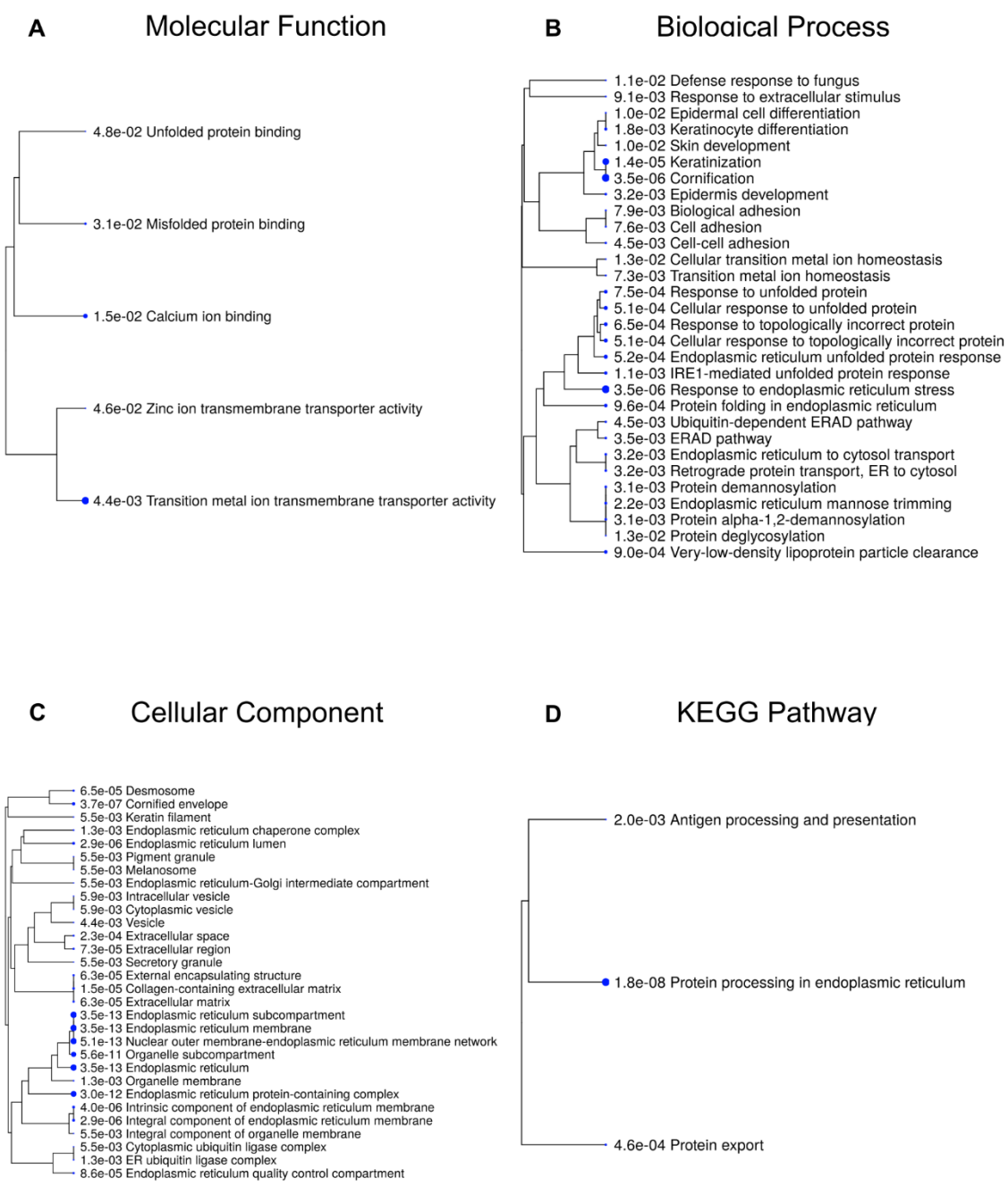

Figure 3.27. GO analysis for garcinol up-regulated proteins. Enrichment of GO terms and KEGG pathways for the significant differentially expressed proteins were generated as described in **Figure 3.1** and Methods. Enriched terms and *p*-values are reported. Larger blue dots indicate more significant *p*-values. Panel A: Molecular function. Panel B: Biological process. Panel C: Cellular component. Panel D: KEGG pathway.

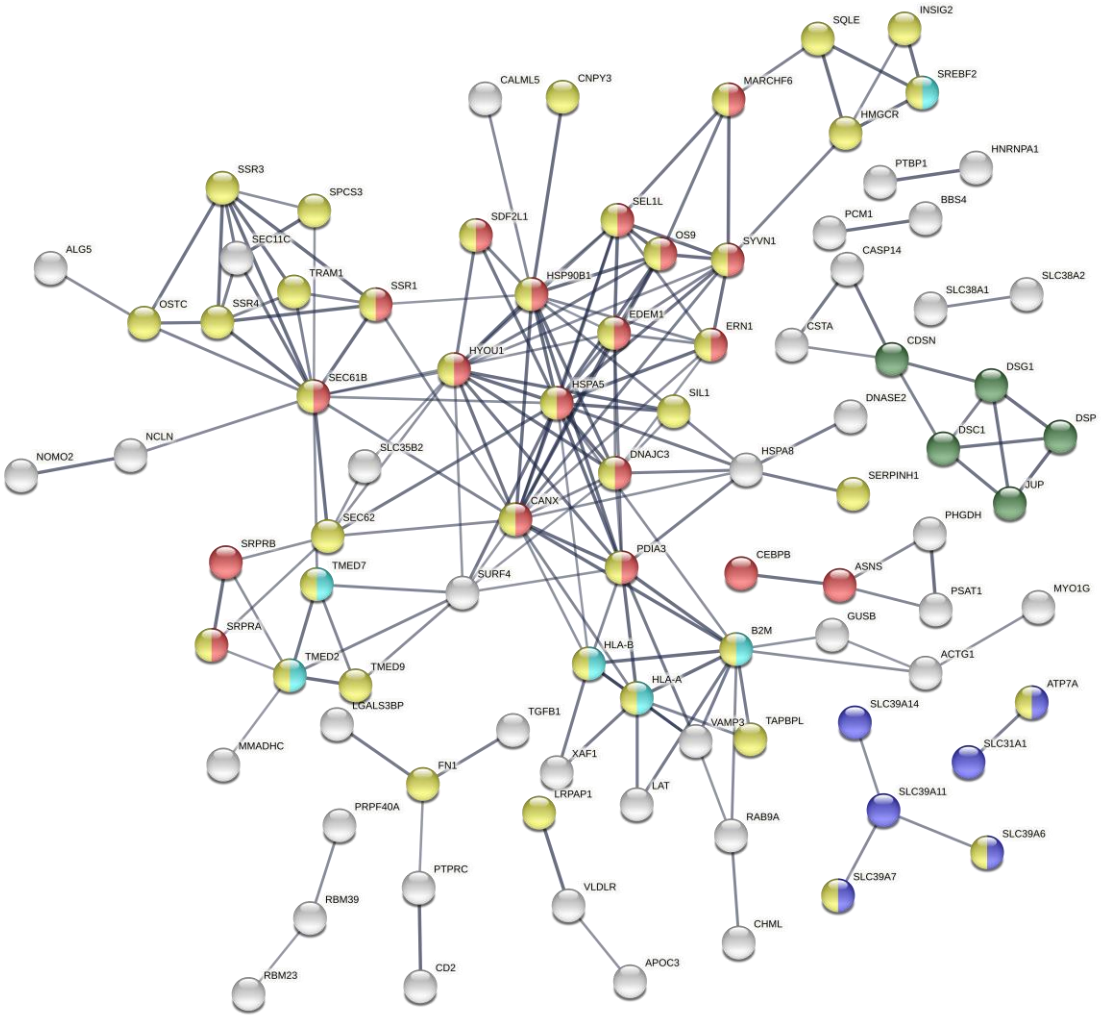

Figure 3.28. Protein-protein interaction network of garcinol up-regulated proteins. Protein-protein interaction network of the significant differentially expressed proteins as described in **Figure 3.4** and Methods. Protein nodes are colored based on functional enrichments: Red: GO:0034976 Response to endoplasmic reticulum stress, Blue: GO:0046915 Transition metal ion transmembrane transporter activity, Dark Green: GO:0030057 Desmosome, Yellow: GO:0005783 Endoplasmic reticulum, Cyan: GO:0012507 ER to Golgi transport vesicle membrane.

Bioinformatics analysis of daurisoline treatment show a down-regulation of proteins associated with ribosome biogenesis, and nucleotide catabolic processes (**Figure 3.29** and **Figure 3.30**). Enriched pathways for the up-regulated proteins include a variety of transmembrane transporters, secondary alcohol, lipid, sterol, steroid, and cholesterol metabolic processes (**Figure 3.3**1 and **Figure 3.32**). Additionally, we see a handful of terms for the endoplasmic reticulum membrane, sub-compartment, and calcium binding. The endoplasmic reticulum plays crucial roles in lipid biosynthesis, and calcium storage [122].

Bioinformatics analysis of the differentially expressed proteins induced by β-lapachone treatment are familiar to many of the other drugs in our panel. Again, we observe that the mitochondrial electron transport chain, and mitochondrial ribosomes are down-regulated (**Figure 3.33** and **Figure 3.34**). Additionally, we see enrichment of negative regulation of the metaphase to anaphase transition that was also enriched in ailanthone. Furthermore, analysis of the up-regulated proteins by β-lapachone treatment is heavily dominated by terms for amino acid transport (**Figure 3.35**). Sprinkled in amongst the transporter terms are a handful of terms associated with the endoplasmic reticulum chaperone complex indicating proteostasis perturbation of the ER (**Figure 3.35** and **Figure 3.36**). These results indicate that β-lapachone cytotoxicity is in part disruption of the mitochondrial matrix, and to a lesser extent perturbation of proteostasis in the endoplasmic reticulum.

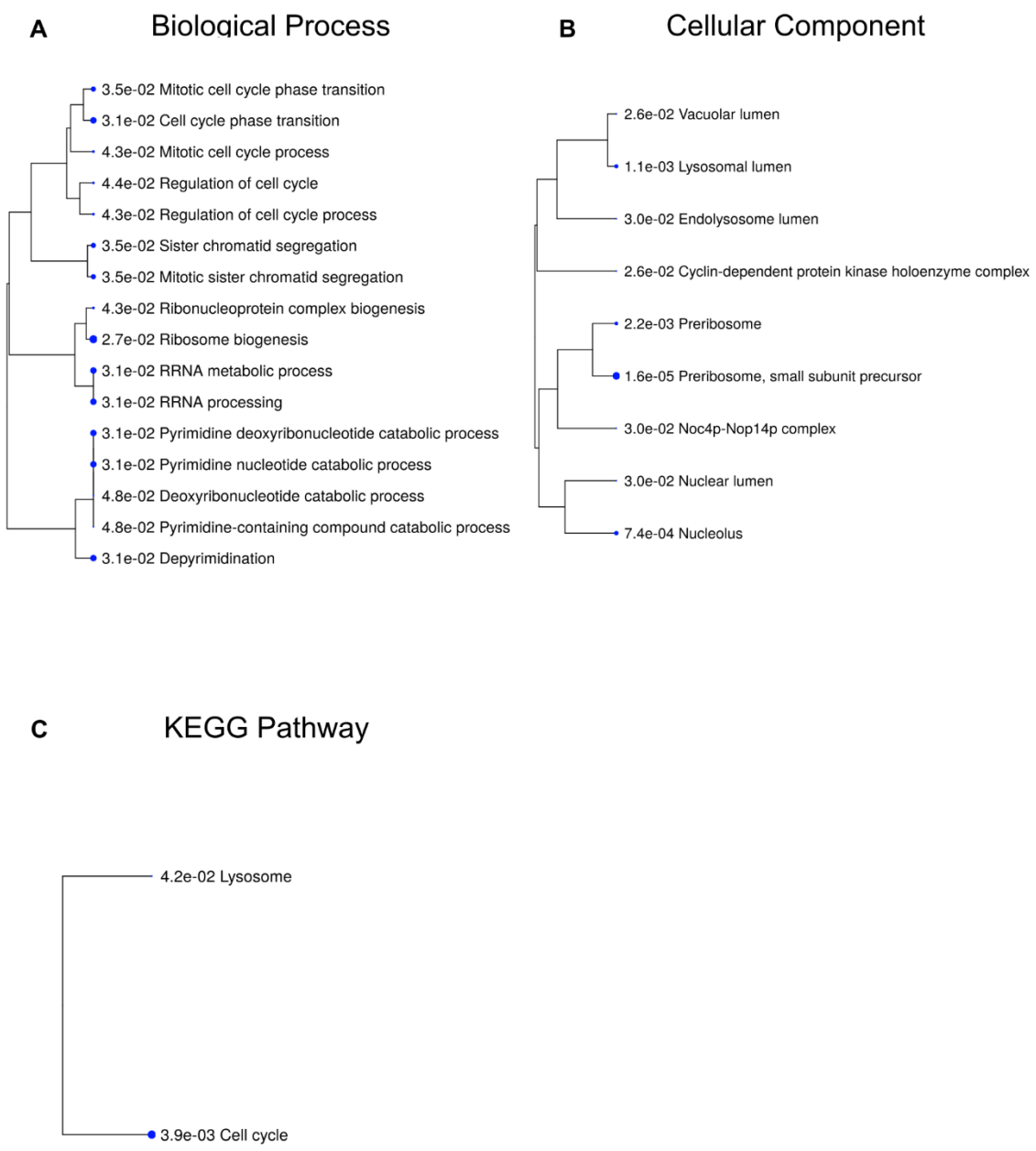

Figure 3.29. GO analysis for daurisoline down-regulated proteins. Enrichment of GO terms and KEGG pathways for the significant differentially expressed proteins were generated as described in **Figure 3.1** and Methods. Enriched terms and *p*-values are reported. Larger blue dots indicate more significant *p*-values. Panel A: Biological process. Panel B: Cellular component. Panel C: KEGG pathway.

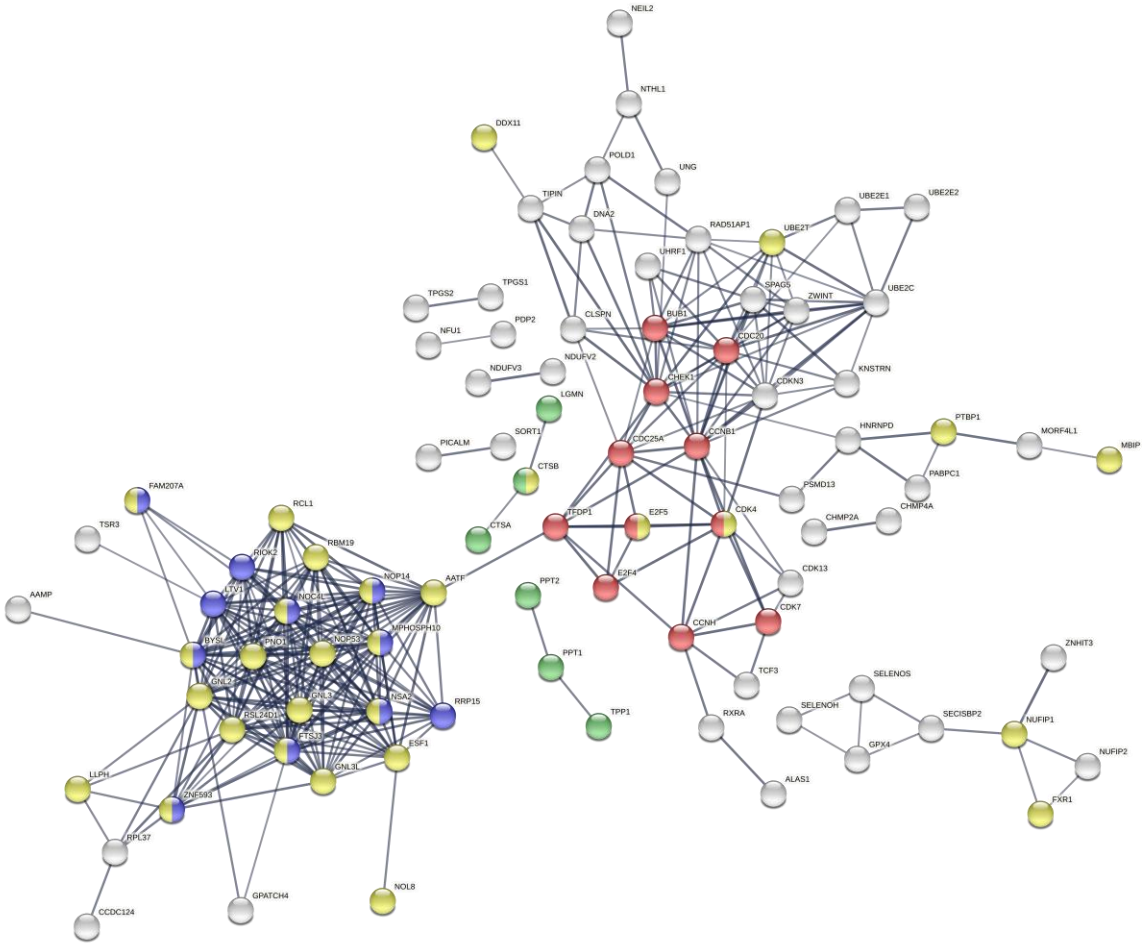

Figure 3.30. Protein-protein interaction network of daurisoline down-regulated proteins. Protein-protein interaction network of the significant differentially expressed proteins as described in **Figure 3.4** and Methods. Protein nodes are colored based on functional enrichments: Red: WP179 Cell cycle, Blue: GO:0030684 Preribosome, Green: GOCC:0043202 Lysosomal lumen, Yellow: GO:0005730 Nucleolus.

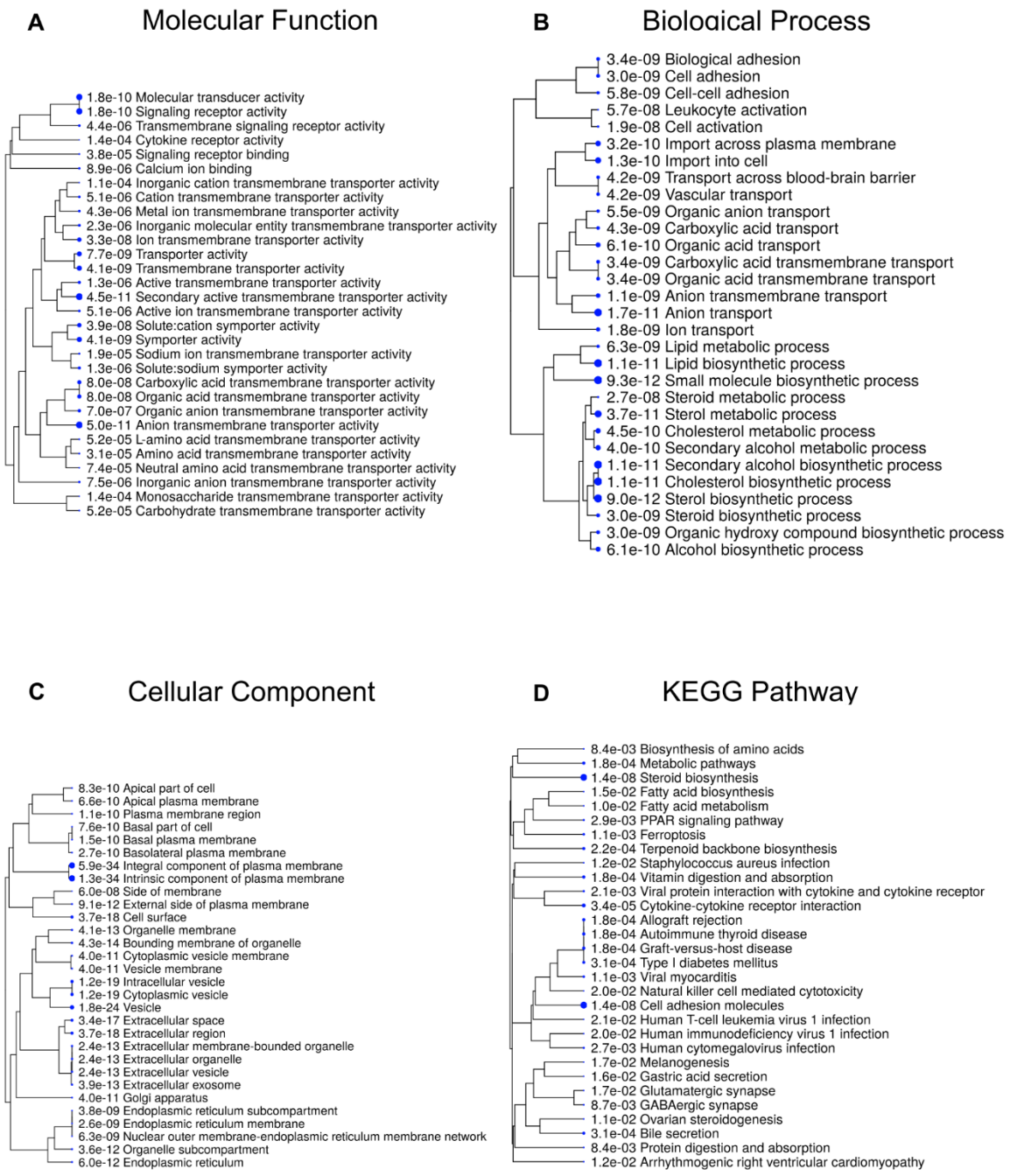

Figure 3.31. GO analysis for daurisoline up-regulated proteins. Enrichment of GO terms and KEGG pathways for the significant differentially expressed proteins were generated as described in **Figure 3.1** and Methods. Enriched terms and *p*-values are reported. Larger blue dots indicate more significant *p*-values. Panel A: Molecular function. Panel B: Biological process. Panel C: Cellular component. Panel D: KEGG pathway.

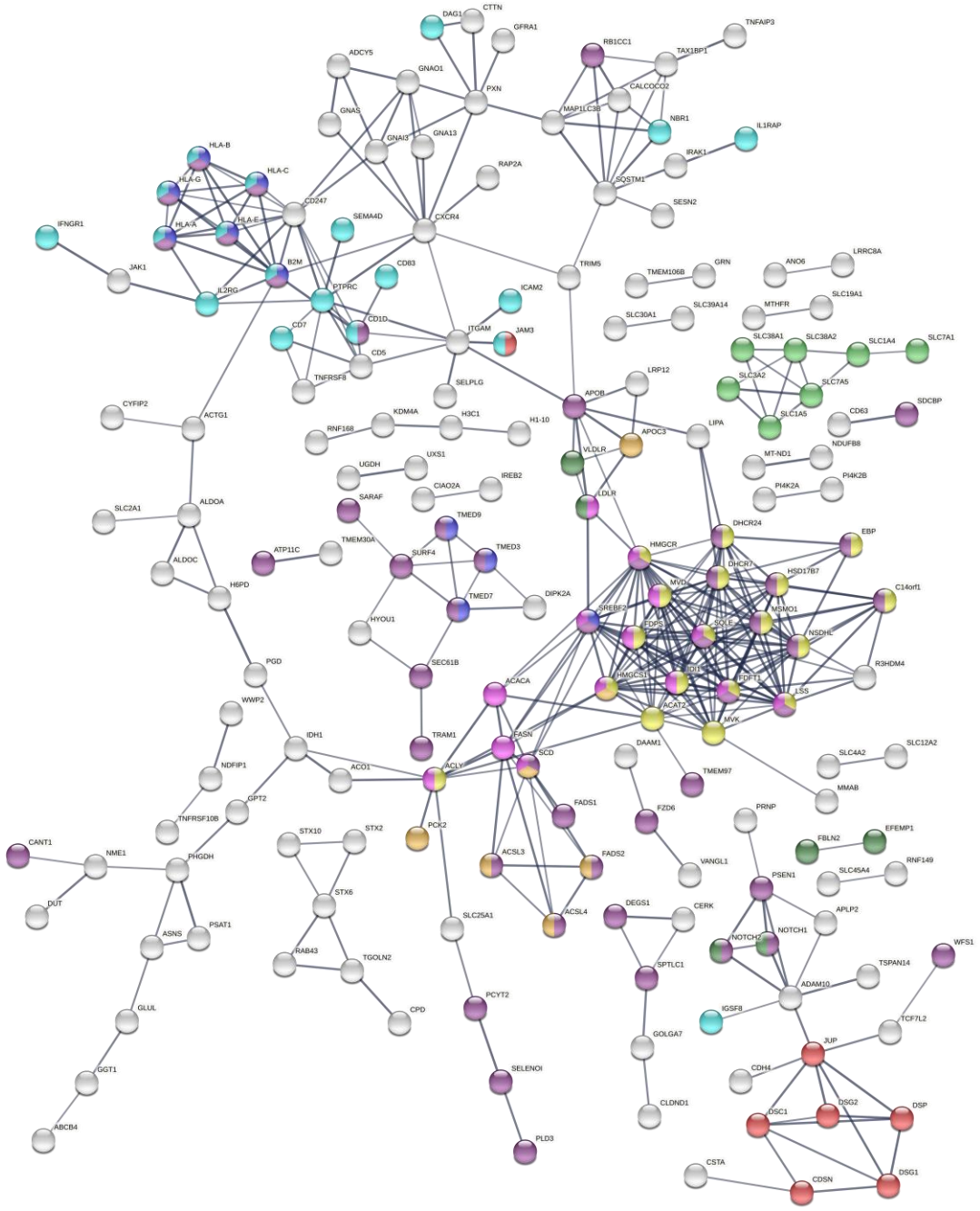

Figure 3.32. Protein-protein interaction network of daurisoline up-regulated proteins. Protein-protein interaction network of the significant differentially expressed proteins as described in **Figure 3.4** and Methods. Protein nodes are colored based on functional enrichments: Red: GO:0030057 Desmosome, Blue: GO:0030134 COPII-coated ER to Golgi transport vesicle, Green: HSA-352230 Amino acid transport across the plasma membrane, Yellow: GO:0016126 Sterol biosynthesis, Dark Green: IPR000742 EGF-like domain, Cyan: IPR013783 Immunoglobulin-like fold, Pink: WP1982 Sterol regulatory element-binding (SREBP) signaling, Purple: GO:0042175 Nuclear outer membrane-endopasmic reticulum membrane network, Orange: hsa03320 PPAR signaling pathway.

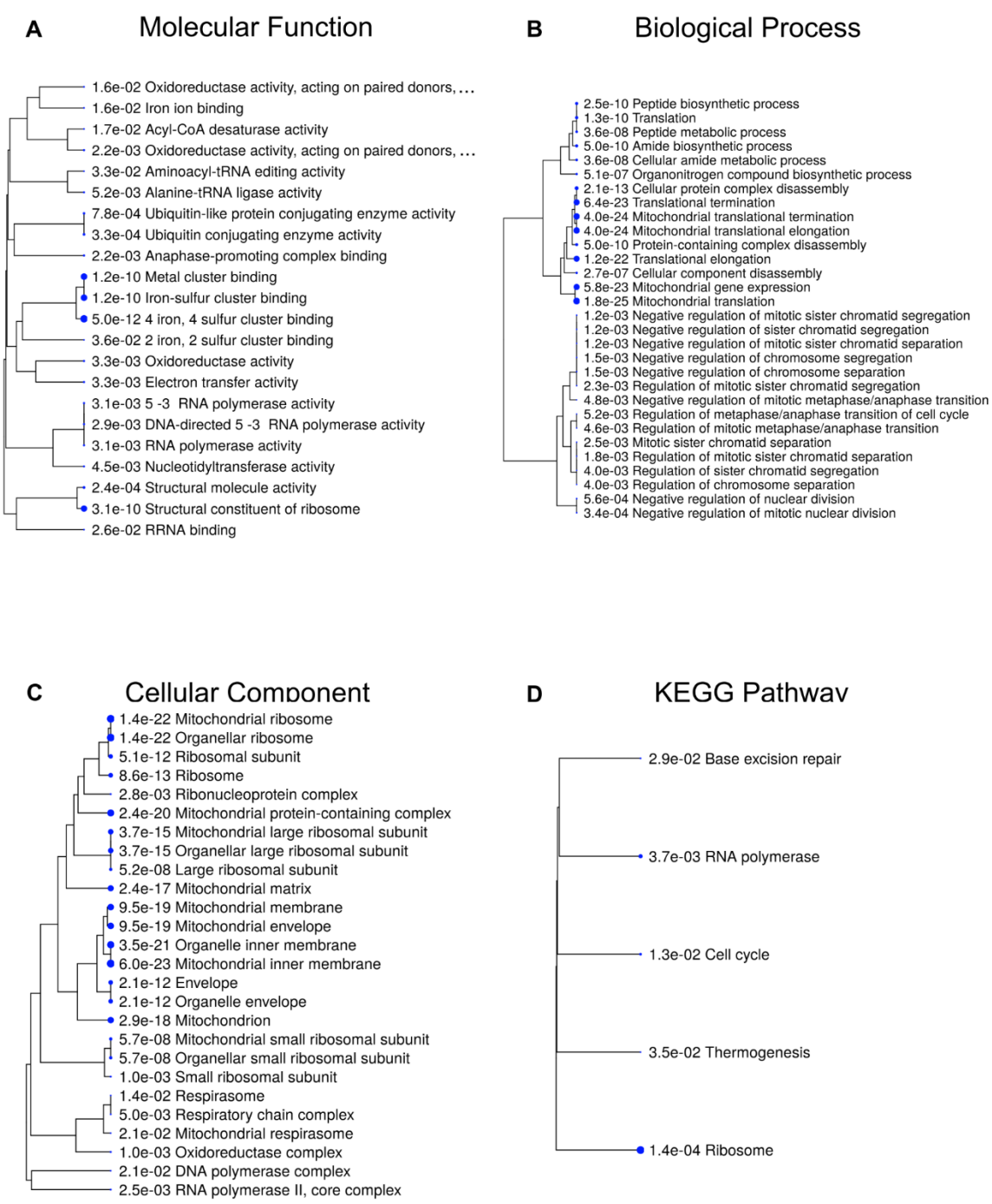

Figure 3.33. GO analysis for β-lapachone down-regulated proteins. Enrichment of GO terms and KEGG pathways for the significant differentially expressed proteins were generated as described in **Figure 3.1** and Methods. Enriched terms and *p*-values are reported. Larger blue dots indicate more significant *p*-values. Panel A: Molecular function. Panel B: Biological process. Panel C: Cellular component. Panel D: KEGG pathway.

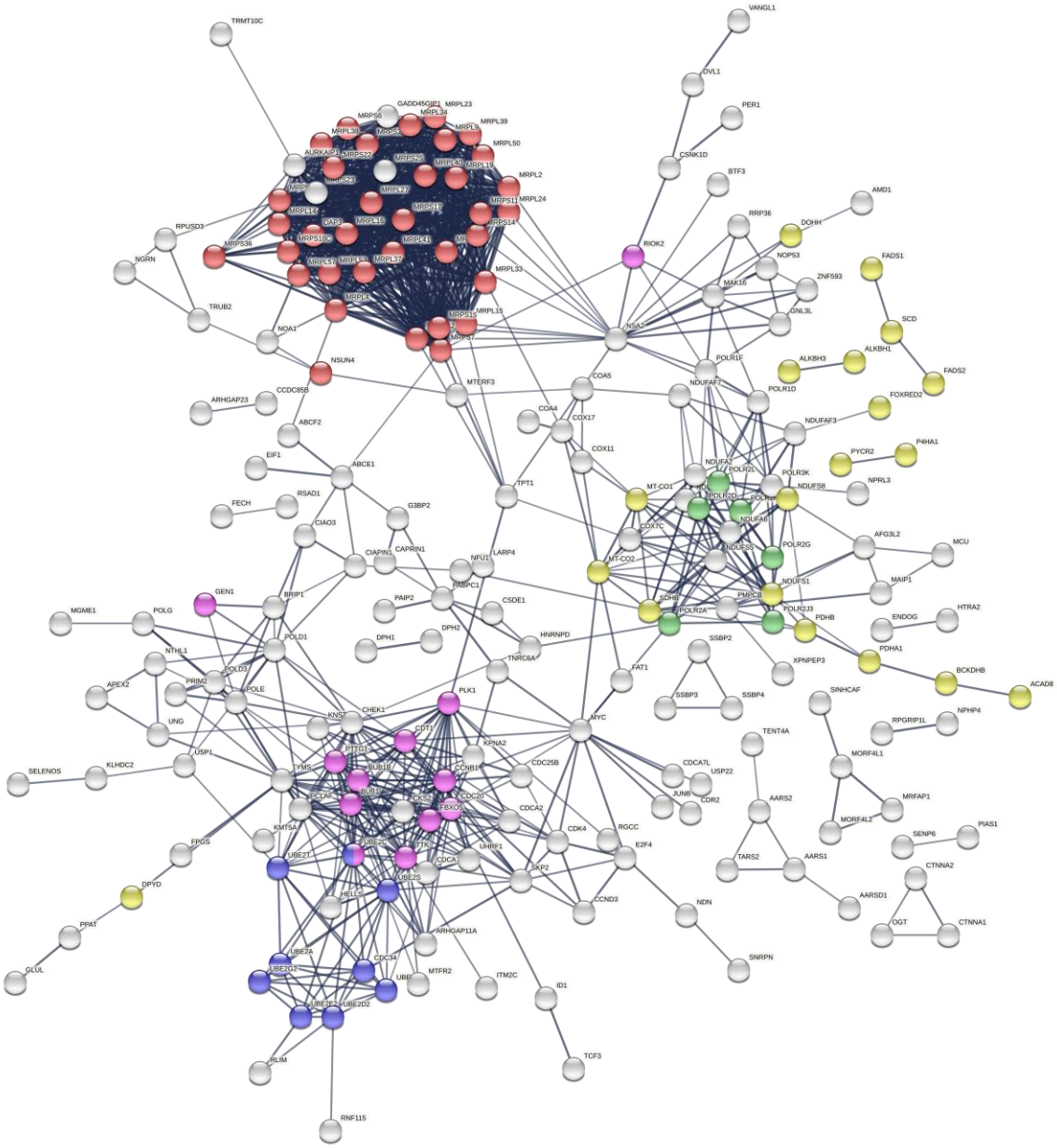

Figure 3.34. Protein-protein interaction network of β-lapachone down-regulated proteins. Protein-protein interaction network of the significant differentially expressed proteins as described in **Figure 3.4** and Methods. Protein nodes are colored based on functional enrichments: Red: GO:0005761 Mitochondrial ribosome, Blue: GO:0061631 Ubiquitin conjugating enzyme activity, Green: GO:0005665 RNA polymerase II, core complex, Yellow: KW-0560 Oxidoreductase, Pink: GO:0010965 Regulation of mitotic sister chromatid separation.

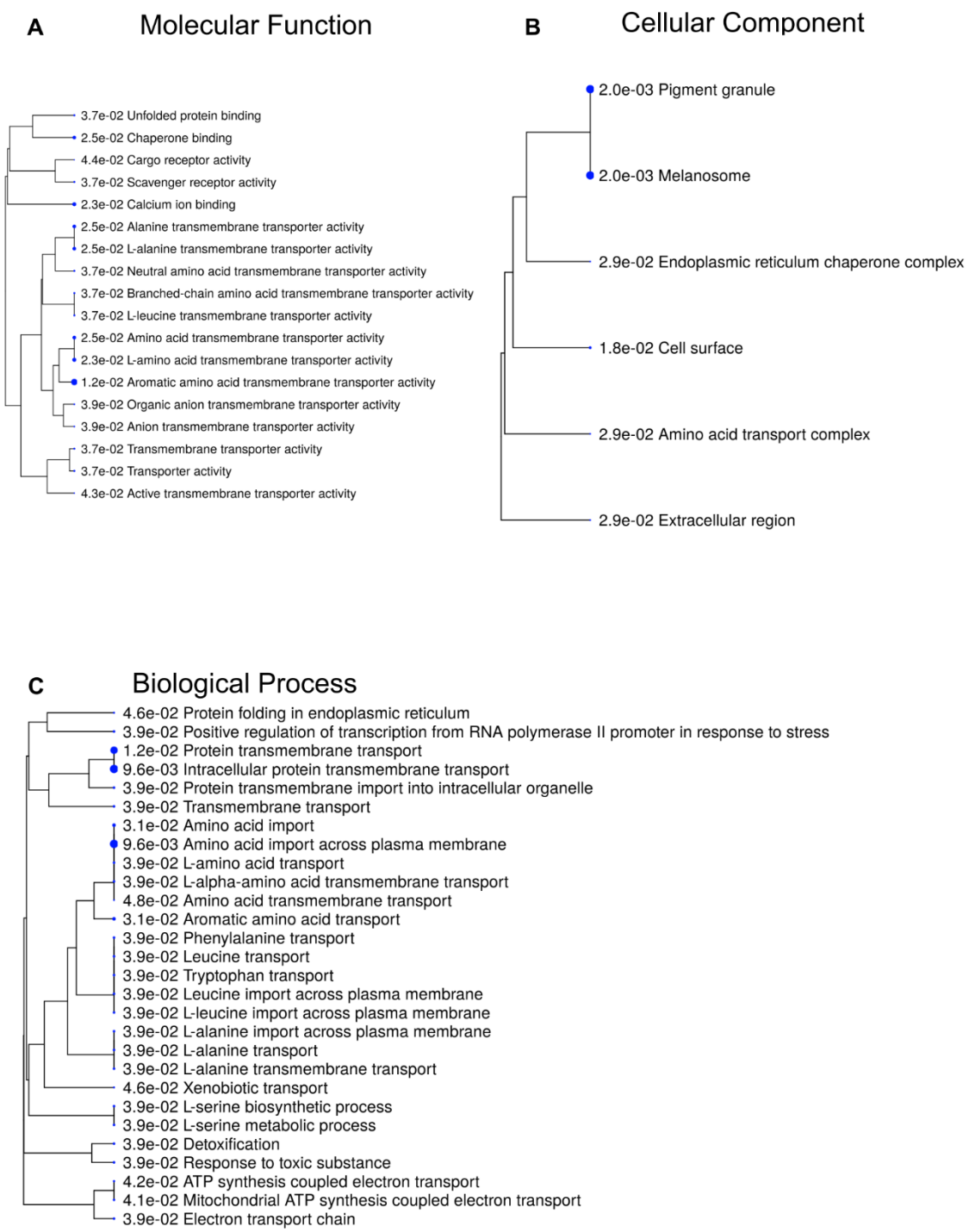

Figure 3.35. GO analysis for β-lapachone up-regulated proteins. Enrichment of GO terms and KEGG pathways for the significant differentially expressed proteins were generated as described in **Figure 3.1** and Methods. Enriched terms and *p*-values are reported. Larger blue dots indicate more significant *p*-values. Panel A: Molecular function. Panel B: Biological process. Panel C: Cellular component.

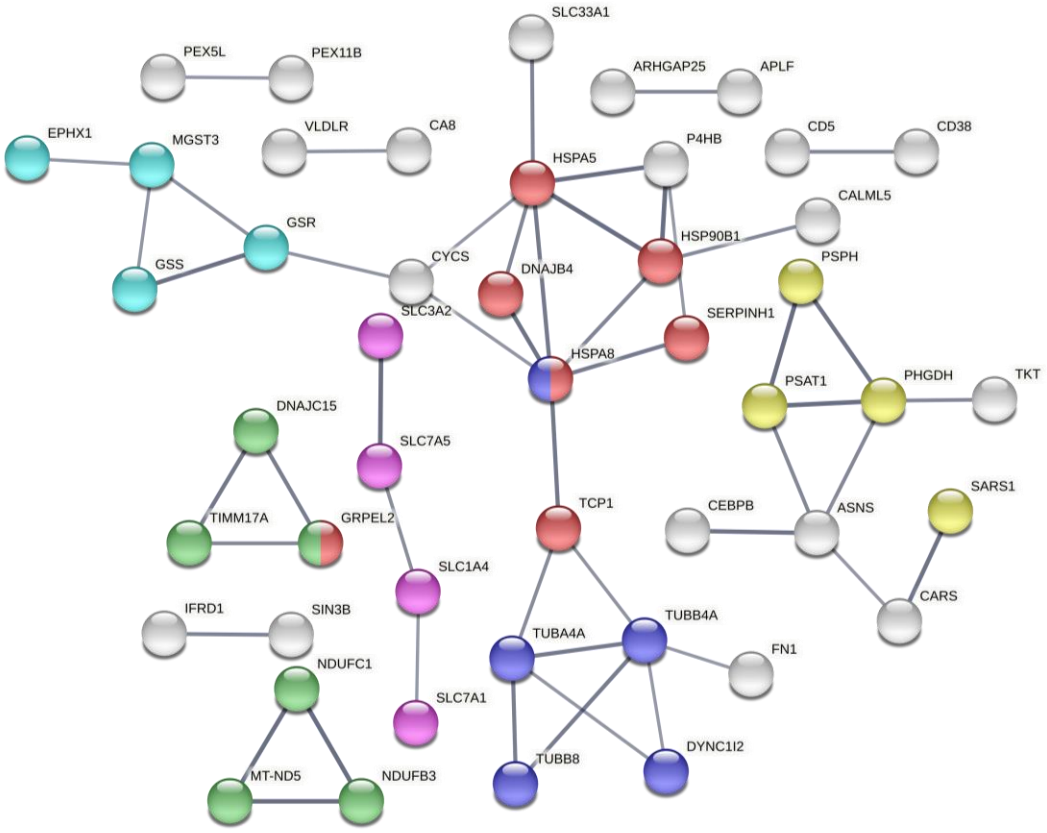

Figure 3.36. Protein-protein interaction network of β-lapachone up-regulated proteins. Protein-protein interaction network of the significant differentially expressed proteins as described in **Figure 3.4** and Methods. Protein nodes are colored based on functional enrichments: Red: GO:0051082 Unfolded protein binding, Blue: HSA-3371497 Hsp90 chaperone cycle for steroid hormone receptors (SHR), Green: GO:0098800 Inner mitochondrial membrane protein complex, Yellow: GO:0009069 Serine family amino acid metabolic process, Pink: GO:0089718 Amino acid import across plasma membrane, Cyan: CL:13064 Glutathione conjugation, and glutathione peroxidase active site.

Bioinformatics analysis of the down-regulated proteins induced by α-mangostin treatment yet again enriched the mitochondrial electron transport chain, and the mitochondrial ribosome (**Figure 3.37** and **Figure 3.38**). Terms for the electron transport chain are highly centralized on complex I, NADH dehydrogenase (ubiquinone). Enriched terms for the up-regulated proteins induced by α-mangostin treatment are sparse and entirely related to lipoproteins to the extracellular matrix (**Figure 3.39** and **Figure 3.40**). These results also indicate that disruption of mitochondrial health is a part of α-mangostin cytotoxicity.

The reoccurring enrichment of the mitochondrial electron transport chain, and mitochondrial ribosome for multiple compounds in our panel encouraged further investigation. Therefore, we generated gene lists for the mitochondrial ribosome, and each complex of the electron transport chain. Using these gene lists we curated heat maps from our proteomics data for comparative analysis. We see apparent down regulation of mitochondrial ribosome proteins for each of the compounds that enriched GO terms: celastrol, clorobiocin, coumermycin A1, garcinol, β-lapachone, and α-mangostin (**Figure 3.41**). These perturbations are not conserved in our AUY922 data.

Similarly, we see apparent down regulation of mitochondrial electron transport chain proteins for compounds that enriched related GO terms: ailanthone, clorobiocin, coumermycin A1, garcinol, β-lapachone, and α-mangostin (**Figure 3.42**). Again, when compare these perturbations to AUY922, we see they are not conserved.

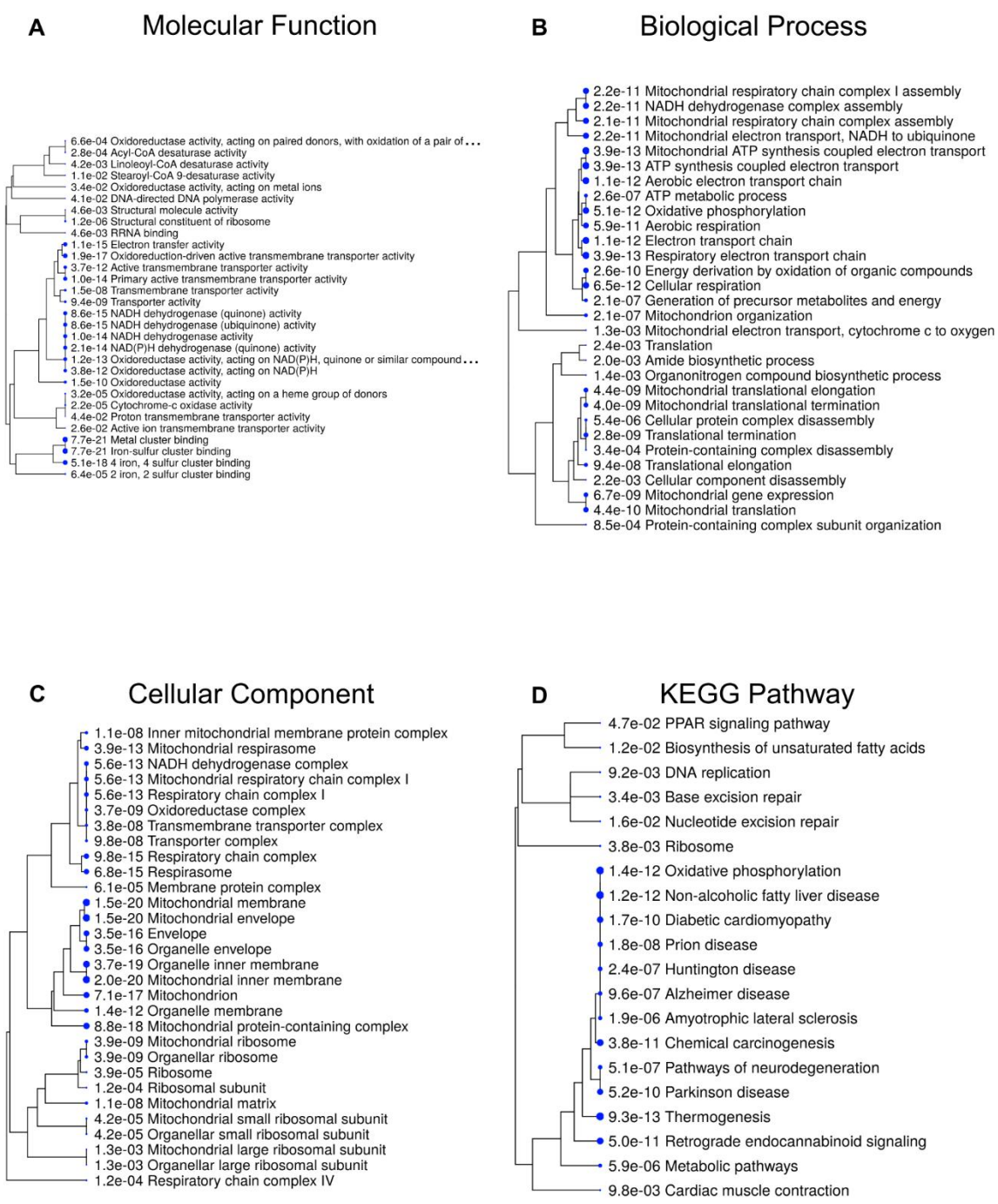

Figure 3.37. GO analysis for α-mangostin down-regulated proteins. Enrichment of GO terms and KEGG pathways for the significant differentially expressed proteins were generated as described in **Figure 3.1** and Methods. Enriched terms and *p*-values are reported. Larger blue dots indicate more significant *p*-values. Panel A: Molecular function. Panel B: Biological process. Panel C: Cellular component. Panel D: KEGG pathway.

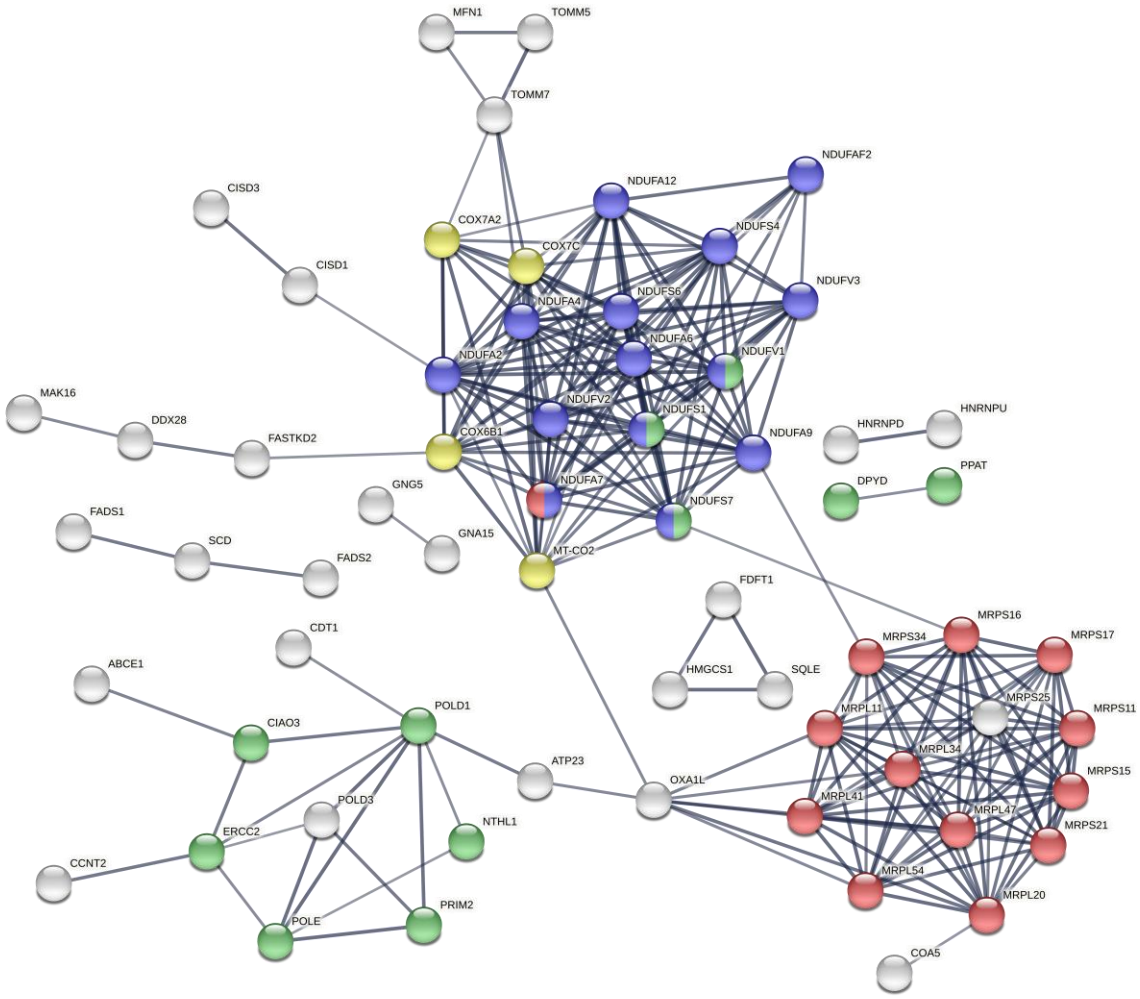

Figure 3.38. Protein-protein interaction network of α-mangostin down-regulated proteins. Protein-protein interaction network of the significant differentially expressed proteins as described in **Figure 3.4** and Methods. Protein nodes are colored based on functional enrichments: Red: GO:0005761 Mitochondrial ribosome, Blue: GO:0008137 NADH dehydrogenase (ubiquinone) activity, Green: GO:0051539 4 iron, 4 sulfur cluster binding, Yellow: GO:0004129 Cytochrome-c oxidase activity.

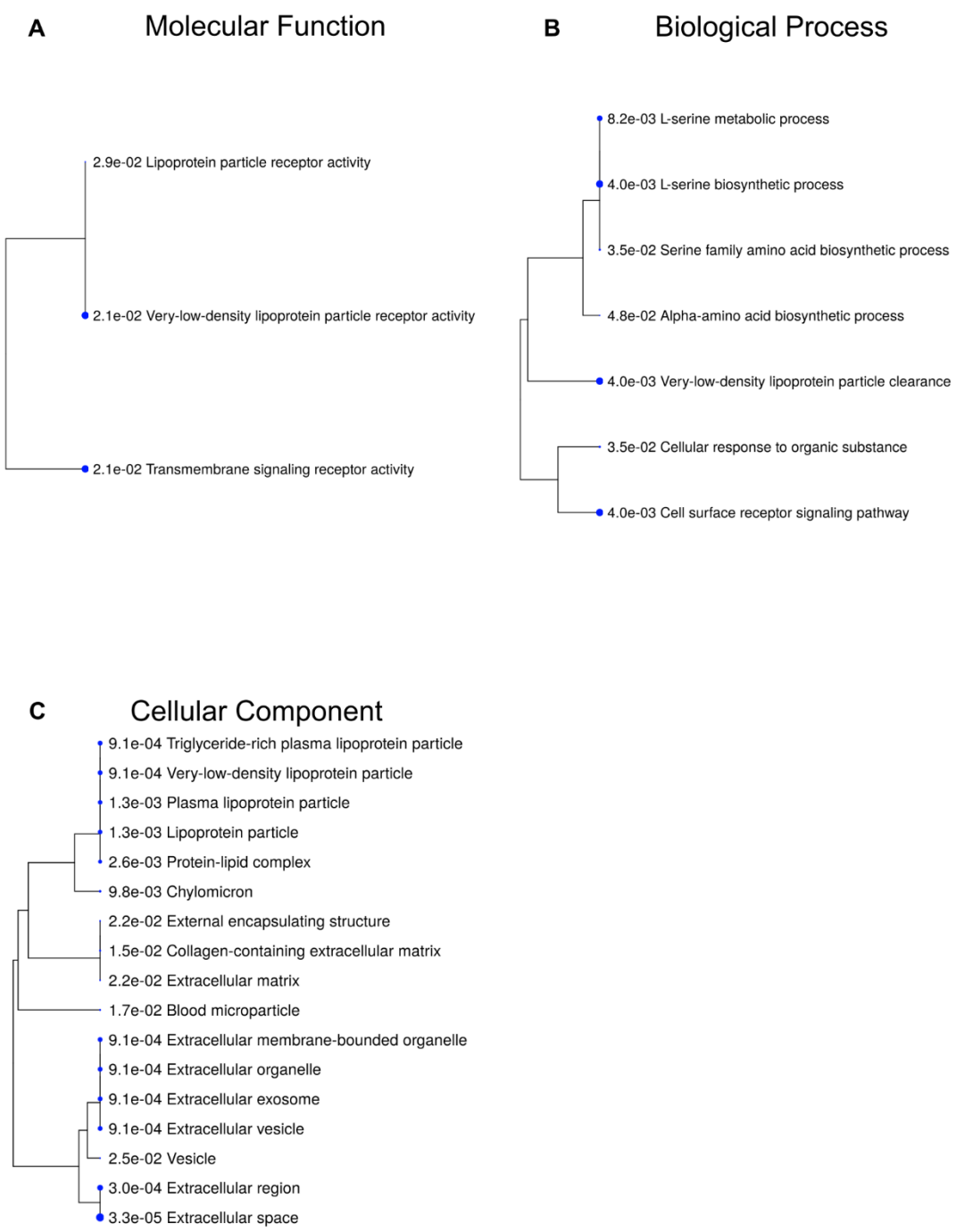

Figure 3.39. GO analysis for α-mangostin up-regulated proteins. Enrichment of GO terms and KEGG pathways for the significant differentially expressed proteins were generated as described in **Figure 3.1** and Methods. Enriched terms and *p*-values are reported. Larger blue dots indicate more significant *p*-values. Panel A: Molecular function. Panel B: Biological process. Panel C: Cellular component.

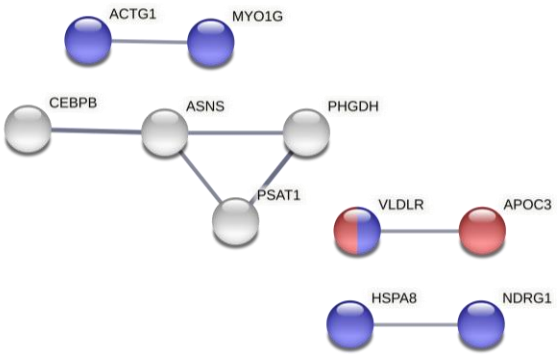

Figure 3.40. Protein-protein interaction network of α-mangostin up-regulated proteins. Protein-protein interaction network of the significant differentially expressed proteins as described in **Figure 3.4** and Methods. Protein nodes are colored based on functional enrichments: Red: KW-0850 VLDL, Blue: GO:0005886 Plasma membrane.

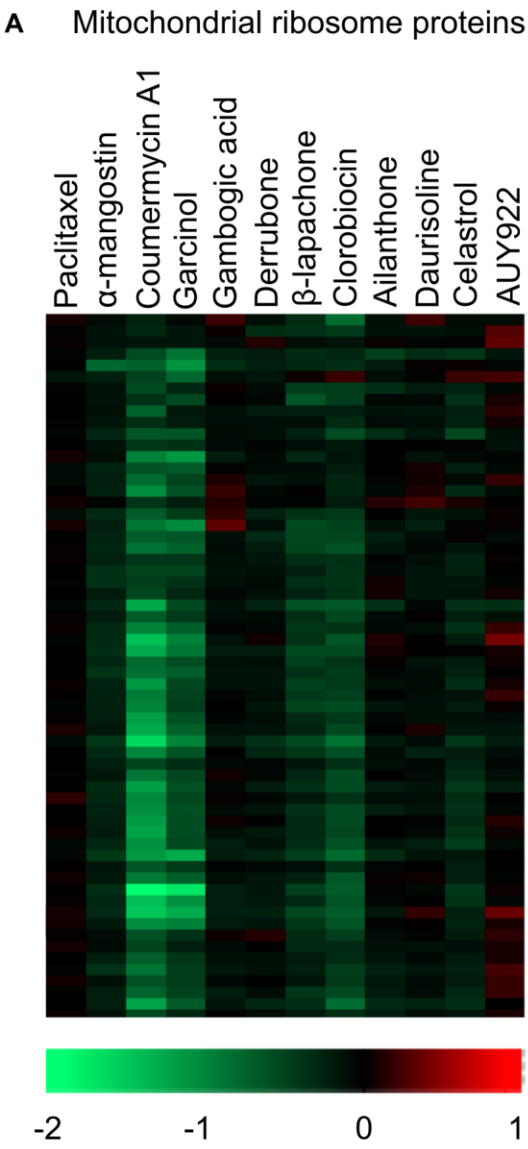

Figure 3.41. Comparison of compound panel changes on protein expression of mitochondrial ribosome proteins. Protein expression was analyzed as described in Chapter 2 Methods, and heat map representing changes in protein expression was constructed for the mitochondrial ribosome proteins. The numbers in the color key located at the bottom heat map are the log2(treated/control) for the average of biological experiments (n=3 for AUY922, n=6 for all other compounds).

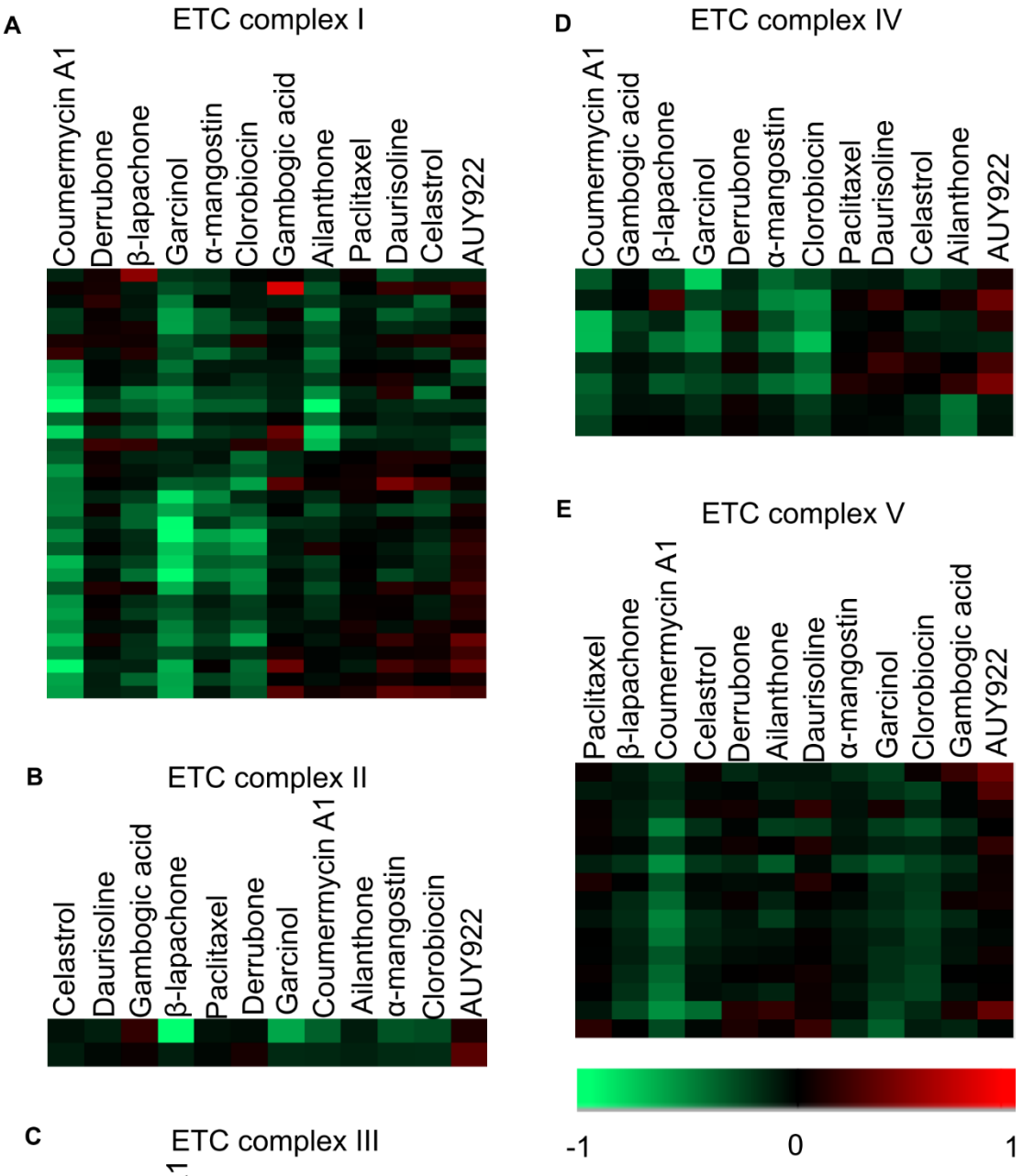

Figure 3.42. Comparison of compound panel changes on protein expression of the electron transport chain (ETC). Protein expression was analyzed as described in Chapter 2 Methods. The color key located at the bottom of Panel E is for the entire figure, the numbers are the log2(treated/control) for the average of biological experiments (n=3 for AUY922, n=6 others). Panel A: complex I. Panel B: complex II. Panel C: complex III. Panel D: complex IV. Panel E: complex V.

Discussion

Bioinformatics analysis of compound perturbations further supports that these compounds are not Hsp90 inhibitors. AUY922 enriched GO terms, and KEGG pathways were highly consistent with literature (**Figure 3.1** and **Figure 3.2**). Comparing AUY922 enrichments to the other compounds in our panel yielded very few conserved terms. Further analysis of conserved enrichments showed minimal conserved proteins driving these conserved terms/pathways between compounds. These results correlate with our findings discussed in Chapter 2 where I concluded that these compounds do no induce cell death through inhibition of Hsp90.

I speculate that disruption of mitochondrial health is a major mechanism of cytotoxicity for ailanthone, celastrol, clorobiocin, coumermycin A1, garcinol, β-lapachone, and α-mangostin. This is driven from the two most common motifs observed in our down-regulated enrichments of our panel: the mitochondrial electron transport chain, and the mitochondrial ribosome (**Figure 3.41** and **Figure 3.42**). This shared motif of mitochondrial perturbation could attribute to the low-moderate Pearson correlations observed in **Table 2.5**. Additionally, the hierarchical clustering in **Figure 2.18** in which we see clorobiocin, coumermycin A1, garcinol, β-lapachone, and α-mangostin significantly cluster. These mitochondrial perturbations are not conserved by our Hsp90 inhibitor, AUY922 (**Figure 3.1, 3.2, 3.41, and 3.42**).

These findings encouraged us to return to the literature for studies that supported our findings. Ailanthone has been reported to induce cell cycle arrest through PI3K-Akt pathway, and apoptosis through the mitochondrial signaling pathway [123]. There are

two reports of celastrol inducing apoptosis through the mitochondrial apoptosis pathway [124-126]. There is one study showing that coumermycin A1 activates PKR leading to cleavage of caspases 8 and 9 [127]. There are two publications indicating garcinol disrupts mitochondrial membrane potential [128, 129]. There are three studies showing that β-lapachone treatment causes loss of mitochondrial membrane potential [130-132]. There is one study on α-mangostin that reports at high concentrations α-mangostin disrupts the electron transport chain, and made the mitochondria membrane permeable thus leading to apoptosis [133]. Based on these previous reports in the literature, I suggest that these compounds be repurposed from Hsp90 inhibitors to antagonist of mitochondria.

I speculate that proteostasis perturbation of the endoplasmic reticulum is a major mechanism of cytotoxicity for garcinol, and a contributing mechanism for celastrol, β-lapachone, gambogic acid, and daurisoline. In addition to the mitochondrial perturbations previously discussed, multiple compounds also enriched GO terms associated with endoplasmic reticulum. The most apparent was garcinol, with enrichment of IRE1-mediated unfolded protein response, ERAD pathway, and multiple terms associated with the removal of endoplasmic reticulum post translational modifications required before they can be transported to the cytosol and degraded (**Figure 3.27**). To a lesser extent, we saw GO terms associated with endoplasmic reticulum for celastrol, β-lapachone, gambogic acid, and daurisoline (**Figures 3.7, 3.13, 3.27, 3.31, and 3.35**).

These results implored us to revisit the literature for studies that reported findings congruent with ours. Garcinol was reported to induce apoptosis, induce endoplasmic reticulum stress, and reduce mitochondrial membrane potential through the accumulation

of reactive oxygen species [128]. Gambogic acid treatment has been reported to induce endoplasmic reticulum stress with XBP1 splicing along and up-regulating BiP mRNA [134]. There are two papers reporting celastrol treatment induces apoptosis through endoplasmic reticulum stress [124, 135]. There are two papers reporting daurisoline and similar compounds induce apoptosis through endoplasmic reticulum stress [136, 137].There are three papers indicating that β-lapachone induces cell death through endoplasmic reticulum stress [130-132]. Based on these previous publications, I suggest that garcinol, β-lapachone, gambogic acid, and daurisoline should be repurposed, and further studied as an antagonist of endoplasmic reticulum proteostasis.

Future Directions

In this work, we repeatedly showed that our compound panel of proposed Hsp90 inhibitors do not induce apoptosis through Hsp90 inhibition, C-terminal or otherwise. Bioinformatics analysis of our proteomic data directed us to motifs indicating that many of the compounds in our panel induced perturbation of mitochondrial, and/or endoplasmic reticulum health. Review of the literature supported our findings. As such, future research on the compounds in our panel should be repurposed to the cellular organelle suggested above.

REFERENCES

1. Chen, B., D. Zhong, and A. Monteiro, *Comparative genomics and evolution of the HSP90 family of genes across all kingdoms of organisms.* BMC Genomics, 2006. **7**: p. 156.
2. Sreedhar, A.S., et al., *Hsp90 isoforms: functions, expression and clinical importance.* FEBS Lett, 2004. **562**(1-3): p. 11-5.
3. Chiosis, G. and L. Neckers, *Tumor selectivity of Hsp90 inhibitors: the explanation remains elusive.* ACS Chem Biol, 2006. **1**(5): p. 279-84.
4. Miyata, Y., H. Nakamoto, and L. Neckers, *The therapeutic target Hsp90 and cancer hallmarks.* Curr Pharm Des, 2013. **19**(3): p. 347-65.
5. Jackson, S.E., *Hsp90: structure and function.* Top Curr Chem, 2013. **328**: p. 155-240.
6. Minami, Y., et al., *The carboxy-terminal region of mammalian HSP90 is required for its dimerization and function in vivo.* Mol Cell Biol, 1994. **14**(2): p. 1459-64.
7. Nemoto, T., et al., *Mechanism of dimer formation of the 90-kDa heat-shock protein.* Eur J Biochem, 1995. **233**(1): p. 1-8.
8. Harris, S.F., A.K. Shiau, and D.A. Agard, *The crystal structure of the carboxy-terminal dimerization domain of htpG, the Escherichia coli Hsp90, reveals a potential substrate binding site.* Structure, 2004. **12**(6): p. 1087-97.
9. Prodromou, C., et al., *Identification and structural characterization of the ATP/ADP-binding site in the Hsp90 molecular chaperone.* Cell, 1997. **90**(1): p. 65-75.
10. Roe, S.M., et al., *Structural basis for inhibition of the Hsp90 molecular chaperone by the antitumor antibiotics radicicol and geldanamycin.* J Med Chem, 1999. **42**(2): p. 260-6.
11. Verba, K.A., et al., *Atomic structure of Hsp90-Cdc37-Cdk4 reveals that Hsp90 traps and stabilizes an unfolded kinase.* Science, 2016. **352**(6293): p. 1542-7.
12. Biebl, M.M. and J. Buchner, *Structure, Function, and Regulation of the Hsp90 Machinery.* Cold Spring Harb Perspect Biol, 2019. **11**(9).
13. Tripathi, V., et al., *Aha1 can act as an autonomous chaperone to prevent aggregation of stressed proteins.* J Biol Chem, 2014. **289**(52): p. 36220-8.
14. Murata, S., et al., *CHIP is a chaperone-dependent E3 ligase that ubiquitylates unfolded protein.* EMBO Rep, 2001. **2**(12): p. 1133-8.
15. Baker, J.D., et al., *Hsp90 Heterocomplexes Regulate Steroid Hormone Receptors: From Stress Response to Psychiatric Disease.* Int J Mol Sci, 2018. **20**(1).

16. Li, J., X. Qian, and B. Sha, *Heat shock protein 40: structural studies and their functional implications.* Protein Pept Lett, 2009. **16**(6): p. 606-12.
17. Zhang, R., et al., *J-domain protein chaperone circuits in proteostasis and disease.* Trends Cell Biol, 2022.
18. Li, Z., F.U. Hartl, and A. Bracher, *Structure and function of Hip, an attenuator of the Hsp70 chaperone cycle.* Nat Struct Mol Biol, 2013. **20**(8): p. 929-35.
19. Bhattacharya, K., et al., *The Hsp70-Hsp90 co-chaperone Hop/Stip1 shifts the proteostatic balance from folding towards degradation.* Nat Commun, 2020. **11**(1): p. 5975.
20. Biebl, M.M., et al., *Structural elements in the flexible tail of the co-chaperone p23 coordinate client binding and progression of the Hsp90 chaperone cycle.* Nat Commun, 2021. **12**(1): p. 828.
21. Freeman, B.C. and K.R. Yamamoto, *Disassembly of transcriptional regulatory complexes by molecular chaperones.* Science, 2002. **296**(5576): p. 2232-5.
22. Knoblauch, R. and M.J. Garabedian, *Role for Hsp90-associated cochaperone p23 in estrogen receptor signal transduction.* Mol Cell Biol, 1999. **19**(5): p. 3748-59.
23. Oxelmark, E., et al., *Genetic dissection of p23, an Hsp90 cochaperone, reveals a distinct surface involved in estrogen receptor signaling.* J Biol Chem, 2003. **278**(38): p. 36547-55.
24. Kreimendahl, S. and J. Rassow, *The Mitochondrial Outer Membrane Protein Tom70-Mediator in Protein Traffic, Membrane Contact Sites and Innate Immunity.* Int J Mol Sci, 2020. **21**(19).
25. Li, W., D. Sahu, and F. Tsen, *Secreted heat shock protein-90 (Hsp90) in wound healing and cancer.* Biochim Biophys Acta, 2012. **1823**(3): p. 730-41.
26. Li, W., et al., *Extracellular Hsp90 (eHsp90) as the actual target in clinical trials: intentionally or unintentionally.* Int Rev Cell Mol Biol, 2013. **303**: p. 203-35.
27. Jayaraj, G.G., M.S. Hipp, and F.U. Hartl, *Functional Modules of the Proteostasis Network.* Cold Spring Harb Perspect Biol, 2020. **12**(1).
28. Brehme, M., et al., *A chaperome subnetwork safeguards proteostasis in aging and neurodegenerative disease.* Cell Rep, 2014. **9**(3): p. 1135-50.
29. Hahn, J.S., et al., *Genome-wide analysis of the biology of stress responses through heat shock transcription factor.* Mol Cell Biol, 2004. **24**(12): p. 5249-56.
30. Trinklein, N.D., et al., *The role of heat shock transcription factor 1 in the genome-wide regulation of the mammalian heat shock response.* Mol Biol Cell, 2004. **15**(3): p. 1254-61.
31. Voellmy, R. and F. Boellmann, *Chaperone regulation of the heat shock protein response.* Adv Exp Med Biol, 2007. **594**: p. 89-99.
32. Krakowiak, J., et al., *Hsf1 and Hsp70 constitute a two-component feedback loop that regulates the yeast heat shock response.* Elife, 2018. **7**.
33. Richter, K., M. Haslbeck, and J. Buchner, *The heat shock response: life on the verge of death.* Mol Cell, 2010. **40**(2): p. 253-66.
34. Hentze, N., et al., *Molecular mechanism of thermosensory function of human heat shock transcription factor Hsf1.* Elife, 2016. **5**.
35. Wodrich, A.P.K., et al., *The Unfolded Protein Responses in Health, Aging, and Neurodegeneration: Recent Advances and Future Considerations.* Front Mol Neurosci, 2022. **15**: p. 831116.

36. Bertolotti, A., et al., *Dynamic interaction of BiP and ER stress transducers in the unfolded-protein response.* Nat Cell Biol, 2000. **2**(6): p. 326-32.
37. Shen, J., et al., *Stable binding of ATF6 to BiP in the endoplasmic reticulum stress response.* Mol Cell Biol, 2005. **25**(3): p. 921-32.
38. Calfon, M., et al., *IRE1 couples endoplasmic reticulum load to secretory capacity by processing the XBP-1 mRNA.* Nature, 2002. **415**(6867): p. 92-6.
39. Acosta-Alvear, D., et al., *XBP1 controls diverse cell type- and condition-specific transcriptional regulatory networks.* Mol Cell, 2007. **27**(1): p. 53-66.
40. Hwang, J. and L. Qi, *Quality Control in the Endoplasmic Reticulum: Crosstalk between ERAD and UPR pathways.* Trends Biochem Sci, 2018. **43**(8): p. 593-605.
41. Yoshida, H., et al., *XBP1 mRNA is induced by ATF6 and spliced by IRE1 in response to ER stress to produce a highly active transcription factor.* Cell, 2001. **107**(7): p. 881-91.
42. Harding, H.P., Y. Zhang, and D. Ron, *Protein translation and folding are coupled by an endoplasmic-reticulum-resident kinase.* Nature, 1999. **397**(6716): p. 271-4.
43. Shoulders, M.D., et al., *Stress-independent activation of XBP1s and/or ATF6 reveals three functionally diverse ER proteostasis environments.* Cell Rep, 2013. **3**(4): p. 1279-92.
44. Bommiasamy, H., et al., *ATF6alpha induces XBP1-independent expansion of the endoplasmic reticulum.* J Cell Sci, 2009. **122**(Pt 10): p. 1626-36.
45. Ciechanover, A. and A.L. Schwartz, *The ubiquitin-proteasome pathway: the complexity and myriad functions of proteins death.* Proc Natl Acad Sci U S A, 1998. **95**(6): p. 2727-30.
46. Bernassola, F., A. Ciechanover, and G. Melino, *The ubiquitin proteasome system and its involvement in cell death pathways.* Cell Death Differ, 2010. **17**(1): p. 1-3.
47. Voges, D., P. Zwickl, and W. Baumeister, *The 26S proteasome: a molecular machine designed for controlled proteolysis.* Annu Rev Biochem, 1999. **68**: p. 1015-68.
48. Whitesell, L., et al., *Inhibition of heat shock protein HSP90-pp60v-src heteroprotein complex formation by benzoquinone ansamycins: essential role for stress proteins in oncogenic transformation.* Proc Natl Acad Sci U S A, 1994. **91**(18): p. 8324-8.
49. Whitesell, L., et al., *Benzoquinonoid ansamycins possess selective tumoricidal activity unrelated to src kinase inhibition.* Cancer Res, 1992. **52**(7): p. 1721-8.
50. Sharma, S.V., T. Agatsuma, and H. Nakano, *Targeting of the protein chaperone, HSP90, by the transformation suppressing agent, radicicol.* Oncogene, 1998. **16**(20): p. 2639-45.
51. Schulte, T.W., et al., *Antibiotic radicicol binds to the N-terminal domain of Hsp90 and shares important biologic activities with geldanamycin.* Cell Stress Chaperones, 1998. **3**(2): p. 100-8.
52. Stebbins, C.E., et al., *Crystal structure of an Hsp90-geldanamycin complex: targeting of a protein chaperone by an antitumor agent.* Cell, 1997. **89**(2): p. 239-50.
53. Supko, J.G., et al., *Preclinical pharmacologic evaluation of geldanamycin as an antitumor agent.* Cancer Chemother Pharmacol, 1995. **36**(4): p. 305-15.

54. Tian, Z.Q., et al., *Synthesis and biological activities of novel 17-aminogeldanamycin derivatives.* Bioorg Med Chem, 2004. **12**(20): p. 5317-29.
55. Le Brazidec, J.Y., et al., *Synthesis and biological evaluation of a new class of geldanamycin derivatives as potent inhibitors of Hsp90.* J Med Chem, 2004. **47**(15): p. 3865-73.
56. Lin, T.Y., et al., *The novel HSP90 inhibitor STA-9090 exhibits activity against Kit-dependent and -independent malignant mast cell tumors.* Exp Hematol, 2008. **36**(10): p. 1266-77.
57. Eccles, S.A., et al., *NVP-AUY922: a novel heat shock protein 90 inhibitor active against xenograft tumor growth, angiogenesis, and metastasis.* Cancer Res, 2008. **68**(8): p. 2850-60.
58. Menezes, D.L., et al., *The novel oral Hsp90 inhibitor NVP-HSP990 exhibits potent and broad-spectrum antitumor activities in vitro and in vivo.* Mol Cancer Ther, 2012. **11**(3): p. 730-9.
59. Immormino, R.M., et al., *Structural and quantum chemical studies of 8-aryl-sulfanyl adenine class Hsp90 inhibitors.* J Med Chem, 2006. **49**(16): p. 4953-60.
60. Lyman, S.K., et al., *High-content, high-throughput analysis of cell cycle perturbations induced by the HSP90 inhibitor XL888.* PLoS One, 2011. **6**(3): p. e17692.
61. Marcu, M.G., T.W. Schulte, and L. Neckers, *Novobiocin and related coumarins and depletion of heat shock protein 90-dependent signaling proteins.* J Natl Cancer Inst, 2000. **92**(3): p. 242-8.
62. Matts, R.L., et al., *Elucidation of the Hsp90 C-terminal inhibitor binding site.* ACS Chem Biol, 2011. **6**(8): p. 800-7.
63. Sgobba, M., et al., *Structural models and binding site prediction of the C-terminal domain of human Hsp90: a new target for anticancer drugs.* Chem Biol Drug Des, 2008. **71**(5): p. 420-433.
64. Morra, G., et al., *Dynamics-Based Discovery of Allosteric Inhibitors: Selection of New Ligands for the C-terminal Domain of Hsp90.* J Chem Theory Comput, 2010. **6**(9): p. 2978-89.
65. Khalid, S. and S. Paul, *Identifying a C-terminal ATP binding sites-based novel Hsp90-Inhibitor in silico: a plausible therapeutic approach in Alzheimer's disease.* Med Hypotheses, 2014. **83**(1): p. 39-46.
66. Bickel, D. and H. Gohlke, *C-terminal modulators of heat shock protein of 90kDa (HSP90): State of development and modes of action.* Bioorg Med Chem, 2019. **27**(21): p. 115080.
67. Li, T., et al., *Targeting the Hsp90-Cdc37-client protein interaction to disrupt Hsp90 chaperone machinery.* J Hematol Oncol, 2018. **11**(1): p. 59.
68. Wang, L., Q. Zhang, and Q. You, *Targeting the HSP90-CDC37-kinase chaperone cycle: A promising therapeutic strategy for cancer.* Med Res Rev, 2022. **42**(1): p. 156-182.
69. Zhang, X., et al., *The Therapeutic Potential of Targeting Hsp90-Cdc37 Interactions in Several Diseases.* Curr Drug Targets, 2022. **23**(10): p. 1023-1038.
70. He, Y., et al., *Ailanthone targets p23 to overcome MDV3100 resistance in castration-resistant prostate cancer.* Nat Commun, 2016. **7**: p. 13122.

71. Chadli, A., et al., *Celastrol inhibits Hsp90 chaperoning of steroid receptors by inducing fibrillization of the Co-chaperone p23.* J Biol Chem, 2010. **285**(6): p. 4224-4231.
72. Patwardhan, C.A., et al., *Gedunin inactivates the co-chaperone p23 protein causing cancer cell death by apoptosis.* J Biol Chem, 2013. **288**(10): p. 7313-25.
73. Hadden, M.K., et al., *Derrubone, an inhibitor of the Hsp90 protein folding machinery.* J Nat Prod, 2007. **70**(12): p. 2014-8.
74. Davenport, J., et al., *Gambogic acid, a natural product inhibitor of Hsp90.* J Nat Prod, 2011. **74**(5): p. 1085-92.
75. Davenport, J., et al., *High-throughput screen of natural product libraries for hsp90 inhibitors.* Biology (Basel), 2014. **3**(1): p. 101-38.
76. Wu, Y., et al., *beta-Lapachone Induces NAD(P)H:Quinone Oxidoreductase-1- and Oxidative Stress-Dependent Heat Shock Protein 90 Cleavage and Inhibits Tumor Growth and Angiogenesis.* J Pharmacol Exp Ther, 2016. **357**(3): p. 466-75.
77. Johnson, J.J., et al., *alpha-Mangostin, a xanthone from mangosteen fruit, promotes cell cycle arrest in prostate cancer and decreases xenograft tumor growth.* Carcinogenesis, 2012. **33**(2): p. 413-9.
78. Watanapokasin, R., et al., *Effects of alpha-mangostin on apoptosis induction of human colon cancer.* World J Gastroenterol, 2011. **17**(16): p. 2086-95.
79. Ding, H., et al., *Ailanthone: A novel potential drug for treating human cancer.* Oncol Lett, 2020. **20**(2): p. 1489-1503.
80. Westerheide, S.D., et al., *Celastrols as inducers of the heat shock response and cytoprotection.* J Biol Chem, 2004. **279**(53): p. 56053-60.
81. Peng, B., et al., *HSP90 inhibitor, celastrol, arrests human monocytic leukemia cell U937 at G0/G1 in thiol-containing agents reversible way.* Mol Cancer, 2010. **9**: p. 79.
82. Zhang, T., et al., *A novel Hsp90 inhibitor to disrupt Hsp90/Cdc37 complex against pancreatic cancer cells.* Mol Cancer Ther, 2008. **7**(1): p. 162-70.
83. Huang, X.H., et al., *Direct targeting of HSP90 with daurisoline destabilizes beta-catenin to suppress lung cancer tumorigenesis.* Cancer Lett, 2020. **489**: p. 66-78.
84. Bantscheff, M., et al., *Quantitative mass spectrometry in proteomics: critical review update from 2007 to the present.* Anal Bioanal Chem, 2012. **404**(4): p. 939-65.
85. Chen, X., et al., *Quantitative Proteomics Using Isobaric Labeling: A Practical Guide.* Genomics Proteomics Bioinformatics, 2021. **19**(5): p. 689-706.
86. Thompson, A., et al., *Tandem mass tags: a novel quantification strategy for comparative analysis of complex protein mixtures by MS/MS.* Anal Chem, 2003. **75**(8): p. 1895-904.
87. Zecha, J., et al., *TMT Labeling for the Masses: A Robust and Cost-efficient, In-solution Labeling Approach.* Mol Cell Proteomics, 2019. **18**(7): p. 1468-1478.
88. Ow, S.Y., et al., *iTRAQ underestimation in simple and complex mixtures: "the good, the bad and the ugly".* J Proteome Res, 2009. **8**(11): p. 5347-55.
89. Karp, N.A., et al., *Addressing accuracy and precision issues in iTRAQ quantitation.* Mol Cell Proteomics, 2010. **9**(9): p. 1885-97.
90. Christoforou, A.L. and K.S. Lilley, *Isobaric tagging approaches in quantitative proteomics: the ups and downs.* Anal Bioanal Chem, 2012. **404**(4): p. 1029-37.

91. McAlister, G.C., et al., *MultiNotch MS3 enables accurate, sensitive, and multiplexed detection of differential expression across cancer cell line proteomes.* Anal Chem, 2014. **86**(14): p. 7150-8.
92. Yorgin, P.D., et al., *Effects of geldanamycin, a heat-shock protein 90-binding agent, on T cell function and T cell nonreceptor protein tyrosine kinases.* J Immunol, 2000. **164**(6): p. 2915-23.
93. Wisniewski, J.R. and F.Z. Gaugaz, *Fast and sensitive total protein and Peptide assays for proteomic analysis.* Anal Chem, 2015. **87**(8): p. 4110-6.
94. Tyanova, S., T. Temu, and J. Cox, *The MaxQuant computational platform for mass spectrometry-based shotgun proteomics.* Nat Protoc, 2016. **11**(12): p. 2301-2319.
95. Tyanova, S., et al., *The Perseus computational platform for comprehensive analysis of (prote)omics data.* Nat Methods, 2016. **13**(9): p. 731-40.
96. Stark, C., et al., *BioGRID: a general repository for interaction datasets.* Nucleic Acids Res, 2006. **34**(Database issue): p. D535-9.
97. Xenarios, I., et al., *DIP: the database of interacting proteins.* Nucleic Acids Res, 2000. **28**(1): p. 289-91.
98. Peri, S., et al., *Human protein reference database as a discovery resource for proteomics.* Nucleic Acids Res, 2004. **32**(Database issue): p. D497-501.
99. Hermjakob, H., et al., *IntAct: an open source molecular interaction database.* Nucleic Acids Res, 2004. **32**(Database issue): p. D452-5.
100. Cusick, M.E., et al., *Literature-curated protein interaction datasets.* Nat Methods, 2009. **6**(1): p. 39-46.
101. Chatr-aryamontri, A., et al., *MINT: the Molecular INTeraction database.* Nucleic Acids Res, 2007. **35**(Database issue): p. D572-4.
102. Manning, G., et al., *The protein kinase complement of the human genome.* Science, 2002. **298**(5600): p. 1912-34.
103. Page, T.J., et al., *Genome-wide analysis of human HSF1 signaling reveals a transcriptional program linked to cellular adaptation and survival.* Mol Biosyst, 2006. **2**(12): p. 627-39.
104. Suzuki, R. and H. Shimodaira, *Pvclust: an R package for assessing the uncertainty in hierarchical clustering.* Bioinformatics, 2006. **22**(12): p. 1540-2.
105. Voruganti, S., et al., *The anticancer drug AUY922 generates a proteomics fingerprint that is highly conserved among structurally diverse Hsp90 inhibitors.* J Proteome Res, 2013. **12**(8): p. 3697-706.
106. Fierro-Monti, I., et al., *A novel pulse-chase SILAC strategy measures changes in protein decay and synthesis rates induced by perturbation of proteostasis with an Hsp90 inhibitor.* PLoS One, 2013. **8**(11): p. e80423.
107. Saei, A.A., et al., *ProTargetMiner as a proteome signature library of anticancer molecules for functional discovery.* Nat Commun, 2019. **10**(1): p. 5715.
108. Boridy, S., et al., *Celastrol targets proteostasis and acts synergistically with a heat-shock protein 90 inhibitor to kill human glioblastoma cells.* Cell Death Dis, 2014. **5**: p. e1216.
109. Wang, J., et al., *Michael acceptor in gambogic acid--Its role and application for potent antitumor agents.* Bioorg Med Chem Lett, 2015. **25**(14): p. 2844-8.

110. Kline, J.T., *Proteomics profiling of putative natural product inhibitors of Hsp90*, in *Biochemistry and Molecular Biology*. 2019, Oklahoma State University - Stillwater.
111. Sink, R., et al., *False positives in the early stages of drug discovery.* Curr Med Chem, 2010. **17**(34): p. 4231-55.
112. Trott, A., et al., *Activation of heat shock and antioxidant responses by the natural product celastrol: transcriptional signatures of a thiol-targeted molecule.* Mol Biol Cell, 2008. **19**(3): p. 1104-12.
113. Klaic, L., R.I. Morimoto, and R.B. Silverman, *Celastrol analogues as inducers of the heat shock response. Design and synthesis of affinity probes for the identification of protein targets.* ACS Chem Biol, 2012. **7**(5): p. 928-37.
114. Ge, S.X., D. Jung, and R. Yao, *ShinyGO: a graphical gene-set enrichment tool for animals and plants.* Bioinformatics, 2020. **36**(8): p. 2628-2629.
115. Szklarczyk, D., et al., *STRING v11: protein-protein association networks with increased coverage, supporting functional discovery in genome-wide experimental datasets.* Nucleic Acids Res, 2019. **47**(D1): p. D607-D613.
116. Yates, B., et al., *Genenames.org: the HGNC and VGNC resources in 2017.* Nucleic Acids Res, 2017. **45**(D1): p. D619-D625.
117. Sharma, K., et al., *Quantitative proteomics reveals that Hsp90 inhibition preferentially targets kinases and the DNA damage response.* Mol Cell Proteomics, 2012. **11**(3): p. M111 014654.
118. Wu, Z., A.M. Gholami, and B. Kuster, *Systematic identification of the HSP90 candidate regulated proteome.* Mol Cell Proteomics, 2012. **11**(6): p. M111 016675.
119. Gopinath, R.K., et al., *The Hsp90-dependent proteome is conserved and enriched for hub proteins with high levels of protein-protein connectivity.* Genome Biol Evol, 2014. **6**(10): p. 2851-65.
120. Pichler, W.J., et al., *Drug Hypersensitivity: How Drugs Stimulate T Cells via Pharmacological Interaction with Immune Receptors.* Int Arch Allergy Immunol, 2015. **168**(1): p. 13-24.
121. Zhou, X., et al., *Serine alleviates oxidative stress via supporting glutathione synthesis and methionine cycle in mice.* Mol Nutr Food Res, 2017. **61**(11).
122. Braakman, I. and N.J. Bulleid, *Protein folding and modification in the mammalian endoplasmic reticulum.* Annu Rev Biochem, 2011. **80**: p. 71-99.
123. Liu, W., et al., *Ailanthone Induces Cell Cycle Arrest and Apoptosis in Melanoma B16 and A375 Cells.* Biomolecules, 2019. **9**(7).
124. Feng, L., et al., *ER stress-mediated apoptosis induced by celastrol in cancer cells and important role of glycogen synthase kinase-3beta in the signal network.* Cell Death Dis, 2013. **4**: p. e715.
125. Chen, G., et al., *Celastrol targets mitochondrial respiratory chain complex I to induce reactive oxygen species-dependent cytotoxicity in tumor cells.* BMC Cancer, 2011. **11**: p. 170.
126. Shrivastava, S., et al., *Anticancer effect of celastrol on human triple negative breast cancer: possible involvement of oxidative stress, mitochondrial dysfunction, apoptosis and PI3K/Akt pathways.* Exp Mol Pathol, 2015. **98**(3): p. 313-27.

127. Zuo, W., et al., *PKR and TLR3 trigger distinct signals that coordinate the induction of antiviral apoptosis.* Cell Death Dis, 2022. **13**(8): p. 707.
128. Cheng, A.C., et al., *Garcinol inhibits cell growth in hepatocellular carcinoma Hep3B cells through induction of ROS-dependent apoptosis.* Food Funct, 2010. **1**(3): p. 301-7.
129. Padhye, S., et al., *Emerging role of Garcinol, the antioxidant chalcone from Garcinia indica Choisy and its synthetic analogs.* J Hematol Oncol, 2009. **2**: p. 38.
130. Lien, Y.C., et al., *Involvement of endoplasmic reticulum stress and activation of MAP kinases in beta-lapachone-induced human prostate cancer cell apoptosis.* Histol Histopathol, 2008. **23**(11): p. 1299-308.
131. Park, M.T., et al., *beta-lapachone significantly increases the effect of ionizing radiation to cause mitochondrial apoptosis via JNK activation in cancer cells.* PLoS One, 2011. **6**(10): p. e25976.
132. Lee, H., et al., *Endoplasmic reticulum stress-induced JNK activation is a critical event leading to mitochondria-mediated cell death caused by beta-lapachone treatment.* PLoS One, 2011. **6**(6): p. e21533.
133. Martinez-Abundis, E., et al., *Effects of alpha-mangostin on mitochondrial energetic metabolism.* Mitochondrion, 2010. **10**(2): p. 151-7.
134. Krajarng, A., et al., *Apoptosis induction associated with the ER stress response through up-regulation of JNK in HeLa cells by gambogic acid.* BMC Complement Altern Med, 2015. **15**: p. 26.
135. Ren, B., et al., *Celastrol induces apoptosis in hepatocellular carcinoma cells via targeting ER-stress/UPR.* Oncotarget, 2017. **8**(54): p. 93039-93050.
136. Yuan, S., et al., *Daurisoline Inhibits ESCC by Inducing G1 Cell Cycle Arrest and Activating ER Stress to Trigger Noxa-Dependent Intrinsic and CHOP-DR5-Dependent Extrinsic Apoptosis via p-eIF2alpha-ATF4 Axis.* Oxid Med Cell Longev, 2022. **2022**: p. 5382263.
137. Liu, E.Y.L., et al., *Tacrine Induces Endoplasmic Reticulum-Stressed Apoptosis via Disrupting the Proper Assembly of Oligomeric Acetylcholinesterase in Cultured Neuronal Cells.* Mol Pharmacol, 2021. **100**(5): p. 456-469.

VITA

Sean Alan Gile

Candidate for the Degree of

Doctor of Philosophy

Dissertation: CHARACTERIZING MECHANISMS OF POTENTIAL INHIBITORS OF THE HSP90 CHAPERONE COMPLEX

Major Field: Biochemistry and Molecular Biology

Biographical:

Education:

Completed the requirements for the Doctor of Philosophy in Biochemistry and Molecular Biology at Oklahoma State University, Stillwater, Oklahoma in May, 2023.

Completed the requirements for the Master of Science in Biochemistry and Molecular Biology at Oklahoma State University, Stillwater, Oklahoma in 2022.

Completed the requirements for the Bachelor of Science in Biochemistry and Molecular Biology at Oklahoma State University, Stillwater, Oklahoma in 2015.